Polarimetric remote sensing system analysis:

Digital Imaging and Remote Sensing Image Generation (DIRSIG) model

validation and impact of polarization phenomenology on material

discriminability

By

Chabitha Devaraj

A dissertation submitted in partial fulfillment of the requirements for the

degree of Doctor of Philosophy in the Chester F. Carlson Center for

Imaging Science, Rochester Institute of Technology

2010

Signature of the Author_____

Accepted by_____
        Coordinator, PhD Degree Program   Date

CHESTER F. CARLSON CENTER FOR IMAGING SCIENCE

ROCHESTER INSTITUTE OF TECHNOLOGY

ROCHESTER, NEW YORK

CERTIFICATE OF APPROVAL

_____

PHD DEGREE DISSERTATION

_____

The PhD Degree Dissertation of Chabitha Devaraj
has been examined and approved by the
dissertation committee as satisfactory for the
dissertation required for the
PhD degree in Imaging Science

_____

Dr. John R. Schott, Dissertation Advisor

_____

Dr. Carl Salvaggio

_____

Dr. David Messinger

_____

Dr. Surendra Gupta

_____

Date

iii

DISSERTATION RELEASE PERMISSION

ROCHESTER INSTITUTE OF TECHNOLOGY

CHESTER F. CARLSON CENTER FOR IMAGING SCIENCE

Title of Dissertation:

Polarimetric remote sensing system analysis:
DIRSIG model validation and impact of polarization phenomenology on material
discriminability

I, Chabitha Devaraj, hereby grant permission to Wallace Memorial Library of
R.I.T. to reproduce my thesis in whole or in part. Any reproduction will not be for
commercial use or profit.

Signature_____

Date

Polarimetric remote sensing system analysis:
DIRSIG model validation and impact of polarization phenomenology on
material discriminability

By
Chabitha Devaraj

Submitted to the
Chester F. Carlson Center for Imaging Science
in partial fulfillment of the requirements
for the degree of Doctor of Philosophy
at the Rochester Institute of Technology

ABSTRACT

In addition to spectral information acquired by traditional multi/hyperspectral systems, passive electro optical and infrared (EO/IR) polarimetric sensors also measure the polarization response of different materials in the scene. Such an imaging modality can be useful in improving surface characterization; however, the characteristics of polarimetric systems have not been completely explored by the remote sensing community. Therefore, the main objective of this research was to advance our knowledge in polarimetric remote sensing by investigating the impact of polarization phenomenology on material discriminability. The first part of this research focuses on system validation, where the major goal was to assess the fidelity of the polarimetric images simulated using the Digital Imaging and Remote Sensing Image Generation (DIRSIG) model. A theoretical framework, based on polarization vision models used for animal vision studies and industrial defect detection applications, was developed within which the major components of the polarimetric image chain were validated. In the second part of this research, a polarization physics based approach for improved material discriminability was proposed. This approach utilizes the angular variation in the polarization response to infer the physical characteristics of the observed surface by imaging the scene in three different view directions. The usefulness of the proposed approach in improving detection performance in the absence of *apriori* knowledge about the target geometry was demonstrated. Sensitivity analysis of the proposed system for different scene related parameters was performed to identify the imaging conditions under which the material discriminability is maximized. Furthermore, the detection performance of the proposed polarimetric system was compared to that of the hyperspectral system to identify scenarios where polarization information can be very useful in improving the target contrast.

Acknowledgements

x

TABLE OF CONTENTS

LIST OF FIGURES

LIST OF TABLES

CHAPTER 1

Introduction

1.1 Research objectives

Traditional optical remote sensing sensors acquire spatial and spectral information. More recently, spectropolarimetric imaging sensors have been developed to acquire spatial, spectral and polarization information. Such an imaging modality offers a complete optical description of a surface that can be utilized in identifying objects with complex morphological and camouflaged structures. A thorough understanding of the polarization phenomenology is required to effectively exploit the polarimetric information in remote sensing applications for improved material discrimination. This in-depth analysis of a polarimetric remote sensing system, however, will require extensive polarimetric data measurements at various imaging configurations. In such cases, synthetic data generation tools that mimic real-world imagery with high fidelity are of great value. This research will highlight the effectiveness of using the Digital Imaging and Remote Sensing Image Generation (DIRSIG) model in understanding the passive electro-optical polarization phenomenology and in performing sensitivity analysis of a polarimetric remote sensing system. Hence the main objectives of this research include

(1)   Validating the capability of DIRSIG in polarimetric image modeling and simulation.

(2)   Investigating the impact of system parameters on material discriminability in polarimetric images.

The vector directional property of radiation from a remotely sensed surface, indicated by polarization, varies with different scene related parameters such as illumination type, observation time, atmospheric condition and object geometry. This variability will influence the separability of materials in the scene and therefore it is important to identify the imaging configurations that maximize the material discriminability in polarimetric images. Moreover, sensor viewing geometry will introduce additional variability in the observed polarization information and therefore polarization physics needs to be incorporated in approaches that aim to maximize material discriminability in polarimetric images. But this comprehensive analysis will require making polarimetric observations at several imaging configurations. So it is advantageous to use synthetic polarimetric imagery simulated using DIRSIG for this polarization phenomenology study. However, prior to using the synthetic data it is essential to confirm the accuracy of polarized radiance prediction by DIRSIG.

1.2 Research approach

In polarimetric remote sensing systems, the sensor reaching polarized radiance can be approximated by the sum of three radiance sources, namely, the unpolarized sunlight reflected by the surface, surface reflected skylight which is the downwelled component, and the upwelled atmospheric component that scatters along the sensor path.

The DIRSIG validation phase of this research aims to verify the correctness of implementation and integration of each link in the polarimetric imaging chain within the simulation model. This was achieved by demonstrating that DIRSIG can precisely replicate the optical polarization phenomena that occur in nature. A theoretical framework for validation of DIRSIG in predicting the polarized signatures within a natural scene was developed. Theoretical polarization vision models (Chapter 3) developed for animal vision studies and industrial defect detection applications were used in this analysis.

A polarization physics-based approach for improved target-background discriminability was proposed and the usefulness of the approach in improving detection performance in the absence of *a priori* knowledge about the target geometry was demonstrated (Chapter 4). The main objective of identifying the influence of system parameters on the observed material discriminability using the proposed approach was accomplished by quantifying the material discriminability and then analyzing the measured discriminability at various imaging configurations. In general, statistical classification techniques that exploit dissimilarity in the polarimetric response of the materials can be used to quantify the material discriminability. However, the quantification results will also depend on the statistical framework of the technique. In order to have a 'generalized' quantification of material discriminability, the well-known contrast metric was used to measure the polarimetric dissimilarity for each target-background pair within a simple scene. Analyzing this direct indicator of discriminability at varying imaging configurations, the optimal imaging conditions to achieve maximum material discriminability were identified.

This analysis was then extended to a more realistic remote sensing scene that contains both spatial variability and multiple target-background materials. In this case, an automatic anomaly detection algorithm was employed to quantify the target discriminability in the scene. These results were integrated with the former contrast analysis observations to interpret the effects of scene induced complexities on material discriminability. Furthermore, the detection performance of the proposed polarimetric system was compared to that of the multispectral system to identify scenarios where polarization information can be very useful in improving the target contrast.

1.3 Research contributions

The major contributions of the proposed research are listed below:

(1)   Validated the accuracy of integration of the polarized version of MODerate resolution atmospheric TRANsmission (MODTRAN) code within the DIRSIG model by performing skylight polarization analysis.

(2)   Validated the correctness of integration of skylight polarization component with the surface reflection polarization inside DIRSIG using water surface reflected skylight analysis.

(3)   Verified the accuracy of DIRSIG in modeling the surface reflection polarization phenomenology by examining the relationship between surface reflection polarization parameters and object geometry for objects with different optical properties.

(4)   Confirmed the accuracy of DIRSIG in calculating the polarized upwelled term and its integration with the surface reflection polarization component using a traditional remote sensing calibration technique.

(5)   Proposed a polarization physics-based approach, which utilizes the polarimetric information observed at multiple sensor view angles, for improved target-background discriminability and demonstrated the usefulness of the approach in improving detection performance in the absence of *a priori* knowledge about the target geometry.

(6)   Performed quantitative analysis of material discriminability in polarimetric images using the proposed approach to identify the effect of various scene related parameters. Analyzed the material discriminability in a realistic scene and identified scenarios where polarization information can improve target discriminability.

1.4 Thesis outline

Polarization phenomenology is introduced in Chapter 2 with emphasis on theory and a mathematical description of the polarization state of light. This chapter continues with the description of the major sources of terrestrial polarization in the visible spectra, which is then followed by a review of polarized radiation measurement methods.

Since this research aims to demonstrate the utility of DIRSIG in polarization phenomenology studies, the correctness of polarization prediction of DIRSIG is verified in Chapter 3. Analysis of skylight polarization and water surface reflected skylight were used in demonstrating the accurate implementation and integration of the described

polarimetric image chain within DIRSIG. Furthermore, the relationship between surface orientation and the predicted polarization signature was verified by analyzing the observed polarization parameters of a hemispherical object. A traditional remote sensing calibration technique was used to verify the effects of upwelled polarization component on the observed surface reflection polarization.

Chapter 4 begins with a detailed description of the polarization phenomenology study to explore the underlying relationship between the polarimetric system parameters and the polarimetric properties of the scene. It also presents a polarization physics-based approach for improved target-background discriminability and demonstrates the usefulness of the approach in improving detection performance in the absence of *a priori* knowledge about the target geometry. This chapter also provides the results of sensitivity analysis of material discriminability in a simple scene for different target background combinations. In addition, the detection performance of the proposed multi-view polarimetric system is compared to that of the multispectral system to identify scenarios where polarization information can be useful in improving the target contrast.

CHAPTER 2

Polarimetric imaging: Theory

2.1 Light and polarization

Light is defined as a transverse electromagnetic wave which vibrates perpendicular to its direction of propagation. As shown in Figure 2.1, a wave propagating in the Z direction and vibrating in the XY plane can be completely characterized using (i) amplitude, (ii) wavelength and (iii) direction of wave oscillation. While the amplitude is indicative of the brightness, the color of light is typically characterized by its wavelength. It is the transverse vibration of the electric field component in the electromagnetic wave that is usually used to describe the polarization state of light and thus polarized light has a preferred plane of vibration (Goldstein 2003). Linearly polarized light is generated when the plane of vibration of the electric field component is in a single fixed plane. Elliptically or circularly polarized light arises when the tip of the electric field describes an ellipse or a circle in any fixed plane intersecting, and normal to, the direction of propagation. Light waves with electric fields vibrating in more than one plane in a random fashion are referred to as unpolarized light. The most important source of light in nature is sunlight which originally is unpolarized but during the process of its

transmission can be converted into totally or partially polarized light. To detect polarization phenomenology that frequently occurs in nature, polarizing filters are required since the human eye is 'polarization blind'.
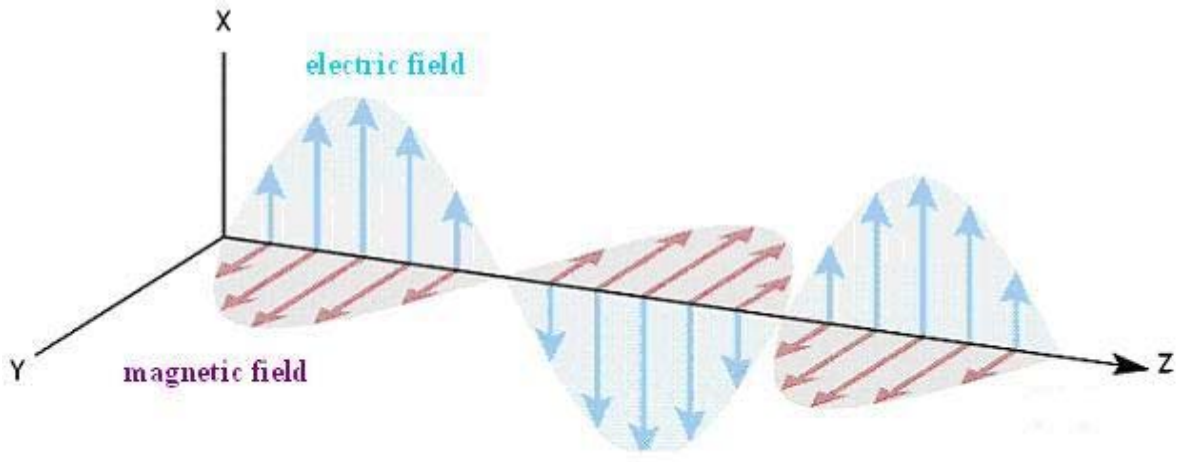
Figure 2.1: Light wave representation.

2.2 Polarization state of light description

The electric field vector of an electromagnetic wave propagating in Z direction given by

$$E = E_0 \cdot e^{i(\omega t - kz + \phi)} \tag{2.1}$$

can be decomposed into two orthogonal components

$$
\begin{aligned}
E_x &= E_{0x} \cdot e^{i(\omega t - kz + \phi_x)} = E_{0x} \cdot \cos\left(\omega t - kz + \phi_x\right) \\
E_y &= E_{0y} \cdot e^{i(\omega t - kz + \phi_y)} = E_{0y} \cdot \cos\left(\omega t - kz + \phi_y\right)
\end{aligned}
\tag{2.2}
$$

Here ϕ_x and ϕ_y are the phase angles of E_x and E_y with peak amplitudes E_{0x} and E_{0y}. k and ω correspond to the wavenumber and angular frequency respectively.

8

A pair of time dependent sinusoidal waves is obtained by normalizing these components

$$\frac{E_x}{E_{0x}} = \cos\left(\omega t - kz + \phi_x\right) = \cos\left(\omega t - kz\right)\cdot\cos\left(\phi_x\right) - \sin\left(\omega t - kz\right)\cdot\sin\left(\phi_x\right) \qquad (2.3)$$

$$\frac{E_y}{E_{0y}} = \cos\left(\omega t - kz + \phi_y\right) = \cos\left(\omega t - kz\right)\cdot\cos\left(\phi_y\right) - \sin\left(\omega t - kz\right)\cdot\sin\left(\phi_y\right). \qquad (2.4)$$

Frequency dependency can be removed by multiplying equation (2.3) by $\sin\left(\phi_y\right)$ and equation (2.4) by $\sin\left(\phi_x\right)$ and subtracting from each other. Likewise equations (2.3) and (2.4) are multiplied by $\cos\left(\phi_y\right)$ and $\cos\left(\phi_x\right)$ and again subtracted to get

$$\frac{E_x}{E_{0x}}\sin\left(\phi_y\right) - \frac{E_y}{E_{0y}}\sin\left(\phi_x\right) = \cos\left(\omega t - kz\right)\cdot\left[\cos\left(\phi_x\right)\cdot\sin\left(\phi_y\right) - \sin\left(\phi_x\right)\cdot\cos\left(\phi_y\right)\right] (2.5)$$

$$\frac{E_x}{E_{0x}}\cos\left(\phi_y\right) - \frac{E_y}{E_{0y}}\cos\left(\phi_x\right) = \sin\left(\omega t - kz\right)\cdot\left[\cos\left(\phi_x\right)\cdot\sin\left(\phi_y\right) - \sin\left(\phi_x\right)\cdot\cos\left(\phi_y\right)\right]. (2.6)$$

Recognizing $\sin(\phi_y - \phi_x) = \cos\left(\phi_x\right)\cdot\sin\left(\phi_y\right) - \sin\left(\phi_x\right)\cdot\cos\left(\phi_y\right)$ and squaring and adding equations (2.5) and (2.6) we get

$$\left(\frac{E_x}{E_{0x}}\right)^2 + \left(\frac{E_y}{E_{0y}}\right)^2 - \left(2\cdot\frac{E_x}{E_{0x}}\cdot\frac{E_y}{E_{0y}}\right)\cdot\cos\left(\delta_\phi\right) = \sin^2\left(\delta_\phi\right), \qquad (2.7)$$

where $\delta_\phi = \phi_y - \phi_x$ is the phase difference between the two orthogonal electric field components. This is the equation of the polarization ellipse traced by the tip of the electric field vector and the mathematical description of the elliptical polarization. Two special cases of the elliptical polarization namely linear and circular polarization are

9

determined by the phase difference between the orthogonal wave components. Linear polarization occurs when $\delta_\phi = 0 \; or \; \pi$ and is given by

$$\left(\frac{E_x}{E_{0x}}\right)^2 + \left(\frac{E_y}{E_{0y}}\right)^2 - \left(2 \cdot \frac{E_x}{E_{0x}} \cdot \frac{E_y}{E_{0y}}\right) = 0 \,, \tag{2.8}$$

which is further reduced to

$$\left(\frac{E_x}{E_{0x}} - \frac{E_y}{E_{0y}}\right)^2 = 0$$
$$\therefore \frac{E_x}{E_{0x}} = \frac{E_y}{E_{0y}} \tag{2.9}$$

Circular polarization arises when the phase difference $\left(\delta_\phi\right)$ between the two orthogonal electric field components is $\pm\dfrac{\pi}{2}$. Then equation (2.7) reduces to a familiar form of equation of a circle which is given by

$$\left(\frac{E_x}{E_{0x}}\right)^2 + \left(\frac{E_y}{E_{0y}}\right)^2 = 1 \,. \tag{2.10}$$

2.3 Polarization parameters

Stokes (1852) showed that with some algebraic manipulation including taking the time averages, equation (2.7) can be written as,

$$\left(E_{0x}^2 + E_{0y}^2\right)^2 = \left(E_{0x}^2 - E_{0y}^2\right)^2 + \left(2E_{0x}E_{0y}\cos\delta_\phi\right)^2 + \left(2E_{0x}E_{0y}\sin\delta_\phi\right)^2 \,. \tag{2.11}$$

Then each term in equation (2.11) is used to define the Stokes vector $\left(S\right)$ as,

$$S = \begin{bmatrix} S_0 \\ S_1 \\ S_2 \\ S_3 \end{bmatrix} = \begin{bmatrix} E_{0x}^2 + E_{0y}^2 \\ E_{0x}^2 - E_{0y}^2 \\ 2E_{0x}E_{0y}\cos\delta_\phi \\ 2E_{0x}E_{0y}\sin\delta_\phi \end{bmatrix}. \qquad (2.12)$$

In equation (2.12), the components of the Stokes vector are defined as follows: S_0 is the total intensity of light, S_1 is the preponderance of horizontally polarized light over vertically polarized light, S_2 is the preponderance of light polarized at +45° over -45° and S_3 is the preponderance of right circularly polarized light over left circularly polarized light. The state of polarization of light can be expressed using the Degree of Polarization (DOP) and Angle of Polarization (AOP), which can be derived from the Stokes parameters (Hecht 1990) using,

$$DOP = \frac{\left(S_1^2 + S_2^2 + S_3^2\right)^{\frac{1}{2}}}{S_0} \quad \text{and} \qquad (2.13)$$

$$AOP = \frac{1}{2}\tan^{-1}\left(\frac{S_2}{S_1}\right). \qquad (2.14)$$

In traditional remote sensing, intensity is the parameter that is usually measured, whereas in polarimetric imaging additional information about the state of polarization is also measured by observing S_1 and S_2. Circular polarization is usually assumed to be negligible in remote sensing (Egan 1985; Tyo et al. 2006) and the Degree of Linear Polarization (DOLP) is defined as

$$DOLP = \frac{\left(S_1^2 + S_2^2\right)^{1/2}}{S_0}. \qquad (2.15)$$

2.4 Generation of polarized light in nature

The most important source of light in nature is the unpolarized sunlight. However, processes such as reflection, refraction and scattering produce polarized light (Können 1985). Unpolarized light that falls on an object will be emitted as polarized light due to the resulting vibration of the electrons in the object that can oscillate in the same direction as the vibrations of the incident light. Thus the transverse nature of light waves converts the unpolarized light to polarized light.

2.4.1 Polarization by scattering

Scattering occurs due to transmission of light in all directions by particles which are smaller than the wavelength of light. Usually the DOP is at the greatest when scattering results in a change of direction of the incident light at about 90° from the original direction of propagation. This angle is called the scattering angle which represents the angular distance between the original light source and the point of observation. For example, molecules in the atmosphere or miniscule dust particles will result in totally linearly polarized light at a scattering angle of 90°. The DOP will be very small when observed around the sun and almost negligible at scattering angles of 0°(forward scattering direction) and 180°(backward scattering direction). There is no circular polarization at any scattering angle. Also the polarized light vibrates perpendicular to an imaginary plane including the source, the scattering center and the point of observation. As a result, the pattern of polarization (Matchko and Gerhart 2005) produced by scattering is always tangential with respect to the original source as shown in Figure 2.2.
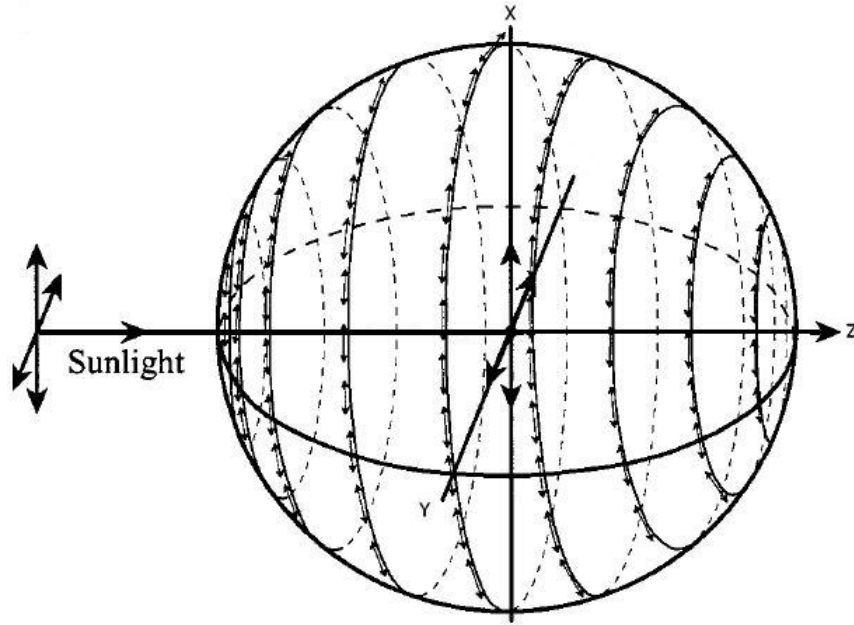
Figure 2.2: Polarization pattern produced by scattering of sunlight.

2.4.2 Polarization by reflection and refraction

When light is incident on large smooth surfaces of metals or dielectrics, the electric field of the incident light wave causes the electrons near the surface to vibrate and reradiate as reflected rays. During this process, a portion of the incoming beam also penetrates the material and this transition from one medium to another that changes the direction of propagation is known as refraction. The index of refraction $(\hat{n})$ of the material indicates the degree to which the refraction process can occur. The incident, reflected and the refracted light rays lie on the same plane called the plane of incidence (POI) as shown in Figure 2.3. The angle that the incident and the reflected light makes with the surface normal is called the angle of incidence and reflection. Conversion of unpolarized light to linearly polarized light is possible during reflection and refraction; however, the resulting polarization pattern will differ from one another. While the

13

refracted wave is polarized in a direction parallel to the POI, the reflected wave is polarized in a direction perpendicular to the POI. Therefore, when unpolarized light illuminates the object, the surface reflection and refraction processes generate horizontally and vertically linearly polarized light as shown in Figure 2.3. Also, the DOP of the reflected and the refracted light depends on the index of refraction of the material and the angle of incidence.
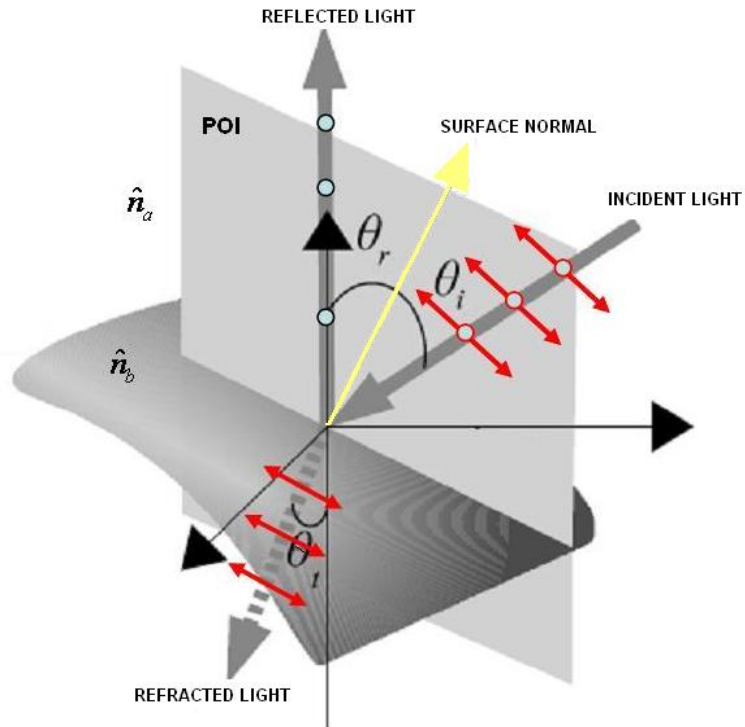
Figure 2.3: Polarization pattern produced by reflection and refraction.

Light reflected from the surface of most types of materials can be separated into two major components: first surface reflection and body or volume reflection. It is necessary to make the distinction between these two kinds of interaction which have totally different effects on the polarization of the reflected light. As shown in Figure 2.4, first surface reflection takes place at the interface between air and matter when the

14

incident light reflects immediately off the surface. Body reflection occurs when the light wave penetrates the object, undergoes multiple scattering due to the inhomogeneities inside the material and then reflects back into the air. Due to the random nature of internal scattering as shown in Figure 2.4, the light becomes depolarized which is the opposite of the first surface scattering that linearly polarizes the incident unpolarized light as shown in Figure 2.3. Also the internal scattering is responsible for color by selective spectral absorption. The interfaces of smooth, transparent objects cause less body reflection or absorption as opposed to opaque objects.

(a) (b)
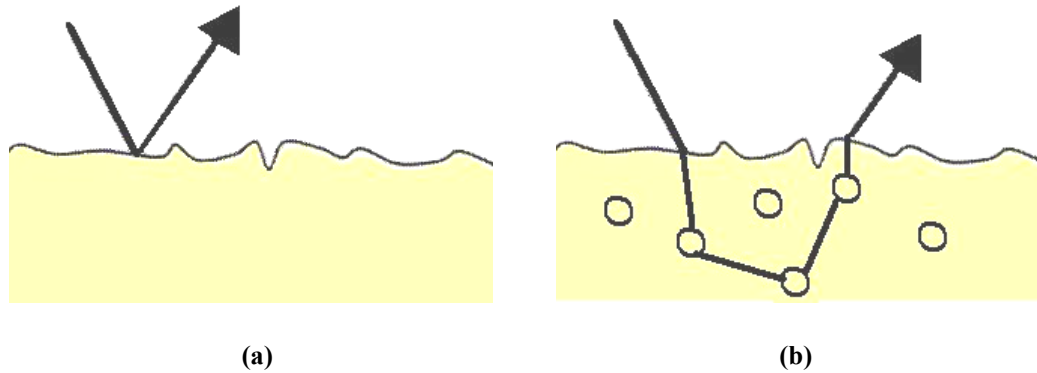
Figure 2.4: Surface scattering phenomenon (a) First surface reflection and (b) Body reflection.

The first surface reflection polarization component of the electric field perpendicular to the POI is called s-polarization and the component parallel to the POI is termed p-polarization. The Fresnel coefficient of reflection (Hecht 1990) is defined as the ratio between the amplitude of the reflected and the incident light. R_s and R_p are the Fresnel coefficients of reflection with respect to the perpendicular and the parallel plane to the POI, respectively

$$R_s = \frac{\left(A - \cos(\alpha)\right)^2 + B^2}{\left(A + \cos(\alpha)\right)^2 + B^2} \text{ and } R_p = R_s \left[\frac{\left(A - \sin(\alpha)\tan(\alpha)\right)^2 + B^2}{\left(A + \sin(\alpha)\tan(\alpha)\right)^2 + B^2}\right] \quad (2.16)$$

where

$$A = \sqrt{\frac{\sqrt{C} + D}{2}}, B = \sqrt{\frac{\sqrt{C} - D}{2}}, C = 4n_r^2 k_r^2 + D^2 \text{ and } D = n_r^2 - k_r^2 - \sin^2(\alpha), \quad (2.17)$$

with the complex refractive index of the material $\hat{n} = n_r + ik_r$ and reflection angle α measured with respect to the surface normal. DOP is then defined using the Fresnel coefficients as

$$DOP(\alpha, n_r, k_r) = \frac{R_s - R_p}{R_s + R_p}, \quad (2.18)$$

where

$$\cos(2\alpha) = \cos(\theta_i)\cos(\theta_r) + \sin(\theta_i)\sin(\theta_r)\cos(\varphi_i - \varphi_r) \quad (2.19)$$

with (θ_i, φ_i) and (θ_r, φ_r) corresponding to source elevation and azimuth angles and observation elevation and azimuth angles. Figure 2.5 illustrates the dependency of polarization on angle of incidence in forward scattering direction for a dielectric and a metallic surface.

The angle at which the maximum reflection polarization occurs is known as the Brewster's angle (θ_b) which is given by

$$\theta_b = \arctan\left(\frac{\hat{n}_b}{\hat{n}_a}\right) \quad (2.20)$$

where $\hat{n}_a$ and $\hat{n}_b$ are the refractive indices of material a and b. In contrast to scattering polarization, the maximum DOP for reflection polarization always happens at an angle

16

lower than 90°. In the case of external reflection $\dfrac{\hat{n}_b}{\hat{n}_a} > 1$, so it immediately follows that

$\theta_b < 90°$. For example, the Brewster's angle for glass $(\hat{n}_b \approx 1.5)$ and a metal

$\left(\hat{n}_b \approx 1.94 \left(1 + 2.7\mathrm{i} \right) \right)$ surface in air $(\hat{n}_a \approx 1)$ is 56.31° and 79.85° respectively. Moreover,

$R_p = 0$ at the Brewster's angle for glass surface. Since the index of refraction for a given

material changes depending on the wavelength of light, Brewster's angle will also vary

with wavelength.
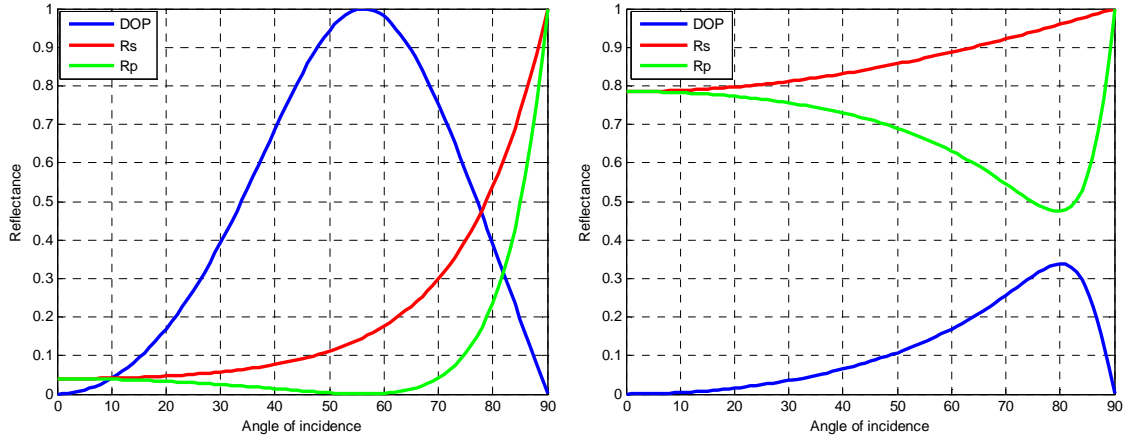
Figure 2.5: DOP of surface reflected light as a function of reflection angle for (a) glass and (b) metal.

Also, from Figure 2.5 it can be identified that polarization information is very

useful in discriminating electrically conducting materials such as metals and dielectrics.

The main difference between bare metals and dielectrics is that the former reflects light

with higher efficiency but has lower polarizing capability. Moreover, at grazing incidence

angles the reflected polarization of metals reaches its maximum. These two polarization

properties were found to be useful in classifying such material types. Wolff (1990)

demonstrated the capability of polarization based methods to segment material surfaces

17

according to varying levels of relative electrical conductivity. Egan (2004) improved the detectability of vehicles and personnel in desert background and foliage utilizing the surface reflection polarization information. Previous research (Egan 2000; Egan and Duggin 2000, 2002; Jones et al. 2006; Jong et al. 2000) has also shown that various manmade objects were discriminated from natural backgrounds using the distinct polarization properties of these materials.

Reflected polarized visible light was used to detect scene surface roughness due to the underlying differences in the scattering mechanisms of smooth and rough surfaces. Laboratory and field studies (Coulson 1966; Raven et al. 2002) have been performed to demonstrate the utility of the polarization property in soil mapping. Polarimetric characteristics of soil was used to distinguish soil types, which differ in their moisture content (Curran 1978, 1979) and particle size (Genda and Okayama 1978). Also the polarization of reflected light provides valuable information for characterizing vegetation types (Curran 1981, 1982; Egan 1970; Egan et al. 1992; Raven et al. 2002; Vanderbilt et al. 1985a; Vanderbilt et al. 1988; Vanderbilt et al. 1985b) with surface structural variations.

2.5 Measurement of the state of polarization

Conventional panchromatic cameras measure the intensity of optical radiation over a single spectral band. Spectral imaging systems measure the intensity over a number of spectral bands, which can range from three as in a color camera through multispectral systems that measure a few spectral bands to hyperspectral systems that measure hundreds of spectral bands. These systems provide information about the

spectral properties of materials in the observed scene. Imaging polarimetry (Clarke and Grainger 1971) seeks to measure information about the vector nature of the optical field across the scene by sampling in polarization angle space.

2.5.1 Polarizer

A polarizer (Goldstein 2003) is a device that converts an unpolarized light beam into a beam with a single polarization state. Polarizers are divided into two general categories namely absorptive polarizers and beam splitting polarizers. Absorptive polarizers are based on the phenomenon of polarization by selective absorption or dichroism (Hecht 1990), which is caused due to absorption anisotropy in materials. The simplest polarizer is the wire grid polarizer, which consists of a regular array of parallel metallic wires, placed in a plane perpendicular to the incident beam. The electric field that is parallel to the wires causes the electrons in the wires to vibrate and acts as a metallic surface that reflects light. But for the electric field that is perpendicular to the wires, the electrons cannot move across the wire and therefore the incident wave travels through the grid. Since the electric field component parallel to the wires is reflected, the transmitted wave is linearly polarized in the direction perpendicular to the wires. The intensity of transmitted light depends on the relative orientation between the polarization direction of the incoming light and the polarization axis of the polarizer. Unlike absorptive polarizers, beam splitting polarizers do not absorb but split the incident beam into two fully polarized beams with orthogonal polarizations. Beam splitting polarizers (Tyo et al. 2006) are used in applications where both the polarization components are analyzed simultaneously.

2.5.2 Imaging polarimetry

The difference in the electrical characteristics of materials causes differences in how the light reflects off these surfaces. According to the Fresnel reflection theory, dielectric surfaces strongly polarize light upon surface reflection and a significantly higher conductivity of the material makes surface reflected light much less partially polarized. The polarization state of a partially linearly polarized light wave is studied by considering it as a sum of two components: a completely linearly polarized and a completely unpolarized light. Therefore, a polarization sensor has to compute the magnitude of the light, the proportion and the angle of the linearly polarized component and this is achieved by rotating a polarizer in front of a camera (Wolff and Boult 1991).

The relationship between the magnitude of the transmission of a partially polarized light wave $\left(I_\varphi\right)$ through a linear polarizer and the angle of polarization axis of the polarizer $\left(\varphi\right)$ is described using a sinusoidal function as

$$I_\varphi = \frac{I_{max} - I_{min}}{2} \cos\left(2\varphi - 2 \cdot \text{AOP}\right) + \frac{I_{max} + I_{min}}{2} \tag{2.21}$$

where I_{min} and I_{max} represent the minimum and the maximum magnitudes observed through the polarizer. The observed variation in the light intensity, which is reflected off the surface of a 50% horizontally polarized target, as a function of polarizer orientation angles is shown in Figure 2. 6. DOLP can also be written in terms of observed light intensities as

$$\text{DOLP} = \frac{\left(S_1^2 + S_2^2\right)^{1/2}}{S_0} = \frac{I_{max} - I_{min}}{I_{max} + I_{min}}. \tag{2.22}$$

20

By substituting DOLP from equation (2.22), equation (2.21) can be rewritten as

$$I_\varphi = \frac{S_0}{2} \Big[\text{DOLP} \cdot \cos\big(2\varphi - 2 \cdot \text{AOP}\big) + 1 \Big] \qquad (2.23)$$

From equation (2.23) it can be immediately recognized that $I_\varphi = I_{max}$ when $\varphi = \text{AOP}$. In other words, the observed intensity reaches its maximum value when the polarizer orientation aligns with the polarization angle of the surface reflected light. It can also be identified from Figure 2. 6 that $\text{DOLP} = \dfrac{I_{max} - I_{min}}{I_{max} + I_{min}} = 0.5$ at $\varphi = 0$ and the estimation of the polarization parameters requires infinite polarizer orientation samples. However, it can be seen from equation (2.23) that a reliable estimate of the polarization characteristics of the surface can be obtained from images observed at three different polarizer orientations.
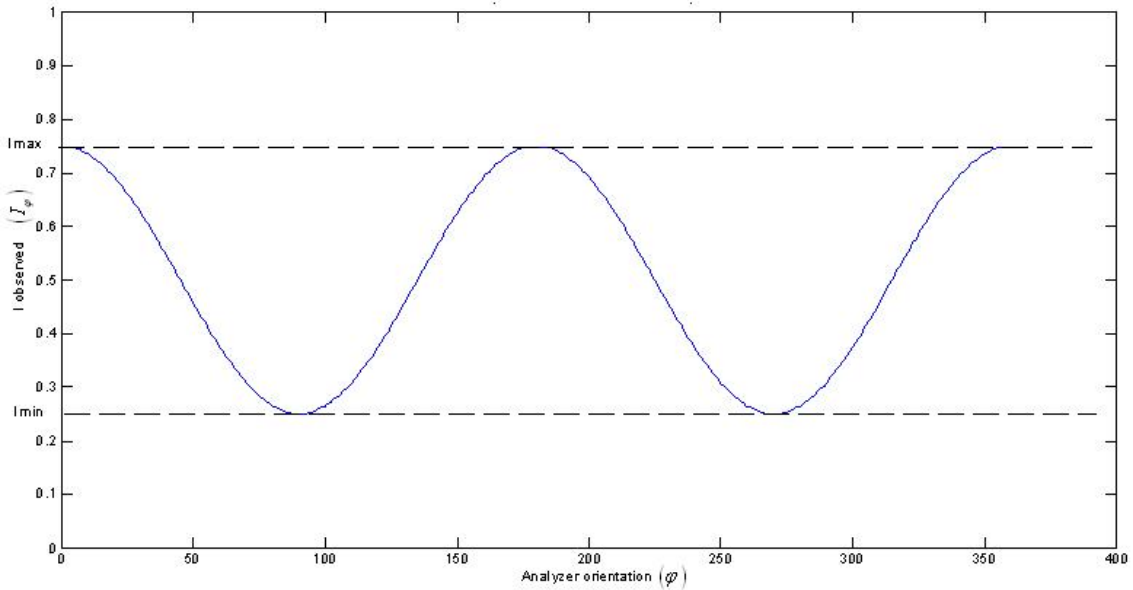
Figure 2. 6: Sinusoidal representation of the observed intensity through a linear polarizer.

21

2.5.3 Polarization measurement methodologies

As stated earlier, it is essential to measure the polarization state of light accurately and this section presents different measurement methods that are widely used in polarimetric imaging.

(a)   Pickering's method

Solomon (1981) reviews the principles of single parameter polarimetric imaging and introduces the concept of multi parameter Stokes vector imaging. Measurements of polarization were made at increments of 45° using linear polarizers. It is indicated that the application of this methodology is effective in remote sensing applications such as feature discrimination and identification. Stokes vector image construction is achieved by using equation (2.24) where I_0, I_{45} and I_{90} are the observation images.

$$
\begin{aligned}
S_0 &= I_0 + I_{90} \\
S_1 &= I_0 - I_{90} \\
S_2 &= 2I_{45} - I_0 - I_{90}
\end{aligned}
\quad . \tag{2.24}
$$

(b)   Modified Pickering's method

Walraven (1981) modified the Pickering method and derived the Stokes images as in equation (2.25) using an additional observation made at 135°.

$$
\begin{aligned}
S_0 &= \tfrac{1}{2}\left(I_0 + I_{45} + I_{90} + I_{135}\right) \\
S_1 &= I_0 - I_{90} \\
S_2 &= I_{45} - I_{135}
\end{aligned}
\quad . \tag{2.25}
$$

(c)   Fessenkov's method

22

Prosch et al. (1983) developed a new polarimetric imaging technique using three linear polarizer orientations at 0°, 60° and 120°. The visual analysis results demonstrate increased target contrast using this method. The Stokes images are calculated using

$$S_0 = \tfrac{2}{3}\left(I_0 + I_{60} + I_{120}\right)$$
$$S_1 = \tfrac{2}{3}\left(2I_0 - I_{60} - I_{120}\right). \tag{2.26}$$
$$S_2 = -\tfrac{2}{\sqrt{3}}\left(I_{120} - I_{60}\right)$$

where I_0, I_{60} and I_{120} are the measured polarimetric images. DOP and AOP can then be estimated using equations (2.13) and (2.14) with the Stokes images calculated using equation (2.24), (2.25) or (2.26).
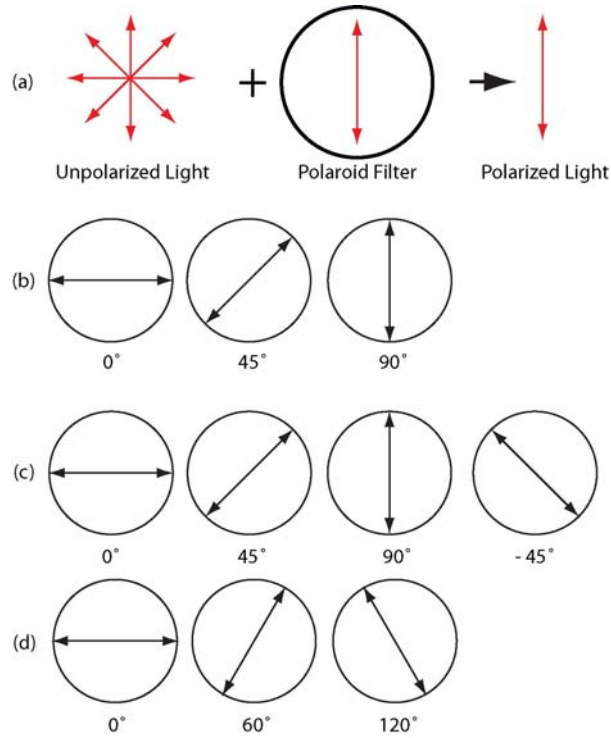
Figure 2.7: Polarization measurement: (a) Filtering concept, (b) Pickering's method, (c) Modified Pickering's method, and (d) Fessenkov's method

Figure 2.7 presents a summary of these measurement techniques with the corresponding filter orientations. It should be noted that the irradiance measured with the linear polarizer oriented to transmit at an angle φ is with reference from the horizontal axis.

2.6 Summary

This chapter presented the theory on the polarization property of light and the mathematical description of different types of polarization namely elliptical, linear and circular polarization. Sunlight is originally unpolarized, however, processes in nature such as scattering, reflection and refraction convert it into totally or partially polarized light. Different scattering mechanisms and their impact on the polarization characteristics of the reflected light was also discussed. This description also provided an introduction to the first surface reflection polarization phenomenology and indicated the importance of understanding the effect of reflection on the state of polarization in order to effectively use the polarimetric information for improved surface characterization and discrimination. Measurement of information about the vector nature of the optical field across the scene using an imaging polarimetry that samples in the polarization angle space was addressed. Different measurement methodologies useful in the study of the polarization state of a partially linearly polarized light were also discussed. Polarization phenomenology will be discussed in more detail in Chapter 3 and will be used in developing a theoretical framework for validating the capability of DIRSIG in polarimetric image modeling and simulation.

CHAPTER 3

Validation of DIRSIG polarimetric image modeling and simulation

3.1 Introduction

The passive electro-optical and infrared (EO/IR) polarized imaging modality is of interest to many because it potentially offers unique phenomenology compared to traditional multispectral and hyperspectral systems. The degree of polarization for man-made objects in the EO/IR region is useful because the natural backgrounds are predominantly unpolarized at these wavelengths. A complete understanding of polarization phenomenology is required to effectively use the polarimetric information for improved surface characterization and discrimination. As the interest in polarization sensitive imaging systems increases, the Digital Imaging and Remote Sensing Image Generation modeling tool (DIRSIG 2004) that can be used to perform instrument trade studies and to generate data for algorithm testing, was adapted to correctly predict the polarization signatures. The incorporation of polarization into the image chain simulated by this tool needed to address the modeling of the natural illuminants (e.g. Sun, Moon, Sky), background sources (e.g. adjacent objects), the polarized Bidirectional Reflectance Distribution Function (pBRDF) of surfaces, atmospheric propagation (extinction,

scattering and self emission) and sensor effects (e.g. optics, filters). Although, each of these links in the image chain may utilize unique modeling approaches, they must be integrated under a framework that addresses important aspects such as a unified-coordinate space and a common polarization state convention. This chapter includes the theory utilized in the modeling tools incorporated into the image chain model to integrate these links into a full signature prediction capability. This chapter also presents a theoretical framework for validation of DIRSIG in predicting the polarized signatures within a natural scene. As a part of this effort, theoretical and empirical models will be used to demonstrate the correctness of implementation and integration of the polarimetric image chain within DIRSIG.

3.2 DIRSIG polarimetric imaging: Validation methodology

The Digital Imaging and Remote Sensing Image Generation (DIRSIG) model is a high fidelity synthetic image generation tool developed at the Rochester Institute of Technology. DIRSIG is a physics-based radiation propagation model, which was designed to simulate broadband, multispectral and hyperspectral imagery. Recently, DIRSIG was extended to support rendering scenes polarimetrically in the visible through thermal infrared regions of the spectrum (Gartley 2007; Meyers 2002; Shell 2005). The simulation tool utilizes community-developed modeling tools such as the experimental version of the MODerate resolution atmospheric TRANsmission (MODTRAN) code (Berk et al. 1989) and BRDF models that have been either derived or extended for polarization. High fidelity synthetic imagery can be used in a number of applications ranging from sensor design studies, to algorithm development and testing, to analyst

training. One of the major benefits of using synthetic imagery is the inherent ground truth data available for every pixel in the scene. Also, synthetic images can be relatively easily generated for a range of variables and provides the user with the capability to control all the variables. This growing dependence of numerous applications on the modeling and simulation capability of DIRSIG increases the importance of ensuring the correctness and reliability of the simulated imagery. This chapter will describe the validation steps performed to assess the fidelity of DIRSIG in replicating the optical polarization phenomena that occur in nature.

Figure 3.1 illustrates the polarimetric image chain within DIRSIG and the key components that require validation. Although, each of these components in the image chain utilize unique modeling approaches, they must be integrated correctly under a framework that addresses important aspects such as a unified coordinate space and a common polarization state convention.
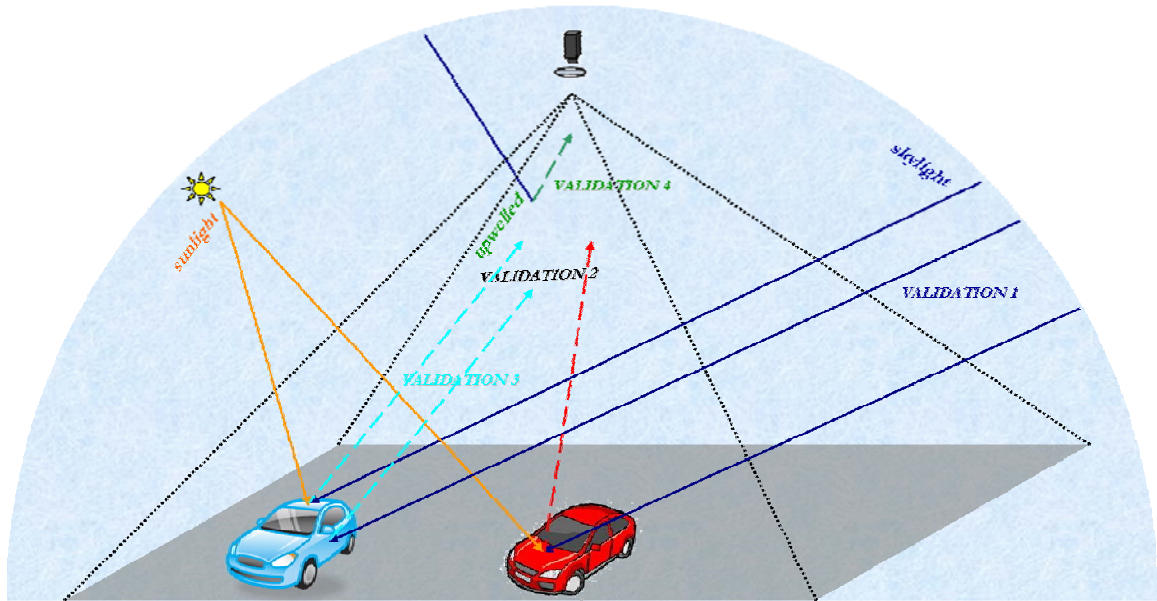
Figure 3.1: Polarimetric image chain and DIRSIG validation of different components.

27

Different validations steps to demonstrate the correctness of implementation and integration of the polarimetric image chain within DIRSIG are listed below.

(1) Validation1: Investigate the accuracy of integration of the polarized version of MODTRAN within DIRSIG.

(2) Validation2: Confirm the correctness of integration of skylight polarization with the surface reflection polarization.

(3) Validation3: Validate the relationship between the surface reflection polarization parameters and object geometry.

(4) Validation4: Examine the effect of upwelled polarization component on the observed surface reflection polarization.

Polarimetric imaging in the natural environment in the reflective spectrum utilizes two illuminant sources: sunlight and skylight. Transmitted sunlight is unpolarized since the exoatmospheric light from the Sun is unpolarized and forward scattering does not impart any significant polarization. However, the diffuse skylight can be highly polarized due to atmospheric scattering of the sunlight. Since the polarization state of the skylight is found to vary over the sky dome, it is important to predict these parameters accurately. DIRSIG has historically utilized the AFRL atmospheric radiative transfer codes [MODTRAN (Berk et al. 1989) and FASCODE (Smith et al. 1978)] for all solar, lunar, sky and path contributions. To model the polarized atmosphere, DIRSIG uses the polarized version of MODTRAN (Fetrow 2003). This chapter presents the theory on skylight polarization that occurs due to Rayleigh atmospheric scattering in Section 3.3.2. The accuracy of skylight polarization prediction of DIRSIG is verified using a simple scene within the DIRSIG simulation as described in Section 3.3.3. Both qualitative and

quantitative analysis was performed to investigate the accuracy of integration of the polarized version of MODTRAN inside the simulation tool.

Synthetic polarimetric images will also include the surface reflection polarization in a natural scene. Therefore, the implementation of the coordinate transformations within DIRSIG that are necessary for accurate simulation of polarized reflection from surface materials was verified. Section 3.4.1 presents the theory of surface reflection polarization with the mathematical description of the reflected polarized radiance. Firstly, the correctness of integration of the polarized skylight with the surface reflection component was confirmed. A theoretical model for the reflection polarization pattern of flat water under clear sky at sunset is presented in Section 3.5. The accuracy of the water surface reflected skylight polarization by DIRSIG is described in Section 3.5.1. Secondly, the accuracy of DIRSIG in modeling the surface reflection polarization phenomenology will be assessed using objects with different optical properties. The relationship between surface reflection polarization parameters and object geometry is discussed in Section 3.6. Lastly, the effects of upwelled polarization component on the observed surface reflected polarization is described in Section 3.7.

3.3 Polarization by scattering

3.3.1 Polarization of light in the atmosphere

Polarization due to skylight occurs mainly as a result of the scattering of sunlight in the Earth's atmosphere. Since both the DOP and the AOP depend on the position of the Sun, the skylight polarization can be described most conveniently by referring to a Sun related coordinate system as shown in Figure 3.2.
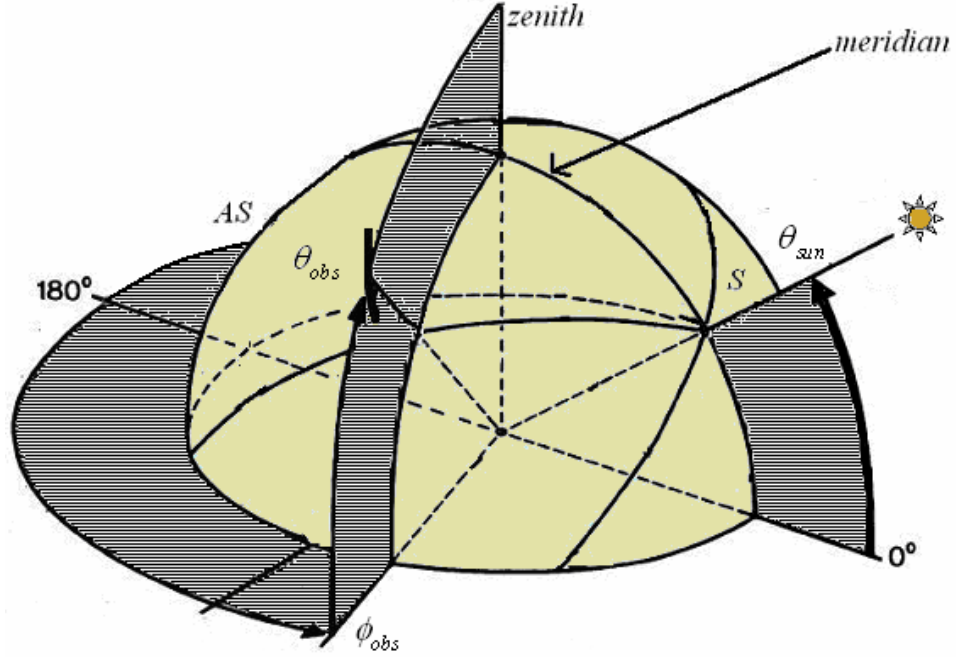
Figure 3.2: Sun related coordinate system for skylight polarization analysis.

The two important positions in such a system are the solar (*S*) location and the antisolar (A*S*) location, where A*S* is 180° away from S on the great circle that originates at S. Therefore the AS point is below the horizon when the Sun is in the sky. Every observation point in the hemisphere of the sky is always referred to with respect to the solar location. The elevation angle is the angle measured from the horizon to the object of interest, which can either be the Sun $\left(\theta_{sun}\right)$ or any point of observation $\left(\theta_{obs}\right)$ on the hemisphere. The azimuth angle $\left(\phi_{obs}\right)$ is measured with the solar azimuth $\left(\phi_{sun}\right)$ as its reference.

3.3.2 Skylight polarization model

A Rayleigh scattering atmosphere that accurately models an atmosphere with negligible amount of aerosols is used to understand the skylight polarization model

30

(Coulson 1988) as it can be used to derive a closed form equation for both the degree and angle of polarization of skylight. This model assumes that the sky is clear with primarily Rayleigh scattering while it ignores the multiple scattering issues and elliptical or circular polarization. For the case of unpolarized incident sunlight the DOP of the scattered light is given by

$$\text{DOP} = \frac{\sin^2(\Theta)}{1+\cos^2(\Theta)} \tag{3.1}$$

where DOP is defined as a function of the scattering angle Θ. Figure 3.3 shows the angular distribution of the DOP for primary Rayleigh scattering with the DOP increasing from 0 to 1 from the center to the outer circle and the scattering angle is indicated on the outermost circle from 0° to 360°. It can be seen that the DOP shows a rotational symmetry around $\Theta = 0^\circ$ to 180° and also along $\Theta = 90^\circ$ directions. Here $\Theta = 0^\circ$ and $\Theta = 180^\circ$ correspond to the solar and antisolar locations if one can visualize the plot as a one-dimensional slice of the hemisphere of the sky. The two important observations here are the two unpolarized points that occur at the solar and antisolar locations and the completely polarized point that occurs when the radiation is scattered at $\Theta = 90^\circ$. Therefore it can be seen that the DOP values in the sky near the sun will be low and will radially increase and reach a maximum value near the right angle of scattering. Also, it is straight-forward to extend this model for the hemisphere of the sky where the DOP pattern will vary in a similar manner for the different scattering angles along both the zenith and azimuth angle directions.

31
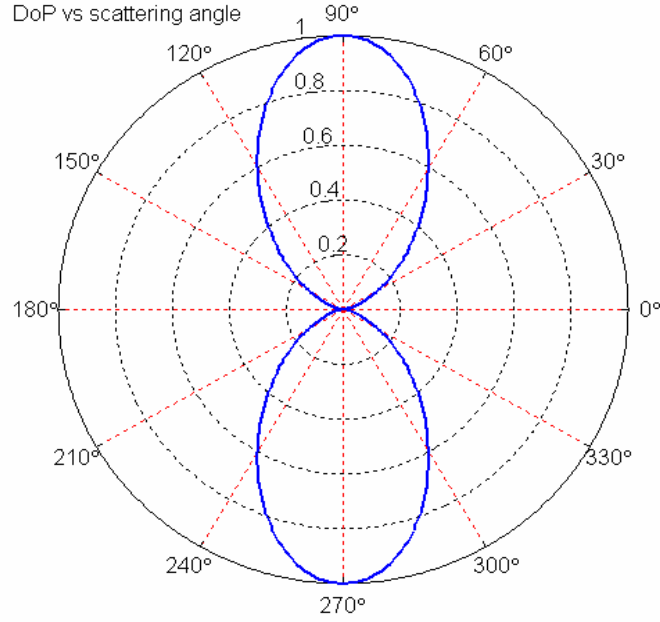
Figure 3.3: DOP of skylight due to primary Rayleigh scattering in the atmosphere as a function of scattering angle.

The AOP pattern (Matchko and Gerhart 2005) in the sky modeled using the Rayleigh atmosphere is given by

$$\cos(\text{AOP}) \;=\; \frac{\sin(\theta_{sun})\cos(\theta_{obs}) - \sin(\theta_{obs})\cos(\theta_{sun})\cos(\phi_{obs} - \phi_{sun})}{\{1 - [\sin(\theta_{sun})\sin(\theta_{obs}) + \cos(\theta_{obs})\cos(\theta_{sun})\cos(\phi_{obs} - \phi_{sun})]^2\}^{1/2}} \quad (3.2)$$

where θ_{sun}, ϕ_{sun}, θ_{obs} and ϕ_{obs} are the solar elevation, solar azimuth, observation elevation and observation azimuth respectively in a global coordinate system. In general, AOP of horizontal and vertical polarization are 0° and 90° respectively, but a different convention is used here in skylight polarization analysis such that the vertical polarization is described using 0° AOP and horizontal polarization by 90° AOP. Figure 3.4 illustrates the AOP pattern over the hemisphere of the sky represented for the solar azimuth of 18° and solar altitude of 36.8°.

32
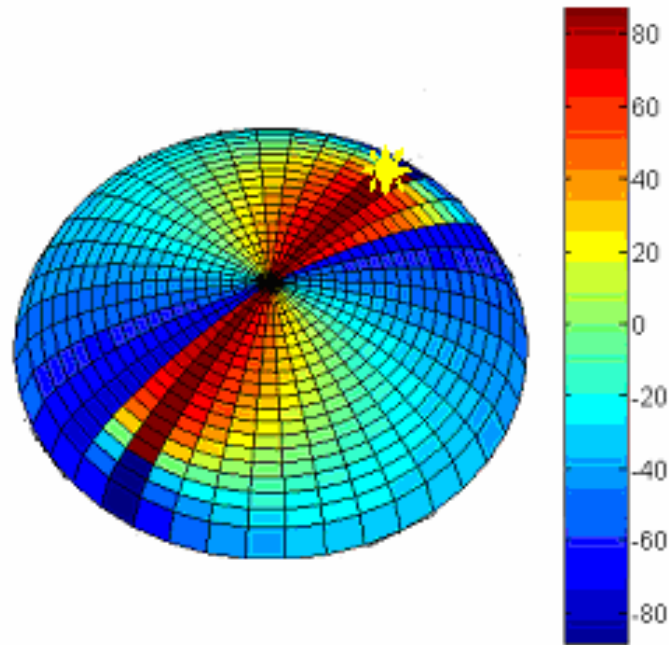
Figure 3.4: AOP distribution over the sky dome for Rayleigh scattering atmosphere for the solar azimuth of 18°and solar altitude of 36.8°.

Many animals orient themselves by using the sun as a compass (Brines 1978; Horváth and Varjú 2004). When the sun is hidden behind vegetation or the horizon, these animals are found to infer the position of the sun from the distribution of the angle of polarization obtained from restricted regions of clear sky. Honey bees, for example, which often fly with most of their field of view obscured by vegetation, can orient themselves correctly even if a small spot of the sky is visible. This indicates that for clear skies, the angle of polarization pattern is quite regular and depends mainly on the position of the sun. In order to explain the dynamics of the pattern of AOP in the sky as a function of geometry we use the bee's celestial map (Rossel and Wehner 1982) as a reference, which is presented in Figure 3.5.

33
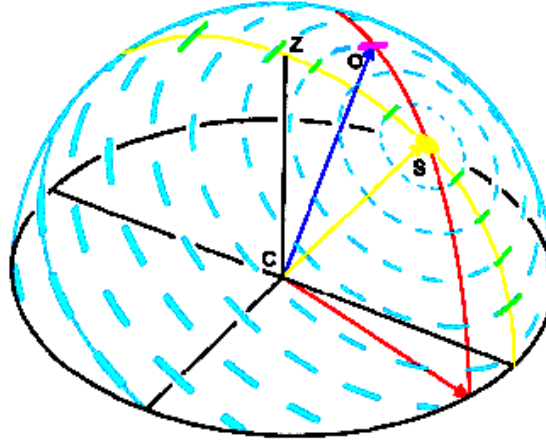
Figure 3.5: Bee's skylight AOP map.

In this representation, the orientation and thickness of the blue dashed lines indicate the AOP directions and the DOP magnitudes with the observer located at C inside the hemisphere of the sky with the local zenith at Z. The AOP at O (point marked in pink) can be found to be perpendicular to the scattering plane (red curve) defined by the solar location S, observer location C and the observation point O. Along the plane of solar meridian which is defined as the plane containing the local zenith and the solar and antisolar locations (yellow curve) the AOP values are found to remain constant and is also perpendicular to the plane of measurement irrespective of the elevation of the sun. Therefore the solar meridian is usually employed as a reference plane for the AOP description. Integrating the information that was derived from the bee's AOP map and the AOP model distribution over the sky dome presented in Figure 3.4, we can observe that the AOP values on the solar meridian are 90° (horizontal polarization). Also the AOP pattern is found to contain the zero cross over point when the scattering angle is 90° beyond which the AOP pattern undergoes a sign change at the same time maintaining the symmetry.

3.3.3 DIRSIG skylight polarization: Results and analysis

As DOP and AOP are heavily dependent upon the angle formed between the sun, the scattering object (in this case, a "piece of sky"), and the sensor, it is important to have a scene that both contains the entire sky dome and also gives us an explicit understanding of where any given pixel is located in the sky. For these polarized simulations, an experimental version of MODTRAN that predicts polarized scattered radiance (referred to as MODTRAN-P) was utilized. In order to verify that the output from MODTRAN-P is being correctly incorporated into DIRSIG, we must be able to visualize where any given pixel is located. While this ability is currently available in DIRSIG in the form of zenith and azimuth angle maps, it is still difficult to get a qualitative understanding of where any given pixel is located, particularly when the sensor is pointed at the sky. For these reasons, a test scene was created that consisted of large alphabetic letters constructed as physical 3-D objects in a CAD environment. The letters created corresponded to the cardinal compass directions, as well as the X and Y directions within the DIRSIG environment. A cube was suspended in mid-air above the center of the scene to indicate a zenith angle of 0°. The geometry was then placed on a large flat plate to represent the ground and create a horizon. The materials attributed to each object were basic materials drawn from the DIRSIG database and Figure 3.6 (a) depicts an overhead view of the scene.

Image data for the polarized atmospheric validation studies were rendered by a VNIR/SWIR pushbroom sensor, which was oriented vertically and swept 360° about the Z-axis. The sweep started and ended facing north (+Y). The sampling rate was configured such that there are three pixels for every degree of rotation, resulting in

images that are 1080 pixels across. The sensor was 1000 pixels in the vertical dimension and was configured with a field of view that extends from below the horizon to over 90° elevation angle, such that the sensor is seeing the sky behind itself. An illustration of the pushbroom sensor imaging the scene is shown in Figure 3.6 (b).

(a)   (b)
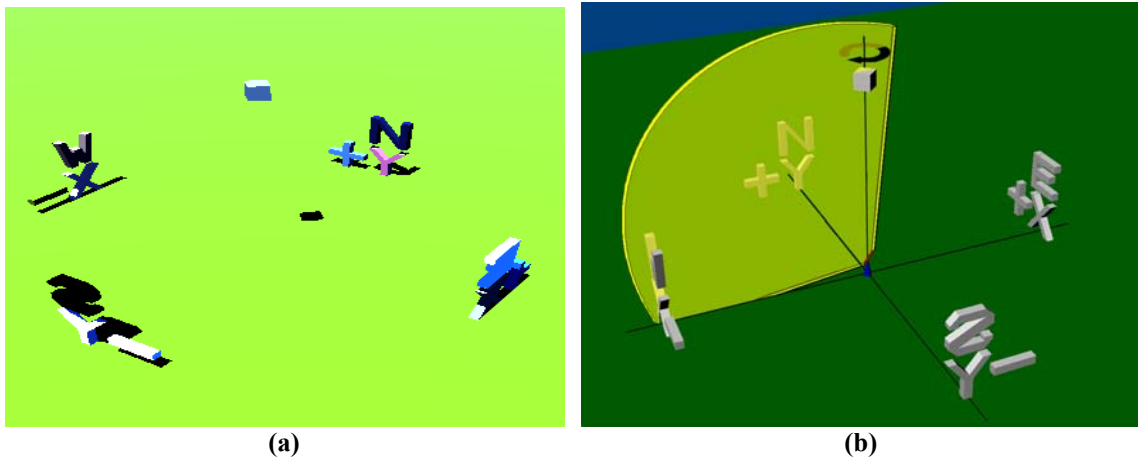
Figure 3.6: (a) Oblique RGB rendering of the DIRSIG scene used for atmospheric validation, (b) Illustration of the pushbroom sensor used in the atmospheric validation study. Note how the FOV extends beyond a zenith of 90°.
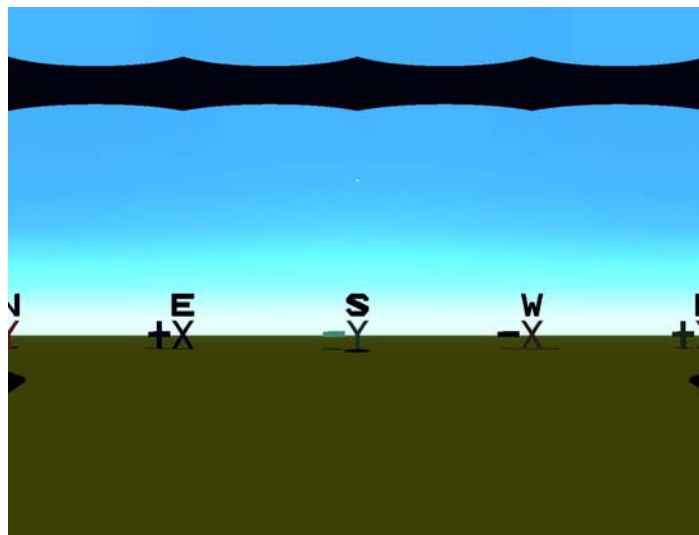
Figure 3.7: Panoramic RGB rendering of the DIRSIG scene used for atmospheric validation.

An RGB rendering of this 360° panoramic image is shown in Figure 3.7. The elongated object across the top of the scene is the bottom of the floating cube. The sun is

36

located due south, and can be seen above the large "S" object. The shadow of the cube is seen due north that is on the left and right edges of the scene as shown in Figure 3.7.

This test scene was then used in the simulations with 40km visibility of the atmosphere in MODTRAN-P to explore the variability of DOP and AOP across the atmosphere. By changing the latitude of the simulation, a qualitative comparison of the DOP distribution for high and low solar zenith is shown in Figure 3.8. It can be noticed that the DOP distribution varies in accordance with the theoretical model discussed earlier. When the solar zenith is high (or for low solar elevation in the sky) the DOP minima occurs above "S" and "N" objects corresponding to the solar and antisolar minima. In the low solar zenith case only the solar minima is shown because the antisolar minima occurs below the horizon. Also, in both cases the DOP maxima occurs at 90° scattering angle. The artifacts in Figure 3.8 (a) are attributed to the discrete sampling of the sky and the bi-linear interpolation currently used.

(a)   (b)
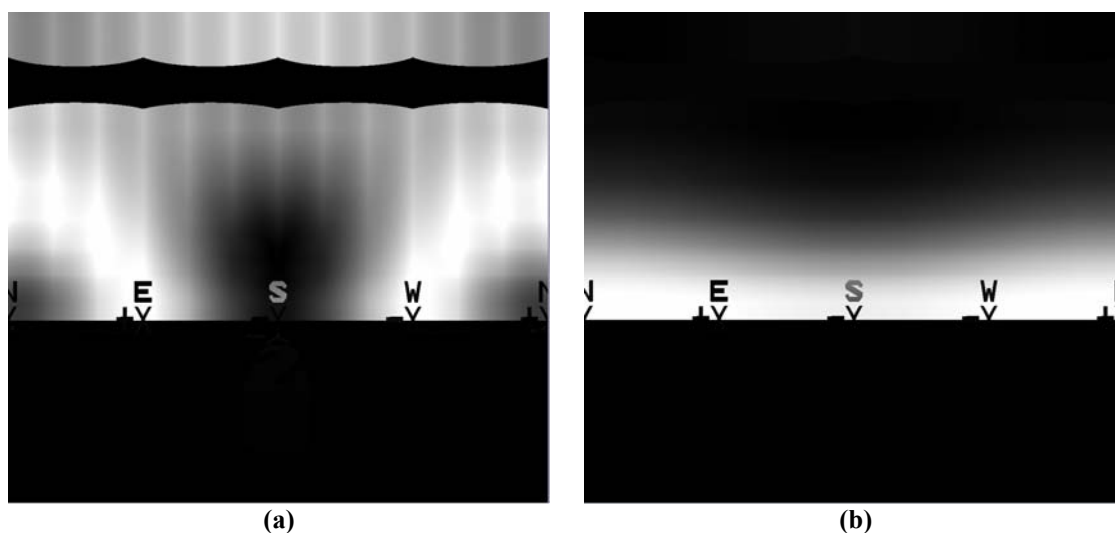
Figure 3.8: DOP distribution for (a) high and (b) low solar zenith.

To perform quantitative analysis, DIRSIG generated skylight polarization was compared with the data obtained from Coulson et al. (1960). Figure 3.9 presents the DOP distribution on the solar meridian at different times of day with solar zenith angles of 85.79, 43.51 and 19.56 at 0.65 μm. The plot illustrates that the DOP value reaches a maximum value at 90° scattering angle for all the three solar zenith (SZ) cases. Even though the absolute maximum value of DOP from DIRSIG data is found to be slightly lower than the Coulson data, the desired DOP variability for different observation zenith angles is observed. Any mismatch between the atmosphere used in the simulations and the Coulson data can lead to such deviations in the resulting absolute value differences.

In addition, the DOP distribution over the hemisphere for different observation zenith angles for high solar zenith case was investigated and the result is shown in Figure 3.10. DIRSIG data was simulated at 0.65 μm with the time of day at 6 am. The plot illustrates the variability of DIRSIG generated DOP at different observation zenith angles such as 80°, 65°, 40° and 10° and the data that Coulson observed at approximately the same observation zenith angles. It can also be seen that the DIRSIG predicted DOP values linearly increase with the observation azimuth and has a maximum value when the observation azimuth is 90° relative to the solar azimuth demonstrating its high correlation with the trends seen in Coulson data. When the observation zenith angle becomes smaller it can be seen that the DOP values are higher because the observation locations move farther from the solar location. Due to the rotational symmetry of DOP the data is plotted only over the half of the hemisphere.
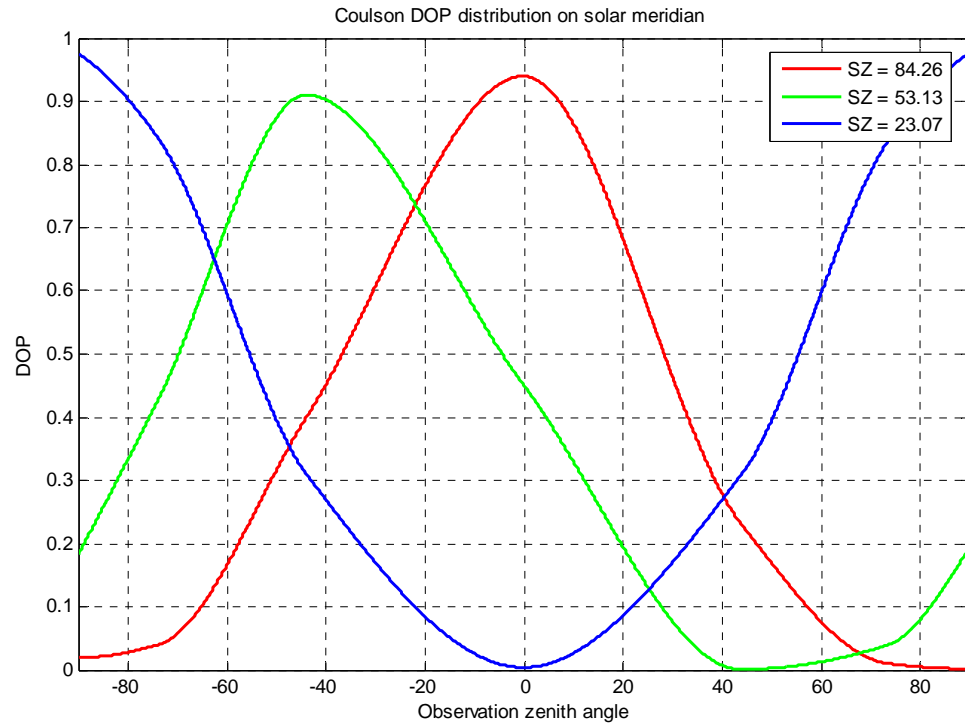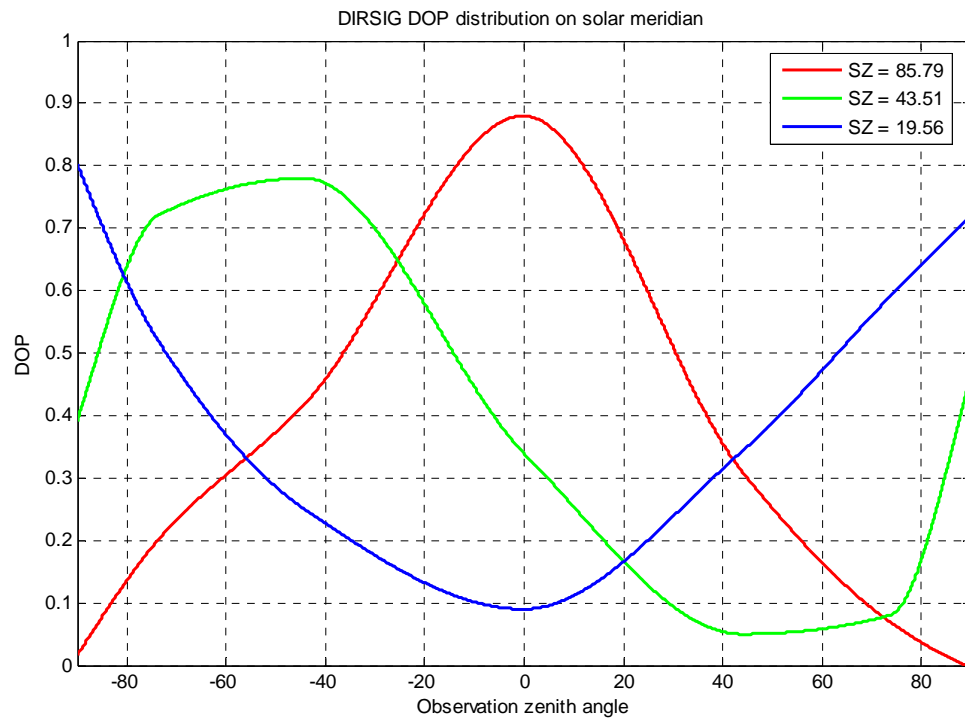
Figure 3.9: DOP distribution of (a) Coulson and (b) DIRSIG data on the solar meridian for different times of day.

Coulson DOP distribution over the hemisphere at SZ 84.3

Legend:
- OZ = 88.85 (blue)
- OZ = 73.73 (green)
- OZ = 43.94 (red)
- OZ = 16.26 (cyan)

DOP

Observation azimuth angle

(a)

DIRSIG DOP distribution over the hemisphere at 6am

Legend:
- OZ = 80 (blue)
- OZ = 65 (green)
- OZ = 40 (red)
- OZ = 10 (cyan)

DOP

Observation azimuth angle

(b)
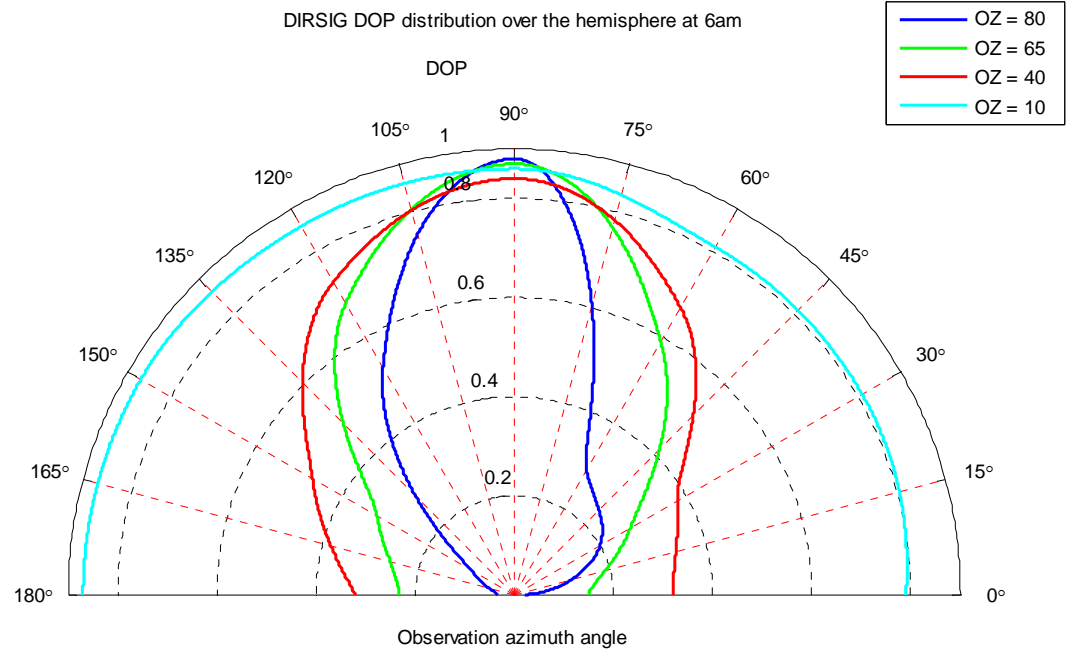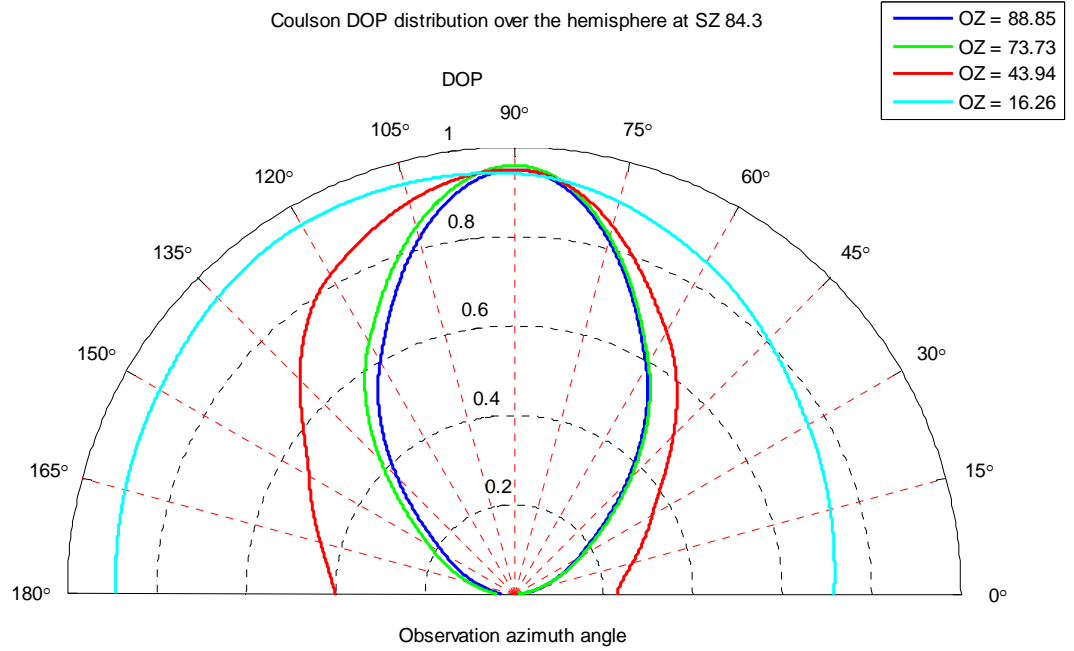
Figure 3.10: DOP distribution of (a) Coulson and (b) DIRSIG data over hemisphere for different observation zenith (OZ) for high solar zenith.
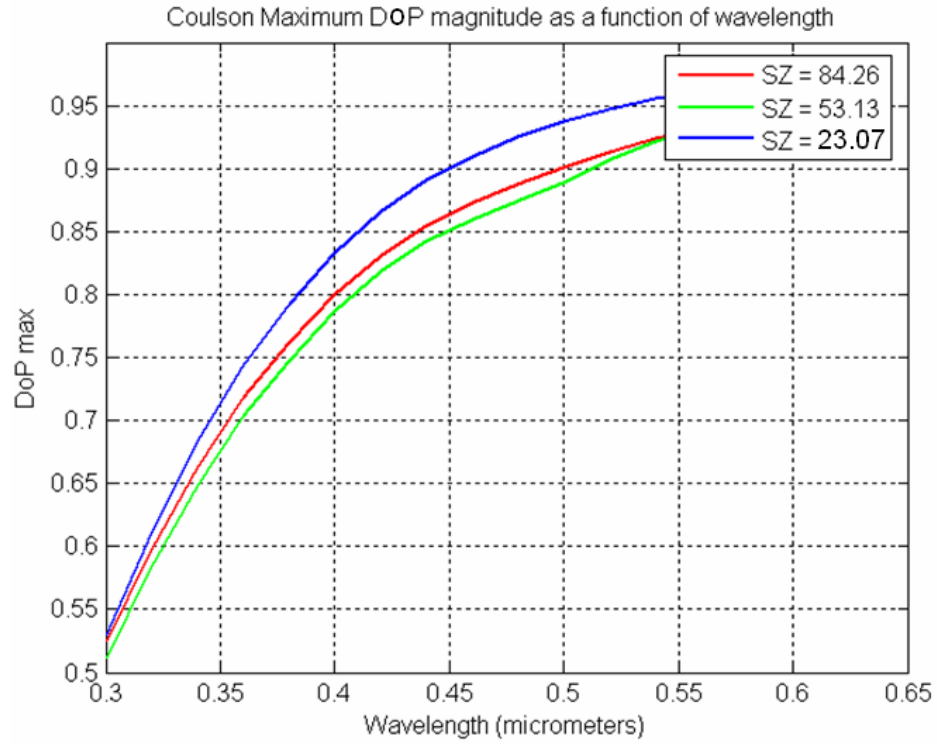
(a)
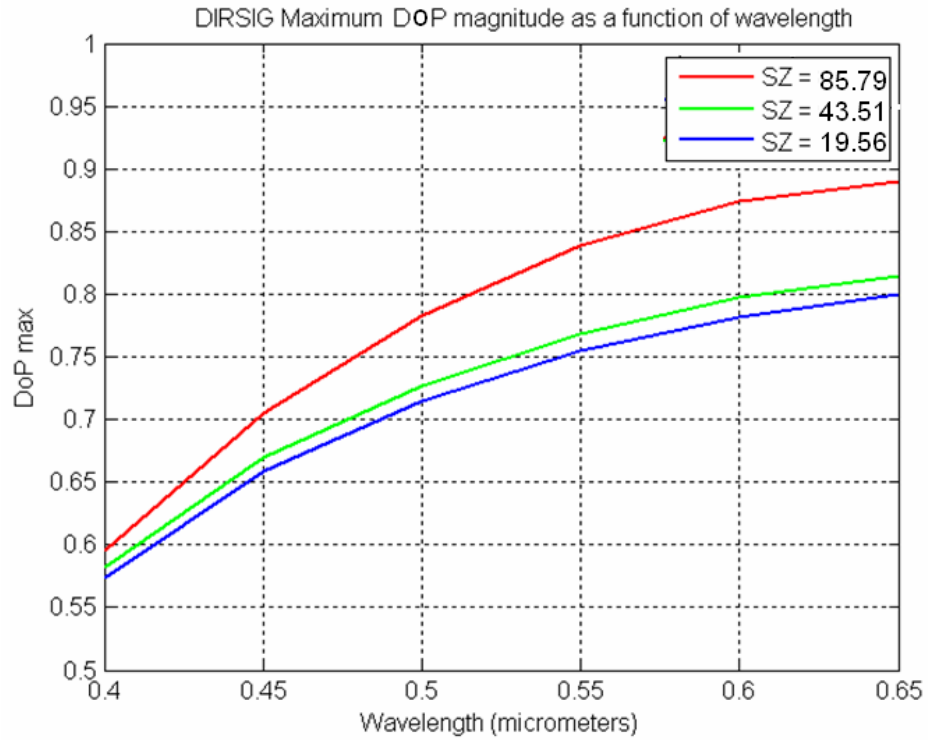
(b)

Figure 3.11: Maximum DoP vs. Wavelength of (a) Coulson and (b) DIRSIG data for different times of day.
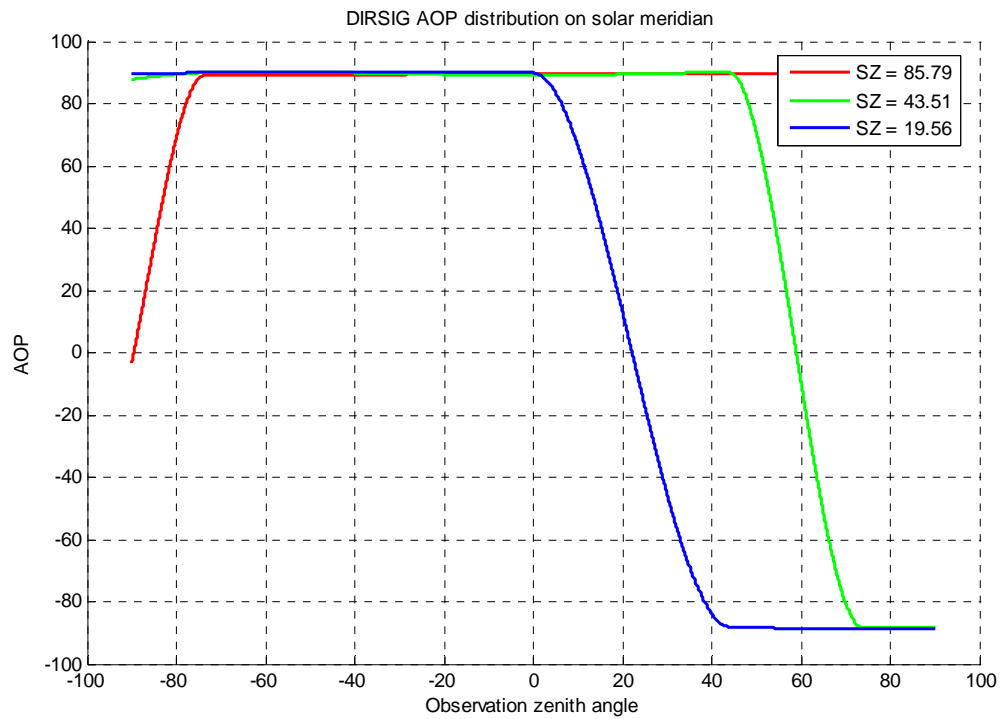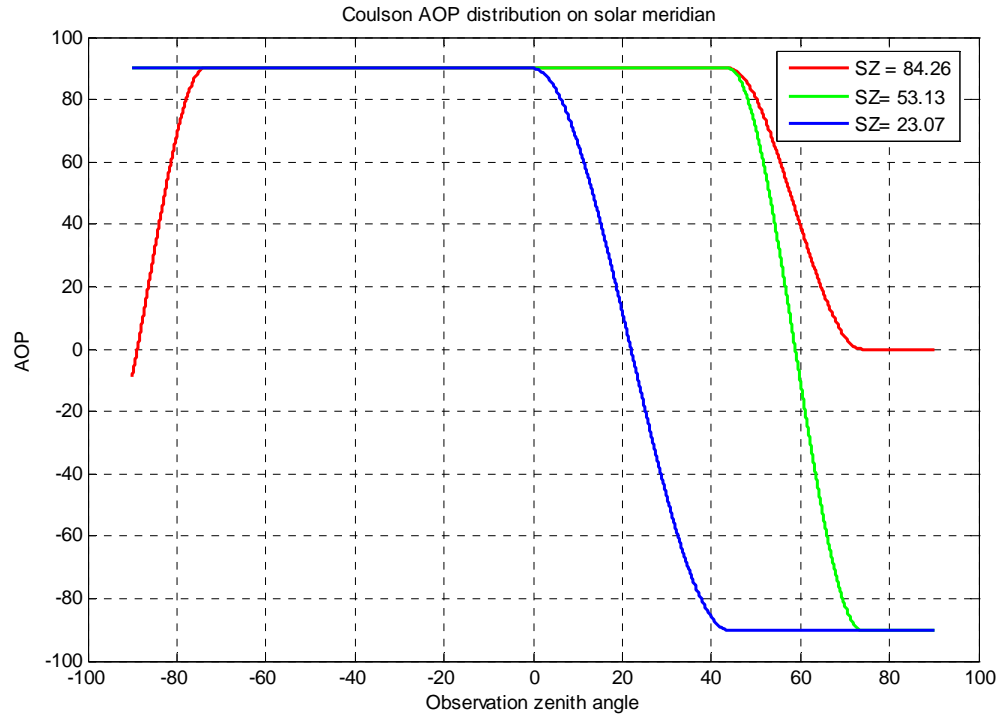
Figure 3.12: AoP distribution of (a) Coulson and (b) DIRSIG data on the solar meridian for different time of day.

The DOP variation as a function of wavelength is illustrated using the data generated between 0.4 and 0.7 μm for 6 am, 10 am and 12 pm cases. The results were compared with the Coulson data for different solar zenith angles ranging from low sun to high sun. Figure 3.11 illustrates the maximum DOP as a function of wavelength. Firstly it can be observed that the DIRSIG data is accurate in following a linear increasing trend across the spectral bands at all times, since the DOP maximum is expected to increase with increasing wavelength. Multiple scattering effects dominate the shorter wavelength region as compared to larger wavelengths.

In order to verify the AOP prediction capability we performed the analysis to show the AOP distribution on the solar meridian for different times of day. It can be seen from Figure 3.12 that DIRSIG is accurate in predicting the AOP values at all observation zenith angles on the solar meridional plane. The AOP values at all points above the sun location remains about 89° while the AOP has a sign change below the sun. The AOP distribution over the hemisphere for different observation zenith angles was also investigated. We verified that the AOP values are independent of wavelength (results not shown here). The results presented in Figure 3.13 indicate the AOP variation across the entire hemisphere observed at solar zenith of 84.26° with the corresponding DIRSIG data generated at 6 am. It can be noticed that the AOP at lower observation zenith tends to decrease from 90° gradually and crosses 0° at about 90° relative azimuth and increases to 90° when observed on the solar meridian plane with 180° relative azimuth angle. At 80° observation zenith angle, the AOP values are approximately 0° throughout the observation hemisphere. Based on all the observation in this analysis, the accuracy of integration of the polarized version of MODTRAN within DIRSIG is confirmed. It is

important to note that in this skylight polarization analysis, vertical polarization is described using 0° AOP and horizontal polarization by 90° AOP.

(a)

(b)
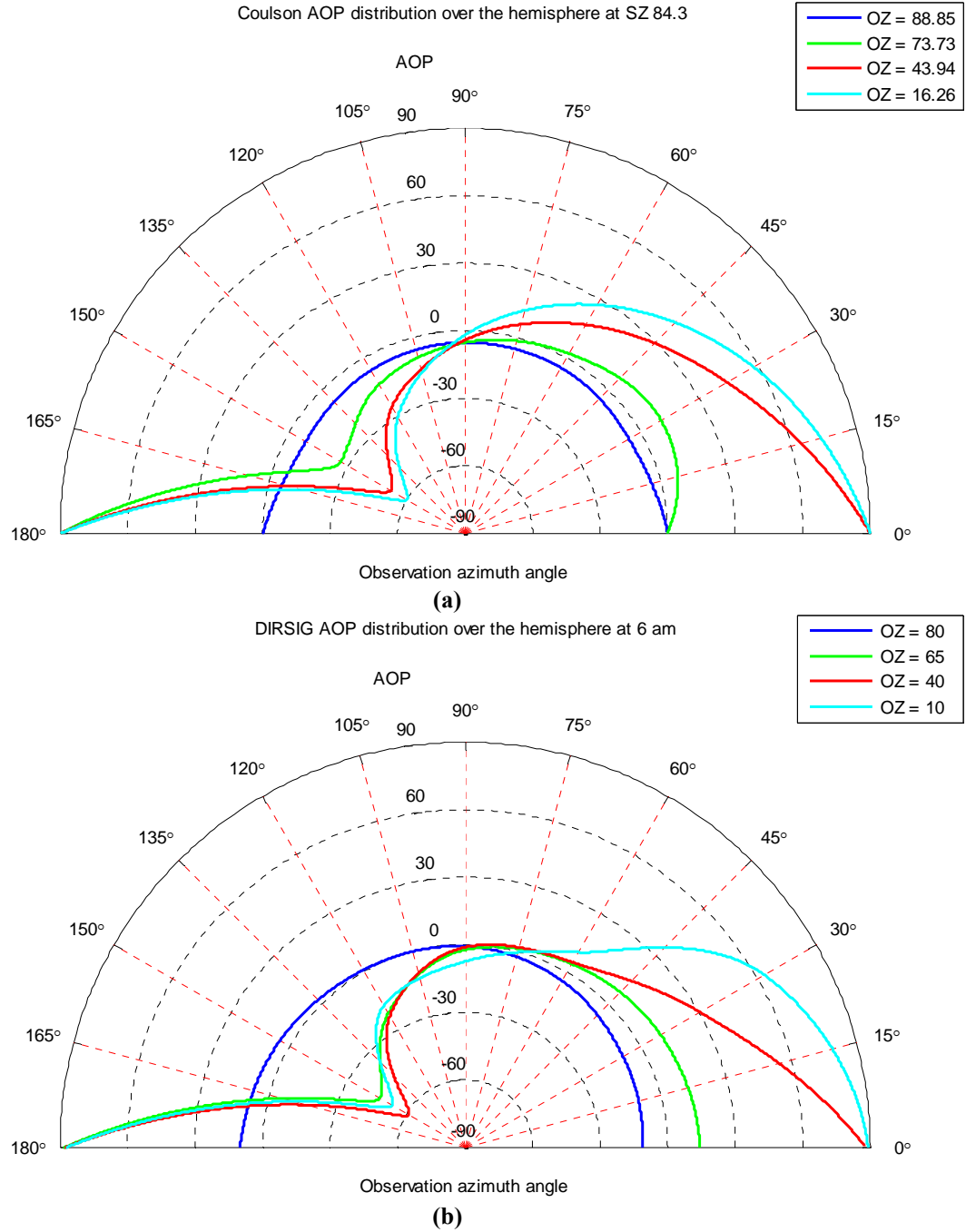
Figure 3.13: AOP distribution of (a) Coulson and (b) DIRSIG data over hemisphere for different observation zenith for high solar zenith.

3.4 Polarization by reflection

3.4.1 Surface reflected polarization

Surface reflection changes the state of polarization of the incident unpolarized light in such a way that the AOP of the reflected light will be vibrating in a plane that is parallel to the surface of the material (Schott 2009). As remote sensing applications involve reflection from the Earth surface, it is very important to understand the effect of reflection on the state of polarization in order to efficiently improve the surface characterization and discrimination using the polarimetric information. The orientation of linearly polarized light is defined with respect to the propagation direction and a reference axis that typically has some context in the real world (e.g. the "up" direction). The BRDF for a material is a function of the incident and reflected directions relative to the surface. In the case of a polarized BRDF, the polarization state (e.g. vertical linearly polarized light) is also assumed to be using the surface relative coordinate space as the reference (meaning the "up" direction is parallel to the surface normal). Once we attempt to model a surface in the context of a global coordinate system we must resolve the effects of the surface orientation within that global coordinate system. Consider vertical linearly polarized light incident on a surface that is tilted at 45° about an axis in-plane with the incident light. In the context of the tilted surface, the incident light is linearly polarized but the orientation is 45° rather than 0° (vertical).

To correctly reflect the radiation off a surface arbitrarily oriented in a global coordinate system we must address two effects. First, the global incident and reflected directions must be projected into the local coordinate space so that they can be used to access the BRDF. Second, the Stokes geometry of the global incident and reflected

polarizations must be translated into and out of the local coordinate space. The global to local vector projections required to evaluate the BRDF are common to any radiative transfer problem. However, the translation of the Stokes geometry is unique to polarized radiative transfer. To resolve the relative vs. global Stokes geometry problem, we need to establish a rotation that will translate the polarization state into and out of a surface relative coordinate system defined by the surface normal ($\hat{n}_{glob}$) in the global coordinate system as shown in Figure 3.14.

For a light path traveling in the direction $\vec{v}_i$, the P (vertical) and S (horizontal) polarization orientations will be defined so that P polarization state is perpendicular to $\vec{v}_i$, in the plane of the global up vector and its projection on $\hat{z}_{glob}$ is positive. The S polarization state is orthogonal to both the propagation direction and P such that $\vec{v}_p \perp \vec{v}_s \perp \vec{v}_i$.
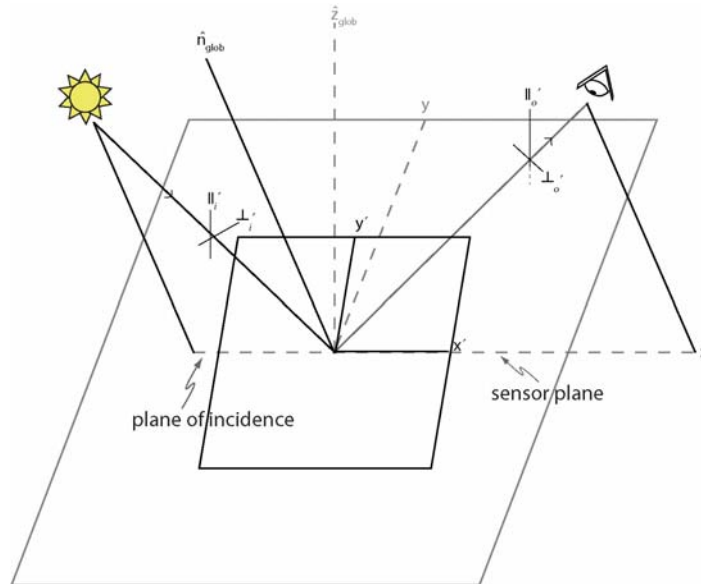
Figure 3.14: Global coordinate system containing a target tipped relative to the plane of Earth.

The rotation of the Stokes vector for incident light ($\vec{v}_i$) can be determined by computing the rotation of the vertical orientation from the global coordinate system into the local coordinate system. This is accomplished by computing the angle between the surface "up" direction (defined by the surface normal, $\hat{n}_{glob}$) and the global "up" direction ($\hat{z}_{glob}$) in the plane orthogonal to the incident light. The calculation of this angle requires calculation of the S and P unit vectors of the incident light propagation direction as well as the facet normal vector projected into the S-P plane of the incident light ($\vec{n}_{i_{SP}}$) given by

$$\vec{n}_{i_{SP}} = \vec{v}_i \times \left(\hat{n}_{glob} \times \vec{v}_i \right), \tag{3.3}$$

$$\vec{v}_s = \hat{z}_{glob} \times \vec{v}_i \text{ and} \tag{3.4}$$

$$\vec{v}_p = \vec{v}_i \times \vec{v}_s \tag{3.5}$$

The incident rotation angle, α_i, can be computed as the inverse tangent of the ratio of the S and P components of the vector $\vec{n}_{i_{SP}}$ as

$$\alpha_i = \tan^{-1} \left(\frac{\vec{n}_{i_{SP}} \cdot \vec{v}_S}{\vec{n}_{i_{SP}} \cdot \vec{v}_P} \right) \tag{3.6}$$

In the above equations $\times$ and $\cdot$ indicate vector cross product and vector dot product respectively. This angle can be used to construct a Mueller matrix that will rotate the incident Stokes vector from the global Stokes geometry into the surface relative Stokes geometry,

$$M_{\alpha_i} = \begin{bmatrix} 1 & 0 & 0 & 0 \\ 0 & \cos(2\alpha_i) & \sin(2\alpha_i) & 0 \\ 0 & -\sin(2\alpha_i) & \cos(2\alpha_i) & 0 \\ 0 & 0 & 0 & 1 \end{bmatrix} \qquad (3.7)$$

The surface relative to global rotation angle for a similar reflective geometry (α_r) can be computed using the same approach. However, the rotation angle is opposite in sign compared to the similar incident geometry. The reflected polarized radiance (L_r) for polarized incident light is then

$$L_r = M_{\alpha_r} \cdot \left(M_{BRDF} \cdot \left(M_{\alpha_i} \cdot E_i \right) \right) \qquad (3.8)$$

where M_{α_r} is the local to global Stokes rotation matrix, M_{BRDF} is the Mueller matrix from the polarized BRDF for the incident/reflected geometry, M_{α_i} is the global to local Stokes rotation matrix and E_i is the incident irradiance defined in the global Stokes coordinate system.

3.5 Water surface reflected skylight at sunset

The polarization parameters of the reflected polarized light depends on the scattering angle formed between the sun, the surface normal, and the sensor. In addition, these polarization parameters are influenced by the polarization state of the incident light and the polarizing property of the surface. This complicates the task of DIRSIG reflection polarization verification as it involves several variables. Therefore validation of the reflection polarization was achieved by demonstrating that DIRSIG can precisely replicate the striking optical polarization phenomenon that occurs in nature at sunset

shown in Figure 3.15. This unique polarization pattern occurs at low solar elevation and the dark spot observed on the water body at 90° from the Sun is due to the reflection of vertically polarized skylight illuminating the surface.

The skylight polarization pattern for a clear blue sky indicates that the angle of polarization is always tangential with respect to the source and the degree of polarization increases radially from the source and reaches the maximum value at 90° (Figure 3.5). Therefore at sunrise or at sunset, the polarization along the entire horizon will be vertically directed. During the day, however, the direction of polarization depends on the location of sun and the point of observation in the sky. As mentioned earlier, surface reflection changes the state of polarization of the incident unpolarized light in such a way that the AOP of the reflected light will be parallel to the surface. In other words, the surface acts as a linear polarizing filter that transmits the polarization component of the incident light that is parallel to the surface. Also almost all flat materials transform the unpolarized light into horizontally directed linearly polarized light. However the degree of polarization depends on the type of material. In Figure 3.15, the unnatural dark spot observed on water at 90° from the Sun is due to the reflected polarization of the vertically polarized sky near the horizon at low solar elevation. It can be noticed that the vertically polarized incident light on still water is less strongly reflected than the other parts of the sky. Only the qualitative characteristic of this striking optical phenomenon in the natural environment is revealed in Figure 3.15.

(a)
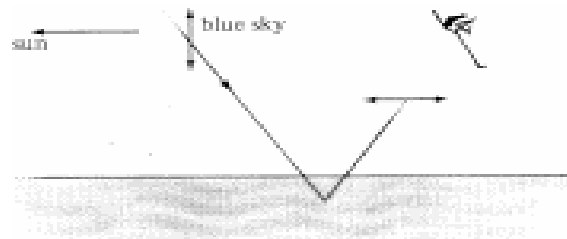
(b)

Figure 3.15: Reflection polarization process in nature (a). illustration (photograph from Können G. P, 1985). (b) Vertically polarized light illuminating the water surface.

Animal vision research reveals that many hydrophilic insects use their polarization vision to detect and identify water bodies (Schwind 1991). It was shown that the horizontally polarized ultraviolet light reflected from the surface of water is the main optical cue for habitat finding by these insects. The characteristics of the reflection polarization pattern on water were then quantitatively investigated (Horváth 1995) to model the change in water detectability of these insects. Results of theoretical prediction of DOP and AOP of Rayleigh skylight for different times of day are presented in Figure

50

3.16. The polarization pattern of the celestial hemisphere is represented in two dimensions using a polar coordinate system, where the angular distance from the zenith and the solar meridian are measured radially and tangentially. So the zenith is at the origin and the horizon is represented by the outermost circle. Here 'THETA SUN' is the solar zenith angle and in Figure 3.16 (b), the AOP is measured with local meridian as the reference instead of the solar meridian as in Coulson convention. Therefore for the case of THETA SUN = 0 Deg, the entire sky dome is horizontally polarized with respect to the local meridian. When the water is illuminated by unpolarized skylight (THETA SUN = 0 Deg), a simple polarization pattern of uniform horizontally polarized light will be observed. But when the sky is clear, complicated polarization patterns can develop due to superposition of the polarization characteristics of the water surface and the partially reflected polarization pattern of the sky light. By superimposing DOP and AOP images for the THETA SUN = 90 Deg case in Figure 3.16, it is easy to identify the specific patch of sky which is strongly vertically polarized.

A theoretical model of the Stokes vector of the reflected skylight on water (Horváth 1995) can be written as

$$S^{ref} = M^{ref} S^{sky} \qquad (3.9)$$

where the Stokes vector of the incident skylight is

$$S^{sky} = I^{sky} \begin{pmatrix} 1 & , & -DOP \cdot \cos(2 \cdot AOP) & , & DOP \cdot \sin(2 \cdot AOP) & , & 0 \end{pmatrix} \qquad (3.10)$$

and I^{sky} is the skylight intensity.
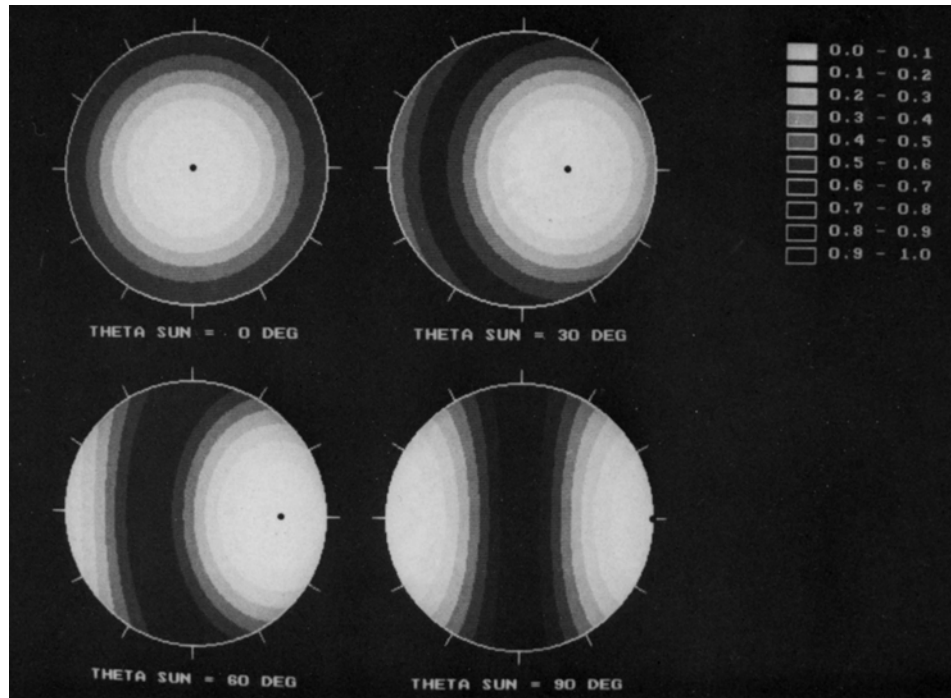
(a)
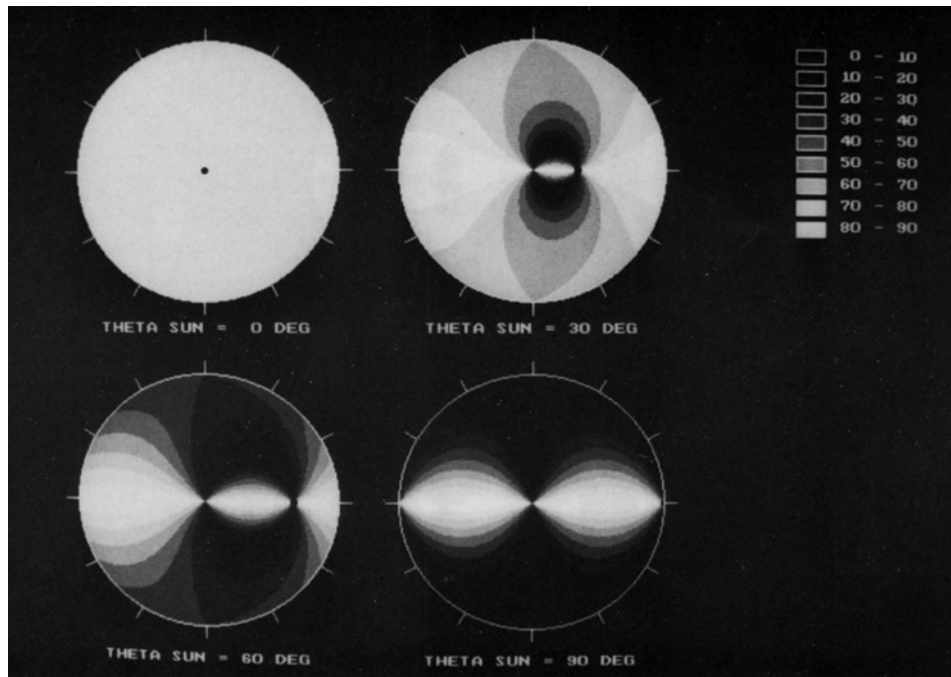
(b)

Figure 3.16: Theoretical prediction of Rayleigh skylight polarization (Horváth 1995) for different times of day (a) Degree of polarization pattern and (b).Angle of polarization pattern.

In equation (3.9) M^{ref} is the Mueller matrix of air-water interface, given by

$$M^{ref} = \frac{1}{2}\left(\frac{\tan(\Delta\theta)}{\sin(\Sigma\theta)}\right) \cdot \begin{bmatrix} T_1 & T_2 & 0 & 0 \\ T_2 & T_1 & 0 & 0 \\ 0 & 0 & T_3 & 0 \\ 0 & 0 & 0 & T_3 \end{bmatrix} \quad \text{with} \quad \begin{array}{l} T_1 = \cos^2(\Delta\theta) + \cos^2(\Sigma\theta) \\ T_2 = \cos^2(\Delta\theta) - \cos^2(\Sigma\theta) \\ T_3 = -2\cos(\Delta\theta)\cos(\Sigma\theta) \end{array} \quad (3.11)$$

where $\Sigma\theta = \theta_i + \theta_r$ and $\Delta\theta = \theta_i - \theta_r$ for angles of incidence (θ_i) and refraction (θ_r).
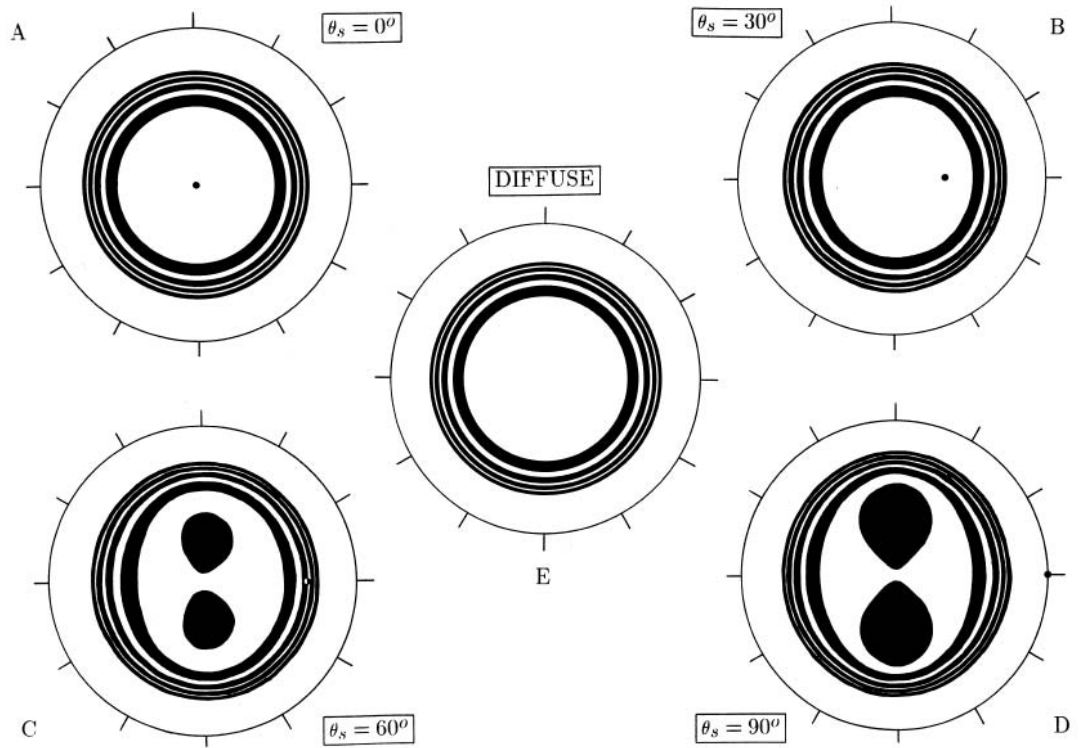
FIG. 7. Contour lines of equal reflectivity of a flat water surface under clear skies for different zenith distances θ_s of the sun (A–D) and for unpolarized light from an overcast sky (E). The position of the sun is indicated by a dot. In patterns (C) and (D), the two black patches represent the regions of the water surface where the reflectivity is less than 2%. In all patterns the contour lines belong to reflectivity values of 3, 4, ..., 9, 10% from the centre towards the periphery; the outermost circle (illustrating the horizon) represents a reflectivity value of 100%. For clarity every second reflectivity region is black.

Figure 3.17: Theoretical calculation of reflectivity pattern of flat water from (Horváth 1995).

Then the theoretical reflectivity pattern of the flat water surface can be calculated using

$$R = I^{sky}_{ref} / I^{sky} \tag{3.12}$$

where I_{ref}^{sky} is the intensity of water surface reflected skylight. Figure 3.17 shows the contour lines of equal reflectivity of flat water surface (Horváth 1995) calculated using equation (3.12) for different times of day. It can be noticed that as the Sun approaches the horizon, these contour lines elongate perpendicular to the solar meridian and the two symmetrical patches appear on the water surface at 90° from the Sun.

3.5.1 DIRSIG water surface reflected skylight polarization: Results and analysis

The accuracy of surface reflection polarization prediction of DIRSIG is verified using a simple scene within the DIRSIG simulation. The test scene contains a hemispherical shaped object of water and a large flat plate below the geometry to represent a nonreflecting ground. This ensures that the polarization pattern of the water surface is determined predominantly by the surface reflected skylight. A hemisphere of water was used in the simulation so that the reflection of the entire sky dome can be observed on the water surface in a single image. A polarimetric image at 450 nm was rendered at 5 am on a clear day using a nadir looking framing array sensor as shown in Figure 3.18.

The Stokes intensity component from the simulation, which corresponds to I_{ref}^{sky} in equation (3.12), is presented in Figure 3.19. DIRSIG predicted reflection polarization was compared with the theoretical reflection polarization pattern described by the Fresnel theory computed for single scattering Rayleigh skylight and with the measured real skylight reflected from the flat water surface (Gál et al. 2001). Striking resemblance in

the pattern can be noticed between the DIRSIG water surface reflected skylight intensity and the theoretical and measured reflection polarization pattern. It can be noticed that the two symmetrical and elongated patches appear on the water surface 90° from the Sun. In addition, the observed intensity pattern also slowly varies to reach its maximum value near the outer boundary of the water body. The additional elongation of the dark patch (highlighted in red) on the water surface is due to the hemispherical nature of the target (instead of flat water) that is being imaged. The fact that the DIRSIG simulated water surface reflected polarization pattern matches with the theoretical and measured pattern indicates the correctness of integration of skylight polarization and implementation of surface reflection polarization.
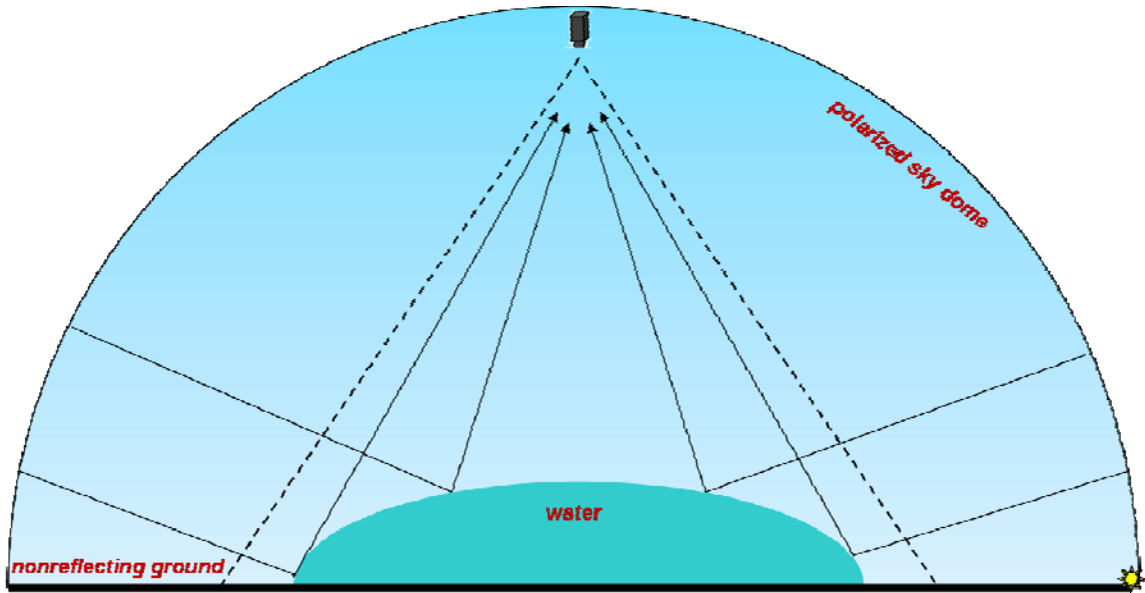
Figure 3.18: DIRSIG simulation setup for water surface reflected skylight analysis.
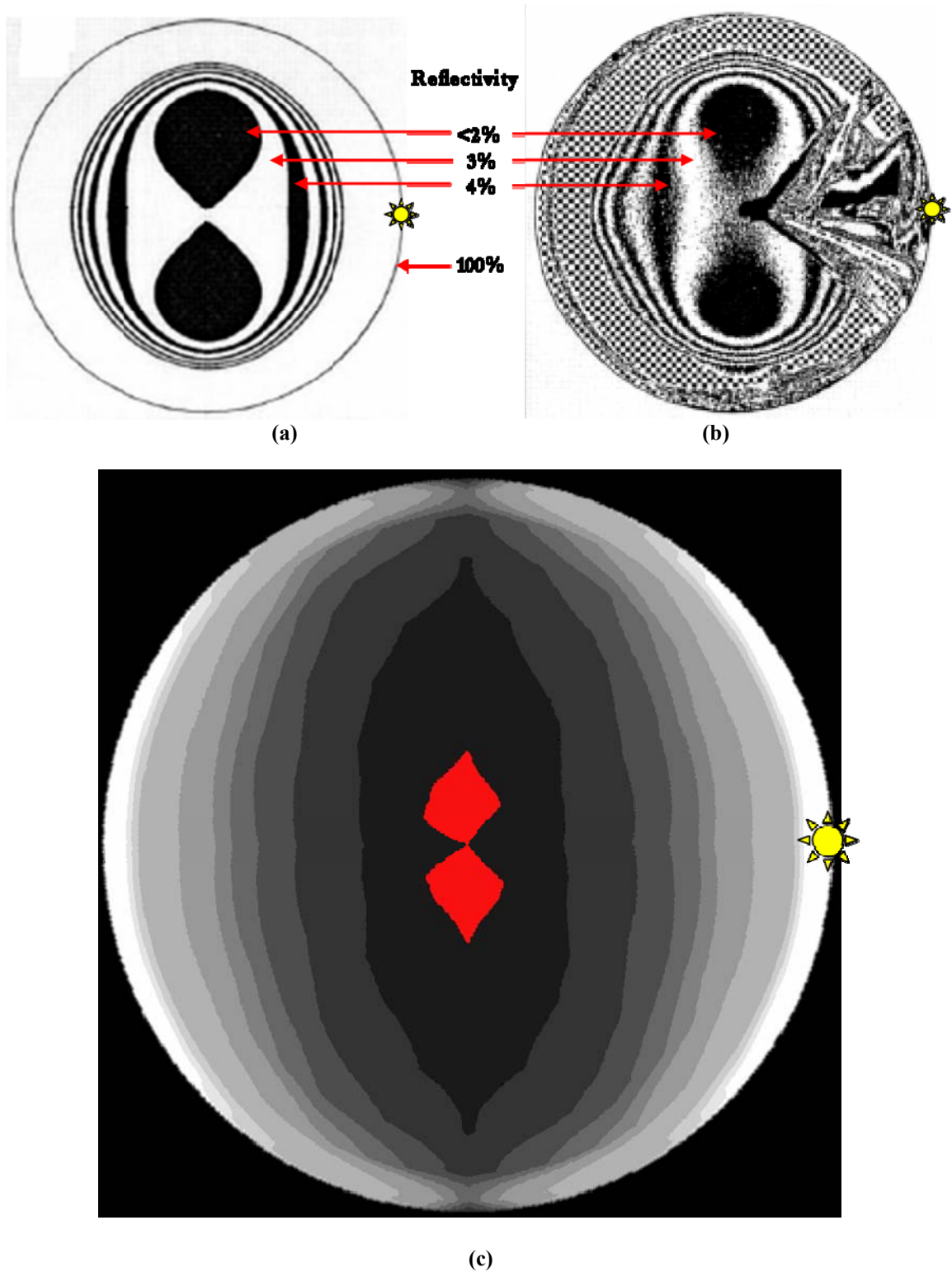
Figure 3.19: Water surface reflected skylight analysis (a) theoretical reflectivity pattern and (b). measured reflectivity pattern, and (c)DIRSIG water surface reflected skylight intensity pattern observed at sunrise.

3.6 Reflection polarization and object geometry

An unpolarized light wave becomes partially linearly polarized after being reflected, depending on the surface normal and the refractive index of the object surface it impinges on. The relation between the angle of refraction and the index of refraction of the surface is given by the Snell's law of reflection as

$$\hat{n}_a \sin \theta_i = \hat{n}_b \sin \theta_r \qquad (3.13)$$

where $\hat{n}_a$ and $\hat{n}_b$ are the refractive indices of material a and b, for angles of incidence (θ_i) and refraction (θ_r). As discussed in Section 2.4.2, Fresnel's theory gives the relationship between the partial polarization of a surface reflected wave and the angle of refraction. The interfaces of smooth objects cause less diffuse reflection and the incident and reflection angles will be equal. Therefore at any given angle of incidence, the degree of polarization of reflected light can be calculated using equation (2.18). It should be noted that this angle is always measured with respect to the surface normal and therefore will vary across the object surface.

In addition, no surface in reality is perfectly smooth in which case the microfacet model (Priest and Germer 2002) assumes that such a surface is a collection of small, randomly oriented mirror like facets. Each microfacet acts as an ideal reflector obeying Snell's law of reflection and the Fresnel reflection theory. Also all microfacets are characterized by their normal vectors which are distributed symmetrically about the mean surface normal according to the slope distribution function. At any given point, out of all the microfacets that make up the surface, only the ones oriented at a certain angle will reflect light directly to the camera and this "certain angle" will always be a bisector of the

scattering angle. Therefore orientation of the reflecting microfacet can be determined if the incident and scattering angles are specified. This clearly indicates that the surface reflection polarization phenomenology can be utilized in determining the surface orientation.

Polarization vision models developed for industrial defect detection applications (Atkinson and Hancock 2006; Meriaudeau et al. 2008; Morel et al. 2006) utilized this relationship between the polarization images and the surface normals to inspect highly reflective metallic surfaces. Such approaches determine the surface orientations from the orientation of the plane of incidence (POI) and the reflection angle at each point on the object's surface, since the direction of reflection polarization is perpendicular to POI.
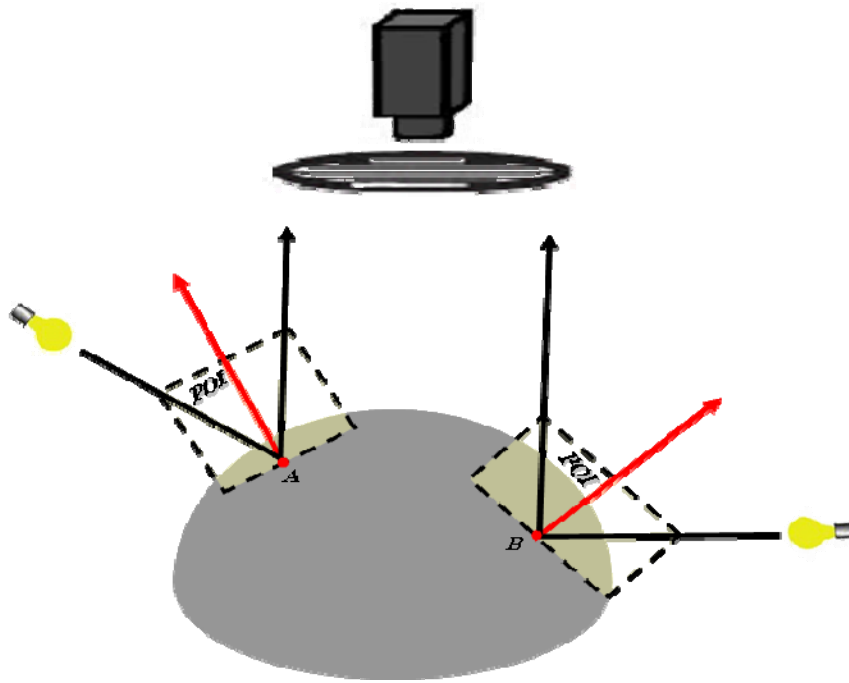
Figure 3.20: Reflection polarization and POI for different points on a hemispherical object.

In other words, an unpolarized light wave becomes partially linearly polarized according to the normal of the POI and therefore AOP can be inferred from the azimuth

58

angle of POI. A hemispherical object is convenient for establishing this relation between AOP and surface normals because it has a smooth geometrical appearance with continuously varying azimuth angle and also includes all surface normal directions. Figure 3.20 illustrates the location of POI for two points A and B on the object surface along with the illumination source for each point. It can be seen that POI location is also determined by the incidence angle at each point on the surface. In order to derive the intrinsic surface properties of the object using polarization, Miyazaki et al. (2004) enclosed the object within a spherical diffuser illuminated with multiple point light sources located around the sphere as shown in Figure 3.21. Such an arrangement with a nadir viewing camera system makes the viewing direction invariant across different observation points on the surface as shown in Figure 3.20. Therefore, the relative difference between AOP at any two points on the object surface will always be proportional to the relative difference between their azimuth angles.
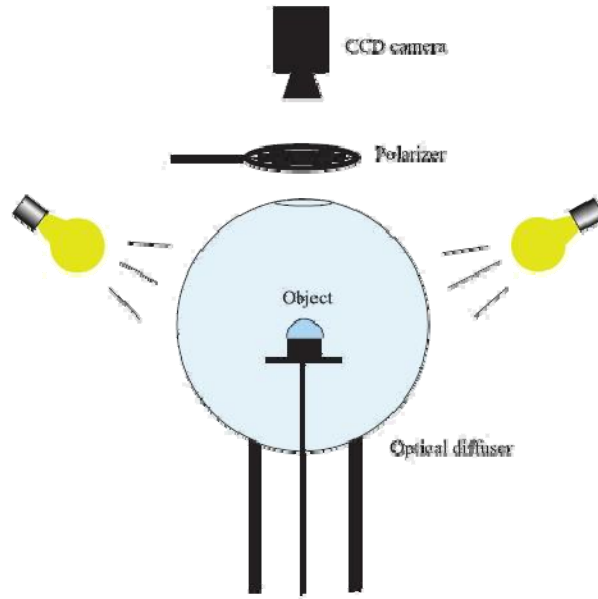
Figure 3.21: Experimental setup used for surface orientation estimation by Miyazaki et al. (2004).
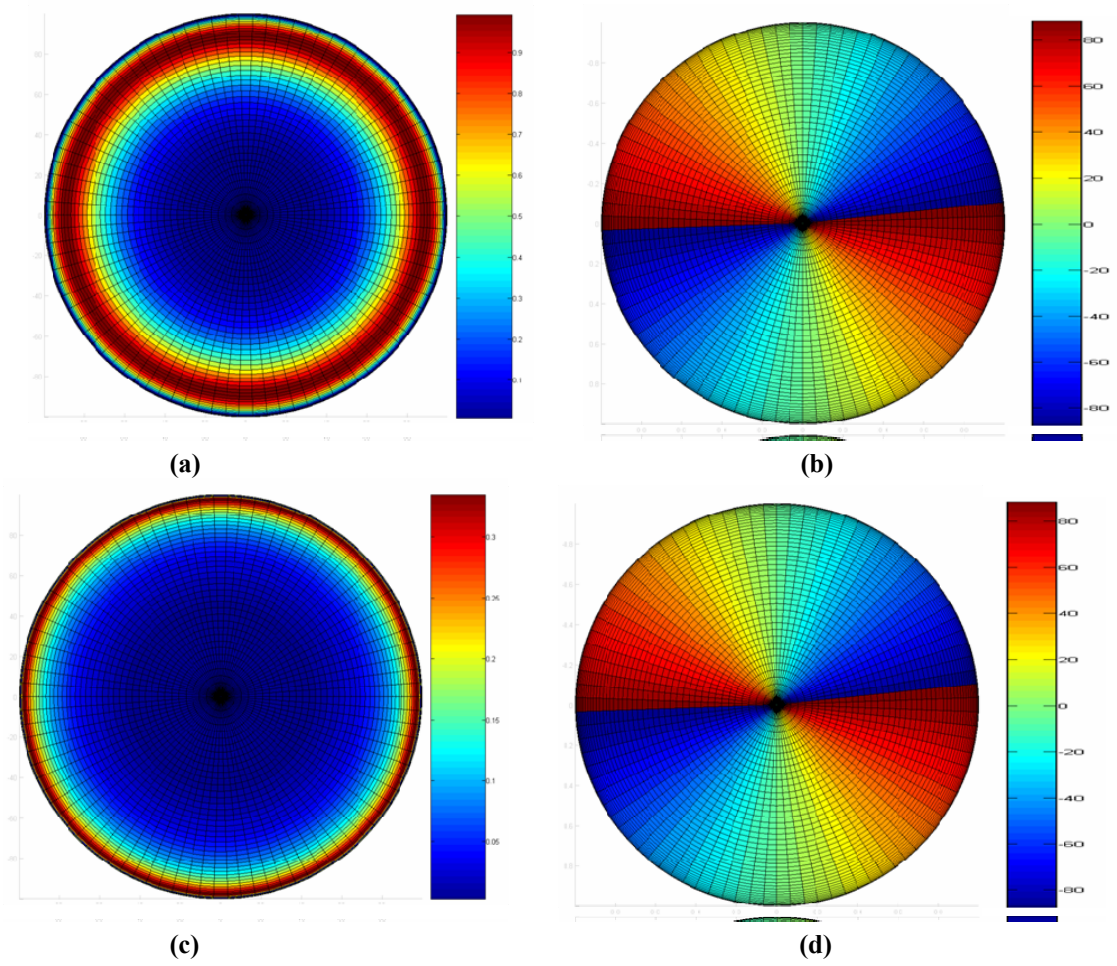
Figure 3.22: Theoretical model of polarization parameters for (a)-(b) glass and (c)-(d) aluminum.

Therefore the polarization parameters for dielectrics and metals can be theoretically predicted for such an arrangement with a nadir viewing camera system as shown in Figure 3.22. Here Figure 3.22 (a) and (c) correspond to DOP and Figure 3.22 (b) and (d) correspond to AOP for glass and aluminum. It can be seen that the AOP varies as a function of the azimuth angle of POI and is also independent of the material type. DOP, however, is a function of the normal of the POI and also depends on the refractive index of the material. And this results in the Brewster band in Figure 3.22 (a) at 56° for glass in addition to higher DOP values compared to aluminum shown in Figure 3.22 (c).

3.6.1 DIRSIG reflection polarization and surface orientation: Results and analysis

Validation of polarization parameters as a function of object geometry is demonstrated using a test scene that contains a painted hemispherical object as shown in Figure 3.23. The scene was illuminated by a uniformly diffuse sky dome to replicate the imaging setup in Figure 3.21. Since the object is placed on a black background, the lower part of the hemisphere will not have any source of illumination from a specular direction. So the sensor is placed at a zenith angle of 90° as shown in Figure 3.23, such that each point on the hemisphere is now illuminated by uniform unpolarized light. It can also be noted from Figure 3.21 that the object is placed on a raised platform in the laboratory so that the lower half of the hemisphere is lit by the multiple point light sources located around the spherical diffuser.
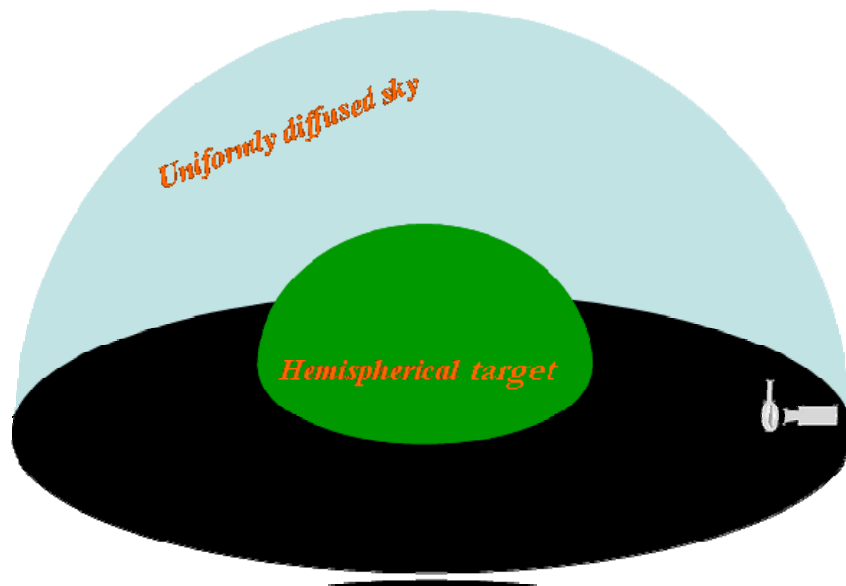
Figure 3.23: DIRSIG simulation setup for validating the relationship between surface reflection polarization and object geometry.

Table 3.1 Experimental design for DIRSIG validation of surface reflection polarization as a function of object surface geometry.

Hemispherical object illuminated by uniform unpolarized sky dome and sensor at 90° zenith			Phenomenology		
			DOP	AOP	
			Incidence angle	POI	
Material type	Dielectric/ metal	Glass	*Fresnel surface*		*Independent of material type*
		Aluminum			
	Glossy	Black	*Umov effect*		
		Green			
		White			
	Matte	Black	*Depolarizing effect*		
		Green			
		White			

The main objective here is to demonstrate the efficiency of DIRSIG in capturing the polarization phenomenology of different material types as a function of surface orientation. Table 3.1 presents the experimental design for the surface reflection polarization validation using the simulation setup shown in Figure 3.23. The results of DIRSIG simulated polarization parameters for this experiment are presented in Figure 3.24, Figure 3.25 and Figure 3.26. Since the sensor was located at 90° zenith angle, only half of the hemisphere comes within the field of view of the camera. So the observed images are comparable to the upper half of the circle shown in Figure 3.22. Fresnel surface reflection polarization phenomenology of glass and aluminum is illustrated in Figure 3.24. The relationship between DOP and angle of reflection can be easily identified, where DOP varies radially outward from the center of the object and is independent of the azimuth angle of the observation point on the hemisphere. It can be seen from Figure 3.24 (a) and Figure 3.24 (c) that dielectrics are highly polarizing

compared to bare metals. By comparing the DOP profiles of glass and aluminum in Figure 3.24 (b) and Figure 3.24 (d) with the entry angle profile in Figure 3.24 (f) it can be identified that glass has its maximum polarization of 0.8 around the Brewster angle while aluminum reaches its maximum polarization of 0.1 at higher reflection angles. Furthermore, it can be seen from Figure 3.24 (e) that the relative difference between AOP at any two points on the object is proportional to the relative difference between their azimuth angles. Figure 3.25 and Figure 3.26 illustrate the Umov effect observed in glossy materials and depolarizing effect observed in matte materials respectively. In Figure 3.25 and Figure 3.26, (a)-(c) correspond to DOP and (d)-(f) correspond to AOP of the hemispherical object in the scene. It is evident from Figure 3.25 and Figure 3.26 that AOP is independent of material type and is merely a function of the azimuth angle of the observation point on the hemisphere and therefore ranges between -90° and +90°. However, DOP is a function of both material type and angle of reflection. By comparing Figure 3.25 (a)-(c) it can be observed that glossy black surfaces are highly polarizing when compared to glossy green and glossy white surfaces. Also glossy black surfaces act as Fresnel surfaces as they are dominated by surface reflection component. This can be seen from Figure 3.25 (a) where DOP increases radially outward and reaches its maximum at the Brewster angle and then drops to zero at 90° reflection angles. By comparing the DOP of a particular colored paint in Figure 3.25 with the DOP of the same colored paint in Figure 3.26, it can be noticed that glossy surfaces are strongly polarizing when compared to matte surfaces. In this surface reflection polarization phenomenology analysis, AOP of horizontal and vertical polarization are 0° and 90° respectively.
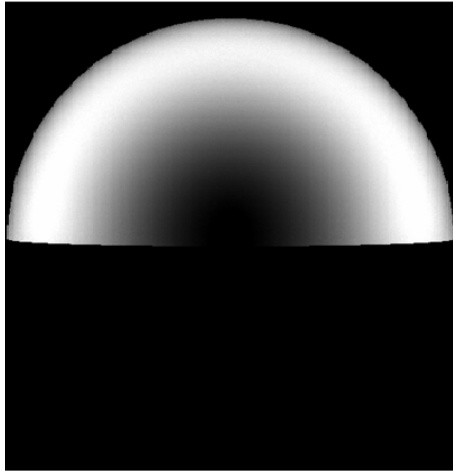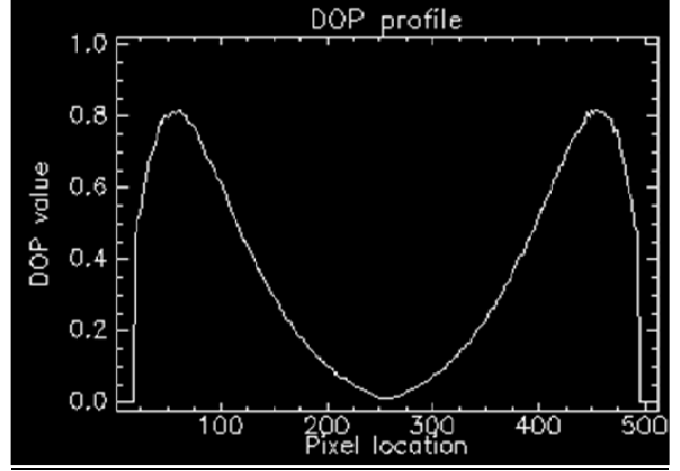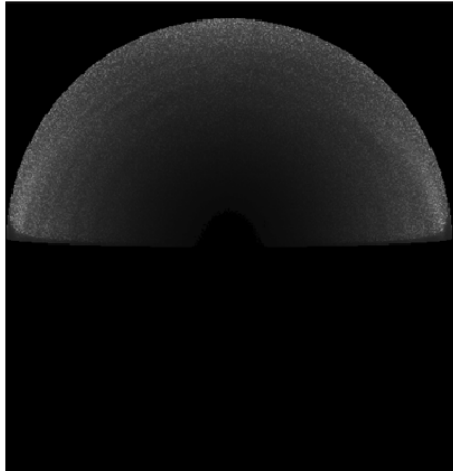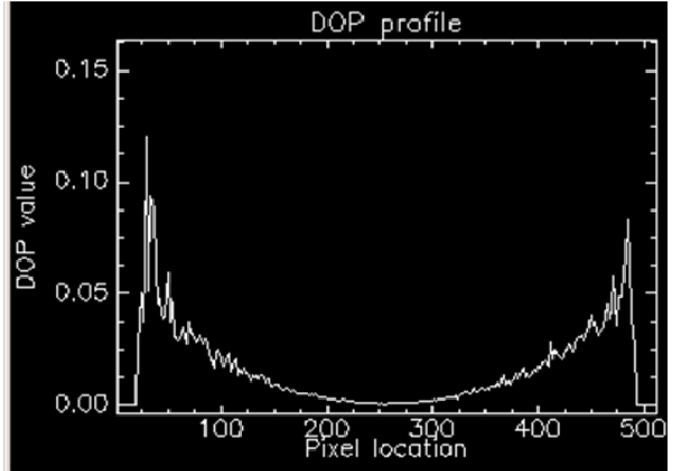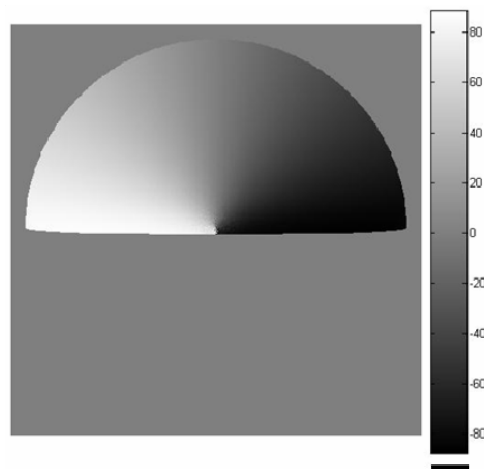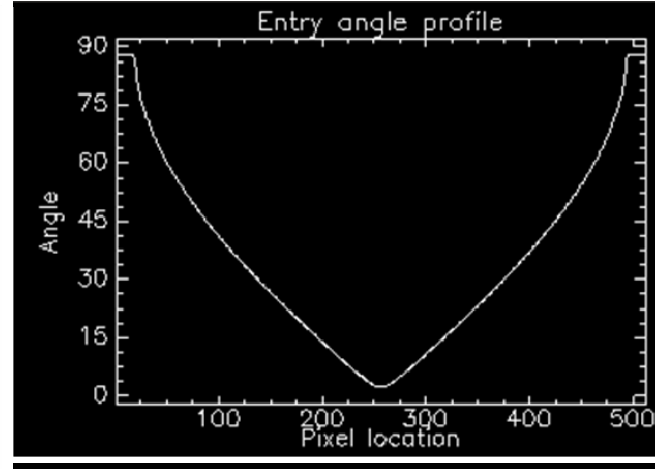
Figure 3.24: DIRSIG simulated polarization parameters for a hemispherical object: (a) - (b) DOP of glass, (c) - (d) DOP of aluminum, (e) AOP and (f) profile from the entry angle truth map.

64
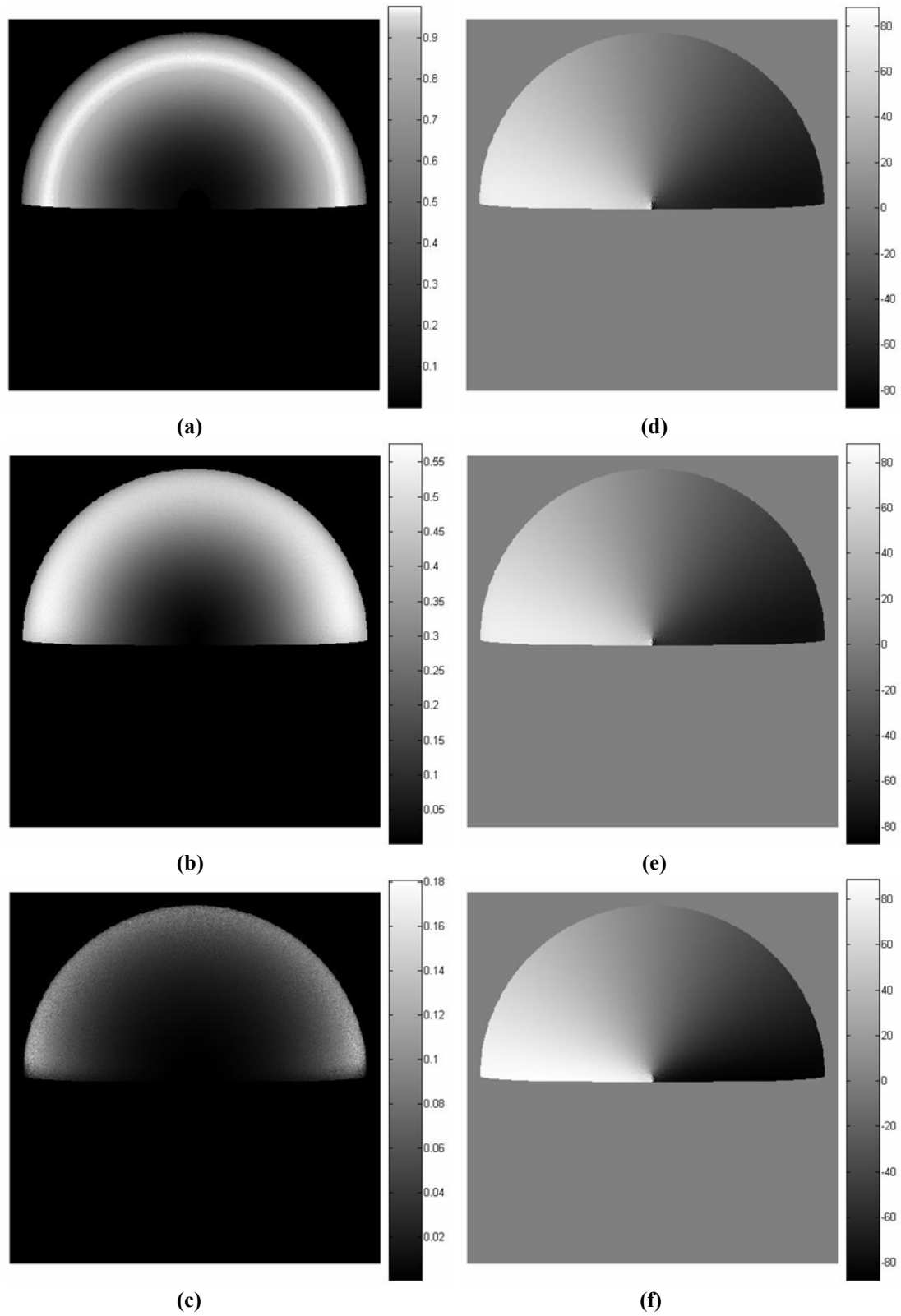
Figure 3.25: DIRSIG simulation of Umov effect using glossy hemispherical object: (a) - (d) black paint, (b) - (e) green paint, and (e) - (f) white paint.

65
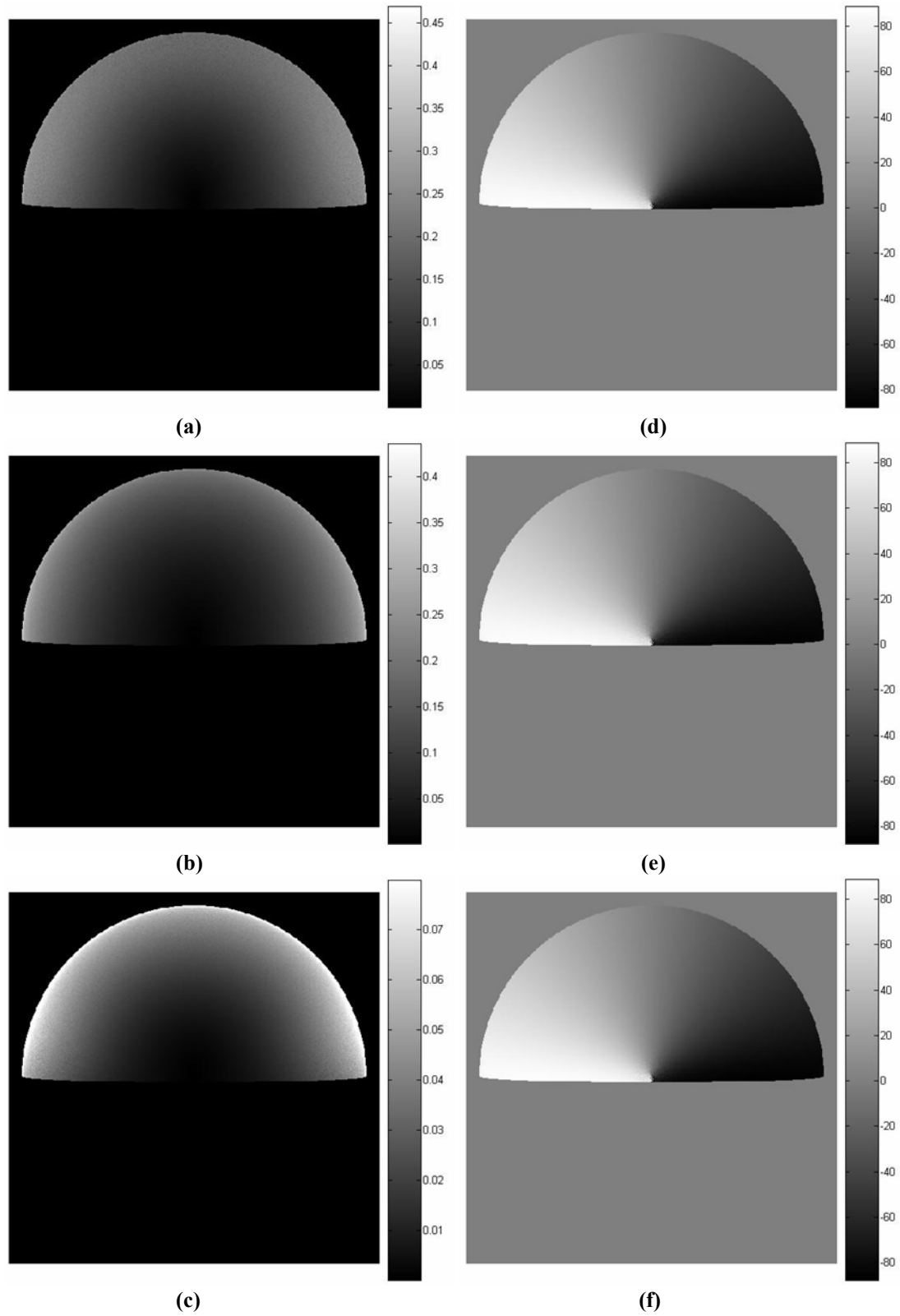
Figure 3.26: DIRSIG simulation of depolarizing effect using matte hemispherical object: (a) - (d) black paint, (b) - (e) green paint, and (e) - (f) white paint.

Table 3.2 DOP for a tilted surface at different view geometries.

| SENSOR LOCATION | | SURFACE ROTATION | | | θ_i | | DOP | AOP | |
AZIMUTH	ZENITH	θ_X	θ_Y	θ_Z	MODEL	DIRSIG	DIRSIG	MODEL	DIRSIG
0	20	0	0	0	20	20	0.15	0	0
0	40	0	0	0	40	40	0.65	0	0
0	60	0	0	0	60	60	0.96	0	0
0	20	0	20	0	0	0	0.00	0	0
0	40	0	20	0	20	20	0.15	0	0
0	60	0	20	0	40	40	0.65	0	0
0	20	0	-20	0	40	40	0.65	0	0
0	40	0	-20	0	60	60	0.96	0	0
0	60	0	-20	0	80	80	0.50	0	0
0	20	20	0	0	27.99	28	0.3	46.78	47
0	40	20	0	0	43.95	44	0.73	29.52	30
0	60	20	0	0	61.97	62	0.95	22.79	23
0	20	-20	0	0	27.99	28	0.3	-46.78	-47
0	40	-20	0	0	43.95	44	0.73	-29.52	-30
0	60	-20	0	0	61.97	62	0.95	-22.79	-23
0	20	0	0	20	20	20	0.15	0	0
0	40	0	0	20	40	40	0.65	0	0
0	60	0	0	20	60	60	0.96	0	0
0	20	0	0	-20	20	20	0.15	0	0
0	40	0	0	-20	40	40	0.65	0	0
0	60	0	0	-20	60	60	0.96	0	0

Lastly, the variability in DOP and AOP as a function of view geometry was verified. The test scene used in this DIRSIG simulation contains a glossy black painted flat plate which was tilted at different orientations with respect to the sensor. The sensor was located in the East (azimuth angle is 0°) at 3 different zenith angles (20°, 40°and 60°). Table 3.2 presents the list of different surface orientations used in the simulation and the observed DOP and AOP. Here the surface normal for $\theta_X = \theta_Y = \theta_Z = 0$ is parallel to Z axis. When $\theta_Y = +\Theta$ and $\theta_Y = -\Theta$ the surface normal is tilted Θ° towards East and

West respectively. Similarly θ_X tilts the surface normal in North or South direction and θ_Z rotates it circularly in the XY plane about the Z axis. The results presented in Table 3.2 indicate that DOP is a function of the reflection angle and AOP is a function of azimuth angle of the surface. It can also be recognized that these polarization parameters are independent of θ_Z. It can be seen that when the surface normal is tilted towards the North or South direction, there is a sign change in AOP, however, the magnitude of AOP remains unchanged. The polarimetric bidirectional reflectance distribution functions (pBRDF) of target materials in DIRSIG are modeled using Maxwell-Beard BRDF model (Maxwell et al. 1973). Scattering properties of materials are modeled through various parameters such as microfacet distribution functions, shadowing functions and volumetric contributions (Shell 2005). The surface reflection phenomenology validation results indicate a qualitative success of the pBRDF treatment in DIRSIG using glossy and matte painted surfaces. In other words, these results confirm the accuracy of DIRSIG in modeling the relationship between surface reflection polarization parameters and object geometry.

3.7 Upwelled polarization component

The upwelled radiance is the atmospheric component that is scattered into the sensor's line of sight without reaching the scene. Clearly this upwelled component is polarized and also depends on the location of sun and the sensor. Therefore the observed surface reflection polarization component will be modified according to the orientation of the surface and the magnitude and direction of polarization of the upwelled polarized atmospheric component.

3.7.1 DIRSIG upwelled polarization: Results and analysis

The main objective of this validation task is to confirm the accuracy of the calculation of the polarized upwelled term and its integration with the surface reflection polarization component. Here a traditional remote sensing calibration technique was used, which includes imaging a scene containing a near-zero polarization target such that the sensor reaching polarized radiance originates only from the upwelled component. DIRSIG simulations were performed to validate the dependency of the polarized upwelled component on the relative sun-sensor geometry for different times of day. Hemispherical observation of the scene was made in all cases to recognize the variability in polarized upwelled component due to changes in the view geometry. Observation zenith angle (θ_{obs}), measured with respect to Z axis, was sampled at every 10° interval between 30° and 80°. Sensor azimuth location (ϕ_{obs}) which is calculated relative to the source was sampled at 45° intervals. Table 3.3 presents the DOP of the upwelled component for Rayleigh scattering atmosphere for 6am and 12pm cases. It can be seen that the upwelled component is highly polarizing when the sensor is located at 90° with respect to sun for both 6am and 12pm cases.

Table 3.4 and Table 3.5 present the DOP of the upwelled component for multiple scattering atmosphere for different observation angles and distances from the target in the scene. Comparing Table 3.3 and Table 3.4, it can be seen that the polarization of the upwelled component depends on the atmospheric condition and as expected, the Rayleigh scattering atmosphere results in a strongly polarizing upwelled component compared to multiple scattering atmosphere. In addition the upwelled polarization component is directly proportional to the range from the target for a multiple scattering atmosphere,

69

which can be identified by comparing Table 3.4 and Table 3.5. These observations demonstrate that DIRSIG is correctly capturing the polarized upwelled component phenomenology.

Table 3.3 Upwelled DOP dependency on view geometry for Rayleigh scattering atmosphere.

UPWELLED DOP FOR SINGLE SCATTERING ATMOSPHERE									
TOD = 6am, RANGE= 1000m					TOD = 12pm, RANGE= 1000m				
Solar zenith angle = 80°, Solar azimuth angle = 73°					Solar zenith angle = 23°, Solar azimuth angle = 170°				
ϕ_{obs} / θ_{obs}	0°	45°	90°	180°	ϕ_{obs} / θ_{obs}	0°	45°	90°	180°
30°	0.398	0.574	0.902	0.752	30°	0.006 **AS**	0.064	0.221	0.465 **S**
40°	0.246	0.472	0.911	0.577	40°	0.041	0.118	0.328	0.645
50°	0.139	0.392	0.921	0.399	50°	0.106	0.204	0.466	0.811
60°	0.058	0.345	0.932	0.254	60°	0.206	0.325	0.624	0.924
70°	0.015	0.318	0.939	0.138	70°	0.342	0.476	0.780	0.935
80°	0.001 **AS**	0.316	0.943	0.05 **S**	80°	0.507	0.646	0.899	0.943

Table 3.4 Upwelled DOP dependency on view geometry for multiple scattering atmosphere.

UPWELLED DOP FOR MULTIPLE SCATTERING ATMOSPHERE									
TOD = 6am, RANGE= 1000m					TOD = 12pm, RANGE= 1000m				
Solar zenith angle = 80°, Solar azimuth angle = 73°					Solar zenith angle = 23°, Solar azimuth angle = 170°				
ϕ_{obs} / θ_{obs}	0°	45°	90°	180°	ϕ_{obs} / θ_{obs}	0°	45°	90°	180°
30°	0.049	0.082	0.130	0.120	30°	0.025 **AS**	0.066	0.011	0.114 **S**
40°	0.012	0.063	0.127	0.093	40°	0.062	0.045	0.058	0.159
50°	0.022	0.043	0.120	0.063	50°	0.048	0.001	0.097	0.181
60°	0.030	0.031	0.111	0.035	60°	0.001	0.045	0.120	0.180
70°	0.013	0.019	0.095	0.016	70°	0.041	0.074	0.121	0.154
80°	0.000 **AS**	0.014	0.076	0.004 **S**	80°	0.063	0.084	0.122	0.119

Table 3.5 Upwelled DOP dependency on range from the target for multiple scattering atmosphere.

UPWELLED DOP FOR MULTIPLE SCATTERING ATMOSPHERE									
TOD = 6am, RANGE= 10000m					TOD = 12pm, RANGE= 10000m				
Solar zenith angle = 80°, Solar azimuth angle = 73°					Solar zenith angle = 23°, Solar azimuth angle = 170°				
ϕ_{obs} / θ_{obs}	0°	45°	90°	180°	ϕ_{obs} / θ_{obs}	0°	45°	90°	180°
30°	0.144	0.207	0.297	0.233	30°	0.014 (AS)	0.029	0.068	0.199 (S)
40°	0.073	0.161	0.280	0.163	40°	0.036	0.003	0.123	0.261
50°	0.023	0.119	0.256	0.098	50°	0.015	0.045	0.175	0.294
60°	0.028	0.083	0.222	0.051	60°	0.035	0.095	0.209	0.283
70°	0.022	0.050	0.173	0.049	70°	0.078	0.125	0.208	0.228
80°	0.000 (AS)	0.028	0.117	0.005 (S)	80°	0.094	0.125	0.165	0.156

3.8 Summary

This chapter demonstrated that the prediction of the polarized radiance for remote sensing applications is complex. In addition to the unpolarized sunlight source, polarimetric remote sensing in the field also utilizes the polarized skylight as an illumination source. Hence, we provide a qualitative and quantitative comparison of skylight polarization of DIRSIG data with the Coulson data. Simulation of polarized imagery of real-world scenes requires coupling of the polarized illumination field with a geometric representation of the scene attributed with appropriate polarized BRDF characterizations. In order to verify the polarization due to surface reflection, water surface reflected skylight polarization analysis was performed. Furthermore, the relationship between surface orientation and the predicted polarization parameters was verified by analyzing DOP and AOP of a hemispherical object. The surface reflection polarization phenomenology validation results demonstrated a qualitative success of the

71

pBRDF treatment in DIRSIG using different glossy and matte painted materials. A traditional remote sensing calibration technique was used to verify the effects of upwelled polarization component on the observed surface reflected polarization. The results provide improved confidence in the synthetic polarimetric images generated using the DIRSIG model, which will now be used in Chapter 4 to investigate the impact of various scene related parameters on material discriminability in polarimetric images.

CHAPTER 4

Impact of polarization phenomenology on material discriminability in remotely sensed images

4.1 Introduction

Passive polarimetric remote sensing is an area of active research in a variety of applications. In particular, the use of polarization information has been shown to enhance the capability of detecting man made targets in remotely sensed images with natural backgrounds (Egan 2004). However, the influence of polarimetric system parameters on the detection capability has not been thoroughly investigated. Comprehending the underlying relationship between the system parameters and the polarimetric properties of materials will facilitate identifying the optimal imaging configuration for improved target discriminability. This complete understanding of the polarization phenomenology is critical in developing analysis procedures and also in improving polarimetric system design. Hence, this research aims to perform an in-depth analysis of an improved polarimetric system by relating target-background discriminability to various scene related parameters. Such a study, however, will require extensive polarimetric data measurements at various imaging configurations. In such cases, synthetic data generation

tools that can mimic real-world imagery with high fidelity are of great value. The proposed research objective is accomplished by utilizing the capability of DIRSIG in polarimetric image modeling and simulation. This chapter begins with a general description of a polarimetric imaging system, which is followed by a discussion of various polarization phenomenology related system parameters. It also presents a polarization physics-based approach for improving target-background discriminability and demonstrates the usefulness of the approach in improving detection performance in the absence of *a priori* knowledge about the target geometry.

4.2 Polarimetric imaging system description

The physical basis of a polarimetric remote sensing system consists of three major components, namely - (1) illumination source, (2) scene characteristics, and (3) observation geometry. A general representation of a polarimetric remote sensing system (Figure 4.1) includes illumination source (θ_s, φ_s), sensor (θ_v, φ_v) and object surface (θ_n, φ_n), characterized by their zenith angle θ_x and azimuth angle φ_x.

In addition to these geometrical descriptions, each component of the polarimetric remote sensing system is described through a set of fundamental optical parameters associated with the polarization phenomenology, which influence the polarization signature observed at the sensor. Furthermore, this variability in the observed polarized radiation from a remotely sensed surface will alter the material discriminability in polarimetric images.
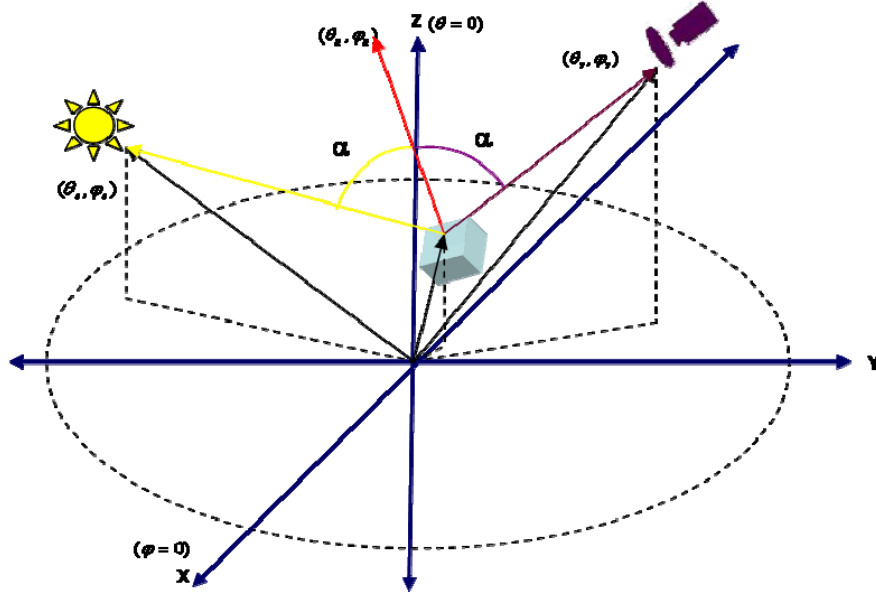
Figure 4.1: Polarimetric imaging system.

4.3 Polarization phenomenology and scene parameters

This section presents a detailed discussion on each of the previously mentioned system components with the corresponding optical parameters that will impact the polarization information contained in the observed scene.

4.3.1 Illumination source

The observed surface reflection polarization in remote sensing images is extremely sensitive to the polarization characteristics of light that illuminates the surface. Therefore it is important to identify the variation in the observed polarization properties of remotely sensed surfaces under different illumination conditions. Primary sources of illumination for polarimetric remote sensing in the natural environment in the reflective spectrum are sunlight and skylight. Transmitted sunlight is unpolarized since the exoatmospheric light from the sun is unpolarized and forward scattering does not impart

any significant polarization. However, the diffuse skylight can be highly polarized due to atmospheric scattering of the sunlight, which is found to vary over the sky dome. Daylight scenes are usually illuminated in three possible ways by (1) sunlight, (2) skylight, and (3) sunlight plus skylight as illustrated in Figure 4.2. The incident light on the surface is always unpolarized when the object in the scene is illuminated only by direct solar radiation. On a clear day when the surface is illuminated by a tangentially polarized skylight (Lee 1998), the observed polarized radiation will depend on the sky polarization pattern, which is a function of the solar location (θ_s, φ_s). Also additional multiple scattering introduced by haziness (Pust and Shaw 2008) in the atmosphere and the upwelled polarized radiance will introduce considerable amount of changes in the observed polarimetric imagery.
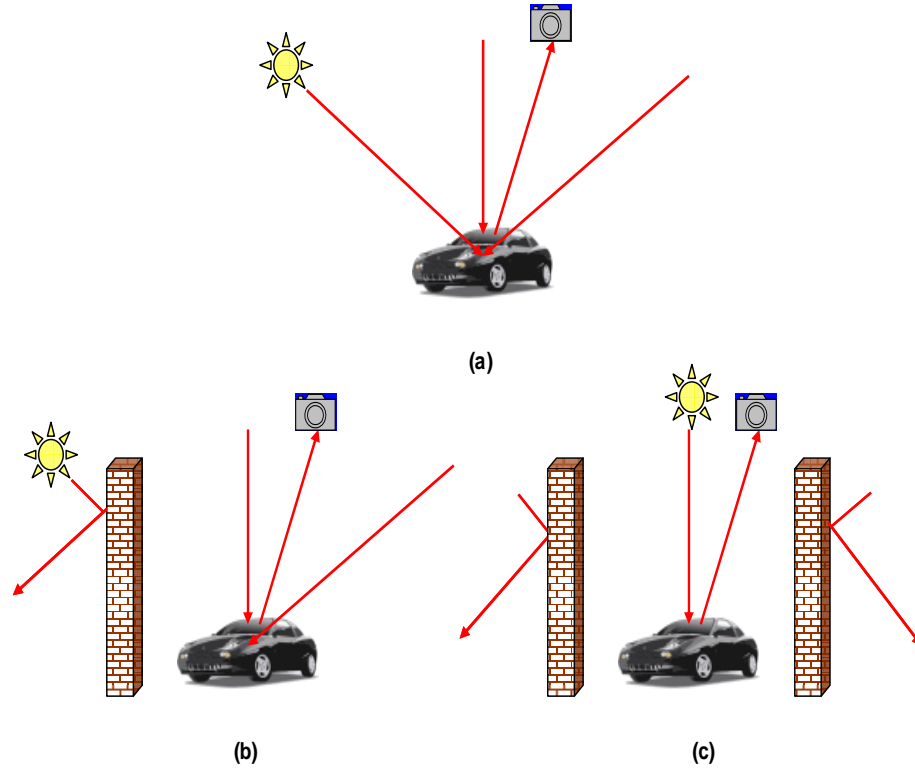
Figure 4.2: Illustration of different scene illumination types, (a) sunlight plus skylight, (b) skylight, and (c) sunlight.

4.3.2 Scene characteristics

Polarimetric remote sensing studies (Coulson 1966; Curran 1982; Genda and Okayama 1978) that aim at surface characterization and discrimination, deduce surface properties from the measurements of intensity and polarization of the reflected radiation. Scene contents induce variability in the observed state of polarization depending on the polarizing capability of the surface material. This can be attributed to the optical property of the surface represented by its index of refraction. In addition, the Umov effect (Umov 1905) tends to strongly polarize the darker surfaces as compared to the highly reflecting surfaces. The physical explanation for this effect is that the brighter surfaces are usually dominated by multiple scattering effects that reduce the polarization mechanism (Egan 1999). Furthermore, the surface roughness usually has a depolarizing effect on the polarization of the incident light (Curran 1978).

4.3.3 Observation geometry

Another key factor that changes the observed reflected polarized radiation is the geometrical aspect of the object, because the observed degree and angle of polarization of the reflected light is related to the orientation of the surface normal. This parameter that modifies the observed state of polarization is the scattering angle (α), which is defined by the angular distance between the original incident light and the surface reflected light. This compound angle (see Figure 4.1) is calculated using

$$\cos(2\alpha) = \cos(\theta_s)\cos(\theta_v) + \sin(\theta_s)\sin(\theta_v)\cos(\varphi_s - \varphi_v) \qquad (4.1)$$

where $\cos(\varphi_s - \varphi_v) = \pm 1$ for the in-plane geometry case.

It can be seen that for a given source position (θ_s, φ_s), α changes for different view geometries (θ_v, φ_v). This will indeed modify the observed polarized component of the reflected light. Consequently, this change in the observation geometry will also alter the material discriminability in polarimetric images. This effect, however, is not that pronounced in the observed intensity images as the unpolarized component of the reflected light from both target and the background varies with α in a similar manner. Therefore, the observation geometry is one of the key factors in target detection using polarimetric images.

4.4 Research methodology

Different materials respond differently at different sensing wavelengths and therefore acquiring images using a multispectral or hyperspectral systems enhances material discriminability more than using a single panchromatic image. Such systems conveniently assume the targets to be lambertian and therefore the target geometry can be ignored. In other words when a set of target spectra are collected to estimate the target statistics, the variability in the target's response comes solely from the atmospheric effects, sensor noise, etc. However in polarimetric imaging the observed polarization response is a function of the target scattering angles which depends on the relative orientation of the target surface with respect to the sensor. This indicates that if the imaged scene includes object geometries composed of multiple surface orientations such as a car then the observed polarization response of each pixel will vary as a function of surface orientation of the car.
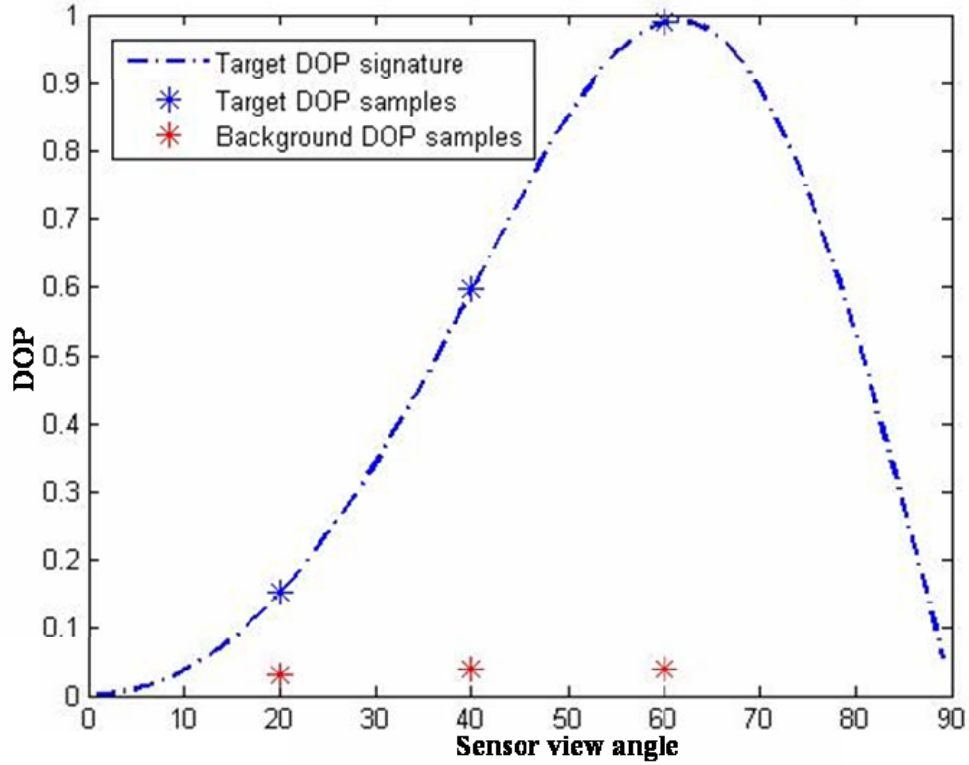
Figure 4.3: Observed polarization of target and background as a function of sensor view angle.

Figure 4.3 presents the observed polarization signature of a flat glossy black target panel and asphalt as a function of sensor view angle. As expected natural backgrounds are not polarizing and therefore asphalt has low DOP values and is also independent of sensor view angle. In this plot the target DOP signature corresponds to theoretical DOP of a flat glossy black target and target DOP samples correspond to the DIRSIG simulated DOP at a given sensor view angle. This plot also reveals that the target-background discriminability in DOP imagery can be maximized when the sensor is placed at the Brewster angle. However this angle is unknown and depends on the index of refraction and roughness of the surface in addition to the target surface orientation relative to the sensor. Figure 4.4 presents the scattering angles for different target surface orientations at a given sensor view angle and here the orientation of the target surface normal is

79

measured with respect to the sensor location. In other words, the sensor (zenith angle) is located at 20°, 40° and 60°on 0° azimuth axis marked on the plot. Therefore it can be seen that the scattering angle is 0° when the target surface normal is oriented such that it overlaps with the pointing direction of the sensor.
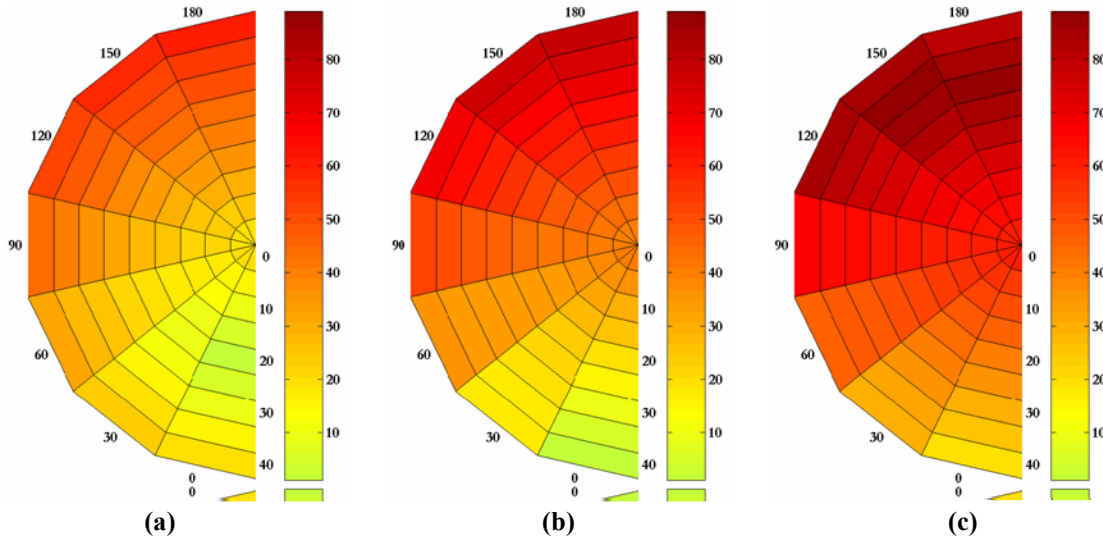
Figure 4.4: Target surface scattering angle at a given sensor view angle (a) 20°, (b) 40° and (c) 60°.

The influence of surface orientation on material discriminability in polarimetric images was investigated by quantifying the target-background discriminability and then analyzing the measured discriminability at various sensor view angles. In order to have a 'generalized' quantification of material discriminability, the well-known contrast metric (Gonzalez and Woods 2002) was used to measure the polarimetric dissimilarity for the target-background pair within the scene. A contrast metric is usually designed to measure the distinctness of a target from its background, assuming that high contrast values indicate easily detectable targets. The most common contrast metric is based on the absolute difference between the first order statistics of the target and the background and is given by

80

$$Contrast = |\mu_b - \mu_t| \qquad\qquad (4.2)$$

where μ_t and μ_b are the mean values of target and background in the observed image.

(a)   (b)   (c)
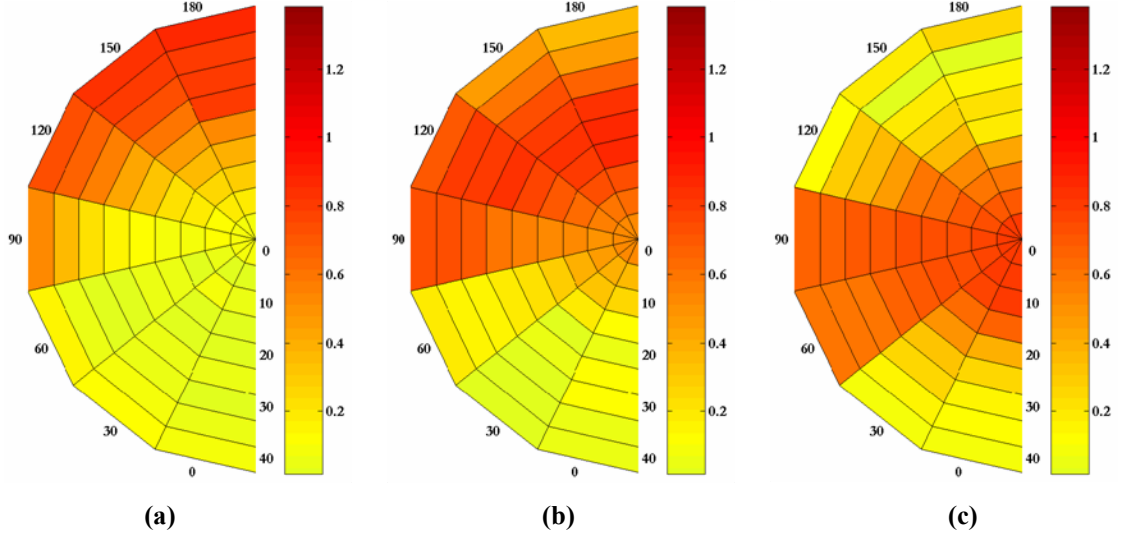
Figure 4.5: Target contrast at a given sensor view angle (a) 20°, (b) 40° and (c) 60°.

Figure 4.5 presents the observed target contrast of glossy black target on asphalt at different sensor view angles with uniform unpolarized sky dome illumination condition. In this plot each cell corresponds to a specific target orientation and is color coded with the measured target contrast. In fact there is high correlation between the scattering angles in Figure 4.4 and the target contrast shown in Figure 4.5. It can be seen that when the sensor is at 20° and 40° the observed target contrast increases for certain target orientations at which their surface normals are tilted away from the sensor resulting in higher scattering angles. Figure 4.5 (c) indicates that when the sensor is located at 60° zenith angle then the observed target contrast starts to decrease at higher scattering angles beyond the Brewster angle. This can be recognized from Figure 4.3 that the target

81

polarization decreases beyond the Brewster angle resulting in poor target contrast at those surface orientations.

(a)   (b)
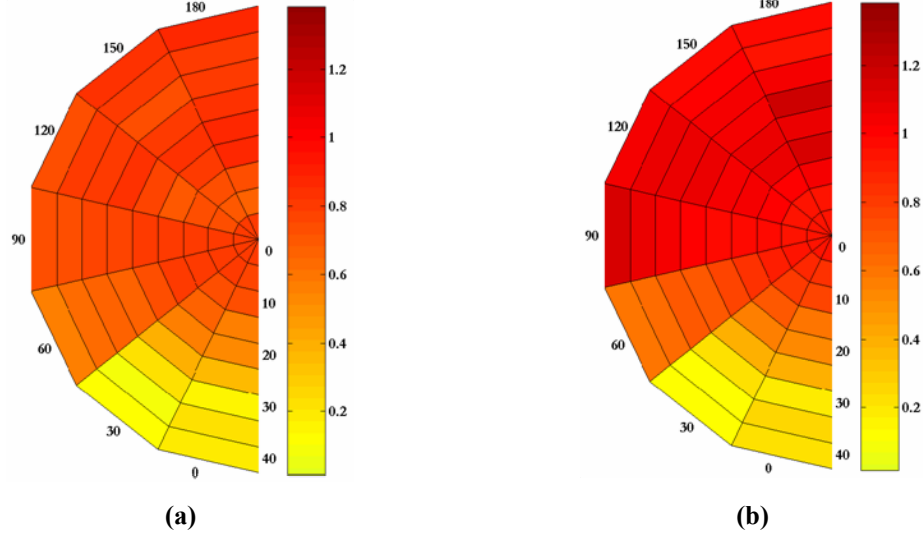
Figure 4.6: Target-background discriminability using (a) optimal single view and (b) multi view polarimetric imagery.

Figure 4.5 highlights the fact that a single view polarimetric image is not sufficient in detecting all the surface orientations. Figure 4.6 (a) presents the theoretical optimal single view performance in detecting each surface orientation; where for a given target orientation the image was acquired using a sensor location that maximizes the target contrast. In practical applications, however, a priori knowledge about the target geometry is usually not available and also the scene could include more than one surface orientation. In such cases, combining information from polarimetric images acquired at multiple view angles will be useful in improving target discriminability. Figure 4.6 (b) presents the target-background discriminability in multi-view DOP imagery for various target orientations calculated using the Euclidean distance metric given by

$$Eulidean\ distance\ = \sqrt{\sum_\theta \left(\mathbf{\mu}_\theta^t - \mathbf{\mu}_\theta^b \right)^2} \tag{4.3}$$

where $\boldsymbol{\mu}_\theta^t$ and $\boldsymbol{\mu}_\theta^b$ correspond to mean values of target (at a given orientation) and background DOP in the observed image acquired at sensor view angle θ. Comparing Figure 4.5 and Figure 4.6 (b) it can be seen that multi-view polarimetric imagery leads to improved target-background discriminability and in fact provides performance comparable to using single view image acquired at the unknown ideal sensor view angle θ for any given target orientation. This approach of combining polarimetric information observed at multiple sensor view angles could potentially benefit applications that involve analyzing scenes that include multiple unknown target geometries.

4.5 Material discriminability using simple scene analysis

This research aims to use DIRSIG polarimetric imagery to explore the functional relationship between the fundamental system parameters and the polarimetric properties of a material by examining the discriminability of a target on a uniform background within a simple scene. Therefore the main components of this study include data generation, quantification, and analysis of material discriminability in polarimetric images. This section presents the details of the simple scene analysis by addressing each of these components.

4.5.1 DIRSIG polarimetric data generation

To understand the fundamental source-scene-sensor physics, a simple DIRSIG scene containing the target of interest on a uniform background (grass, asphalt) was used. Firstly, the analysis focuses on demonstrating the relationship between polarization and optical properties of the target materials. Various man made materials (Shell 2005) such

as glossy and matte painted metals (black, green) were used in the simulation for this analysis. Variations in polarization state due to the changes in surface scattering angle are observed by including targets with different surface normal orientations with respect to the sensor. Figure 4.7 shows the nadir view of the tip of target surface normal with respect to the sensor which is located in the East (0° azimuth angle). Zenith angle of the target surface normal, measured with respect to Z axis, is sampled at every 5° interval and azimuth angle of the target surface normal which is calculated relative to the sensor is sampled at 30° azimuth intervals in the clockwise direction.
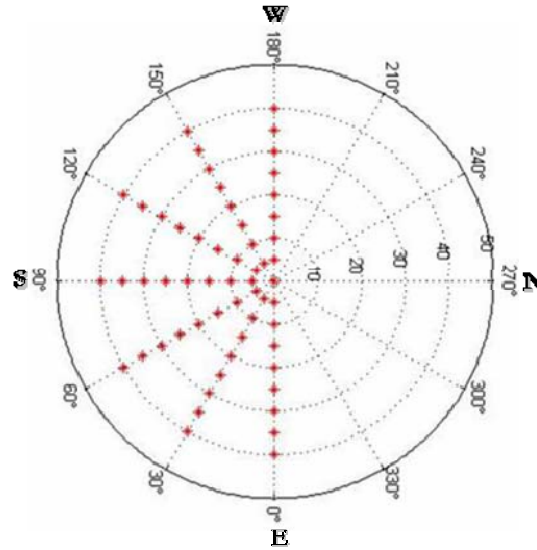
Figure 4.7: Nadir view of tip of target surface normal.

For each case, the analysis was performed to understand the impact of solar location on material discriminability. This analysis was carried out by varying the time of day for acquisition in DIRSIG simulations to observe changes due to solar elevation. The position of sun for every one hour between 5 am to 8 pm for the day used in DIRSIG simulations (07/25/2001, 43° 9' N / 77° 36' W) is shown in Figure 4.8, where the azimuth

angle is marked along the outer circle and the zenith angle is marked along the radial line drawn from the center to the outer circle. We selected 3 different times of day in our simulations until twelve noon (highlighted in blue), due to the observed symmetry in the solar locations after mid day.
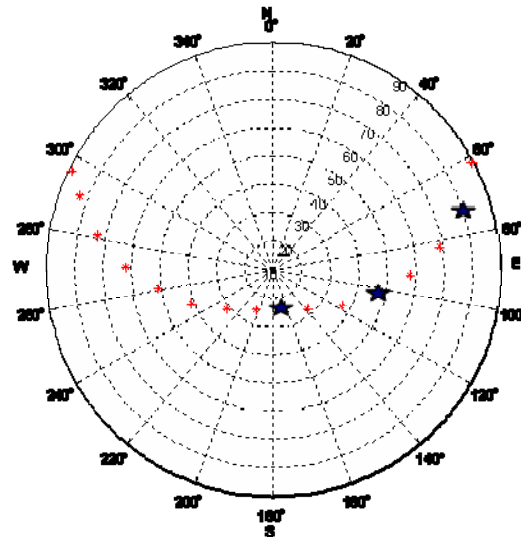
Figure 4.8: Solar locations for 43° 9' N / 77° 36' W on 07/25/2001 between 5am to 8pm.

In all cases, the observations were made at different sensor locations to identify the variability in material discriminability due to changes in the view geometry. The sensor was located at a relative azimuth angle of 180°, 135° and 90° measured with respect to the solar location. Also for each observation azimuth angle, the sensor imaged the scene at 3 different zenith angles (20°, 40° and 60°). Therefore the sensor locations which are relative to the source position will change according to the time of day used in the simulations. Furthermore, the surface orientations with respect to the sensor will also change as shown in Figure 4.9. Such a modification in the DIRSIG Object Database (ODB) file will ensure that the target scattering angles are unaltered for different times of day and therefore the observed polarization is completely due to the change in the

illumination source. Also, in order to understand the impact of the shadowing condition on the material discriminability, the DIRSIG Atmospheric Database (ADB) file was modified to eliminate the solar component in the simulation. Effects of different types of atmosphere such as clear and hazy conditions were also investigated to identify the variability caused by single and multiple scattering in the atmosphere. The effect of upwelled polarization on polarimetric images was studied by including and removing the sensor path radiance in the simulations. In each of these simulations, the observation altitude used was 5000 m and the spatial resolution was 1 m.
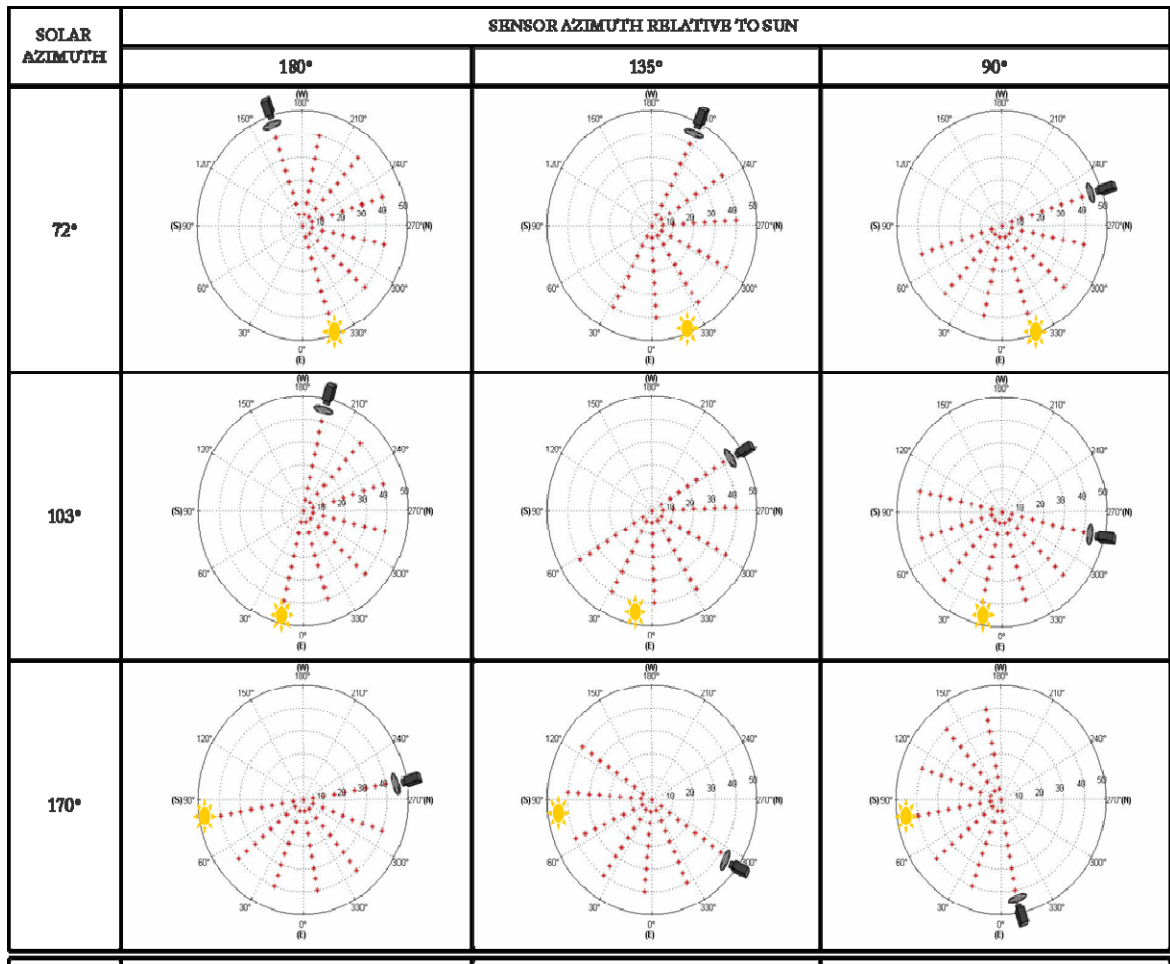
Figure 4.9: DIRSIG sun-sensor geometry for different time of day.

(a)	(b)	(c)

(d)	(e)

(f)
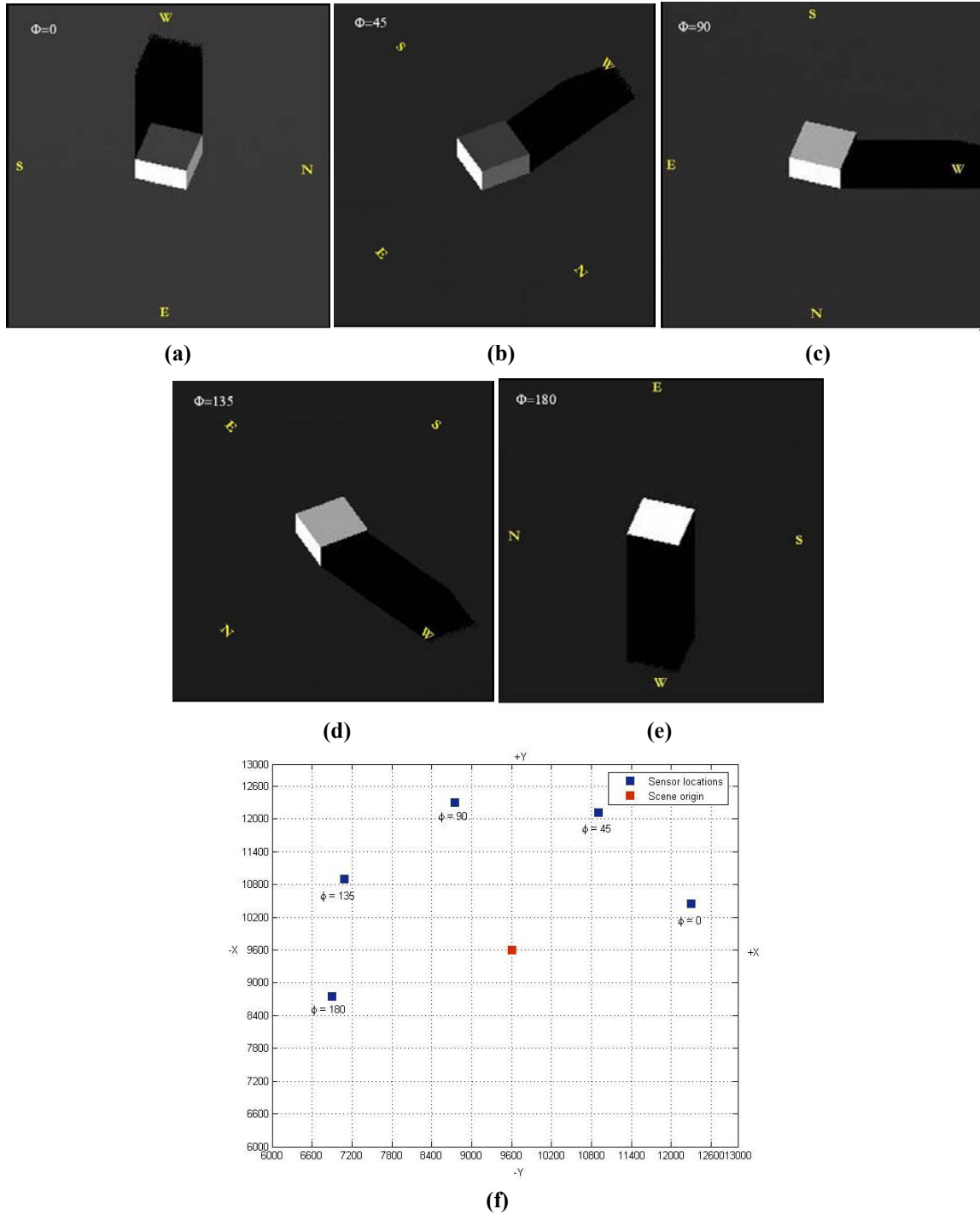
Figure 4.10: Testing DIRSIG sensor locations (a)-(e) images acquired at 6am with varying sensor azimuth locations and (f) projection of sensor locations on ground.

A simple test scene was constructed to verify the correctness of sensor location for making hemispherical observations using DIRSIG. Images were simulated for a given

time of day and sensor elevation but with different sensor azimuth locations. Figure 4.10

(a) - (e) presents images simulated at 6 am with different sensor azimuth locations at $\phi =$

0°, 45°, 90°, 135°, 180°. Source location can be easily identified from the shadow of the

object in the scene. These images were simulated with the sun in the east at lower

elevation angle and therefore the sensor faces the side of the cube that is directly

illuminated by the sun in $\phi = 0°$ image. In the case of $\phi = 180°$ image, the sensor faces

the opposite side of the cube that has no direct solar illumination and therefore looks

darker. In addition, the sensor locations were projected onto the ground as shown in

Figure 4.10 (f) with the scene center at (9600, 9600). It can be seen from Figure 4.10 (f)

that the relative sensor azimuth angle is measured in the anticlockwise direction with

respect to the source.

Table 4.1: List of parameters in simple scene analysis.

PARAMETER	VALUES
Observation time Solar zenith	6, 9, 12 80°, 47°, 23°
Sun-Sensor azimuth	180°, 135°, 90°
Atmosphere	Single and Multiple scattering
Upwelled component	Include, Remove
Observation altitude	5000m
Target-background	[Black glossy, Black matte] on asphalt [Green glossy, Green matte] on grass
Target illumination	Targets in Sun and shadow
Target geometry	Target surface orientations with respect to sensor location
Sensor zenith	20°, 40°, 60°

Table 4.1 provides the summary of parameters used in the polarization phenomenology study to identify the impact of these scene related variables on the observed material discriminability.

4.5.2 Quantification of material discriminability

The main objective of identifying the influence of system parameters on material discriminability in polarimetric images is accomplished by quantifying the material discriminability and then analyzing the measured discriminability at various imaging configurations. In general, statistical classification techniques that exploit dissimilarity in the polarimetric response of the materials can be used to quantify the material discriminability. However, the quantification results will also depend on the statistical framework of the technique. In order to have a 'generalized' quantification of material discriminability, the Euclidean distance metric given in (4.3) was used to measure the polarimetric dissimilarity for each target-background pair within the scene. This distance metric is designed to measure the distinctness of a target from its background, assuming that higher distance values indicate easily detectable targets. Analyzing this direct indicator of discriminability at varying imaging configurations, the optimal phenomenology related parameters to achieve maximum material discriminability can be identified.

This analysis includes multiple imaging configurations as described in Table 4.1 and it can be recognized that for each imaging configuration material discriminability will also depend on the target surface orientation included in the scene. This necessitates the use of descriptive statistics that capture the entire distribution of the measured target

discriminability at any given imaging configuration. This will then allow us to compare two imaging configurations to identify the influence of the scene related parameters on material discriminability. In descriptive statistics, a box plot is a convenient way of graphically depicting groups of numerical data through their five-number summaries: the smallest observation, lower quartile, median, upper quartile, and the largest observation. Figure 4.11 presents the box plot visualization of target discriminability observed at two different imaging configurations, which illustrates the usefulness of box plot in examining the two configurations graphically. Here the location of lower whisker and the median are good indicators that can be used as selection criteria to identify the imaging configuration that maximizes the material discriminability. In Figure 4.11 (c) case A is better than case B in improving target discriminability using polarization information.

(a)   (b)   (c)
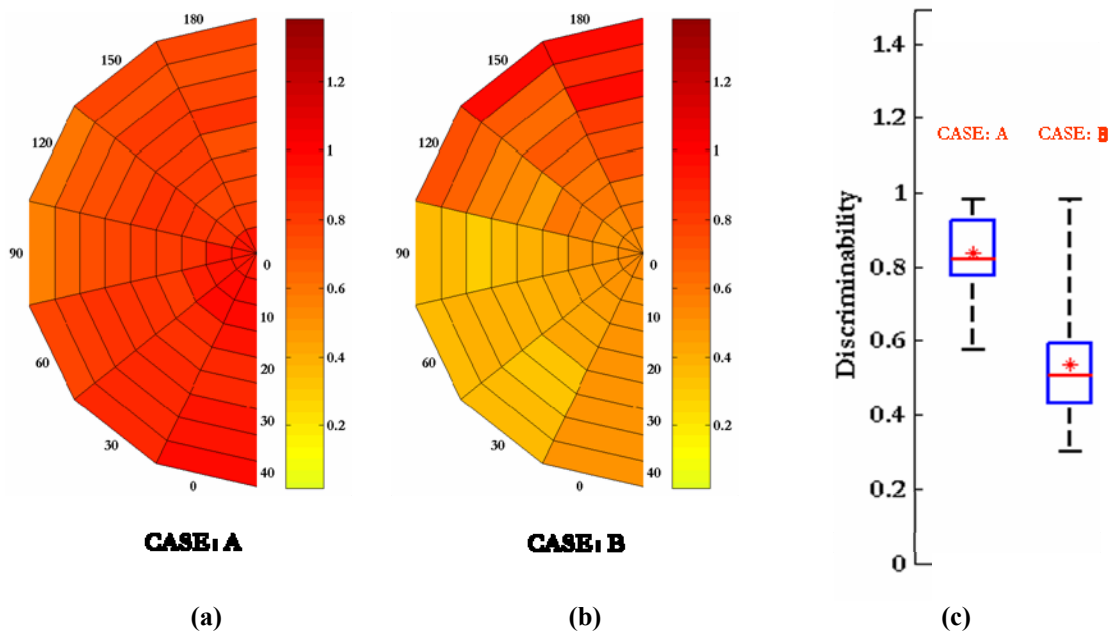
Figure 4.11: Visualization (a)-(b) target-background discriminability for 2 different imaging conditions and (c) Box plot illustration.

4.5.3 Analysis of material discriminability in polarimetric images

The main objective of this analysis is to investigate the impact of polarization phenomenology related parameters on the observed material discriminability using multi view polarimetric images. This section presents the sensitivity analysis of material discriminability in a simple scene for different target background combinations that have poor separability in the visible spectral images.

4.5.3-i Glossy black target on asphalt

A glossy black painted target behaves like a theoretical Fresnel surface reflector. This is because the reflected radiation from a highly absorbing surface is mainly due to single surface reflection while the remaining radiation is completely absorbed. Also, the discriminability of a black target on asphalt is low in the visible spectral region. Figure 4.12 illustrates the observed material discriminability of glossy black target on asphalt when the scene is directly illuminated by sunlight and skylight. It can be seen that in the multiple scattering atmosphere when the upwelled component is not included, the material discriminability is independent of both time of day and sun-sensor azimuth. It can be attributed to the depolarizing effect of the multiple scattering atmosphere, which remains unaffected for different observation geometry and solar location. This can be verified from Table 4.2, which presents the correlation of the measured material discriminability with the material discriminability observed with a theoretical uniform unpolarized sky dome (laboratory illumination condition). The high correlation values indicate the similarity of the multiple scattering atmosphere to unpolarized sky dome and also the slight variation is due to realistic non-uniformity in sky dome.
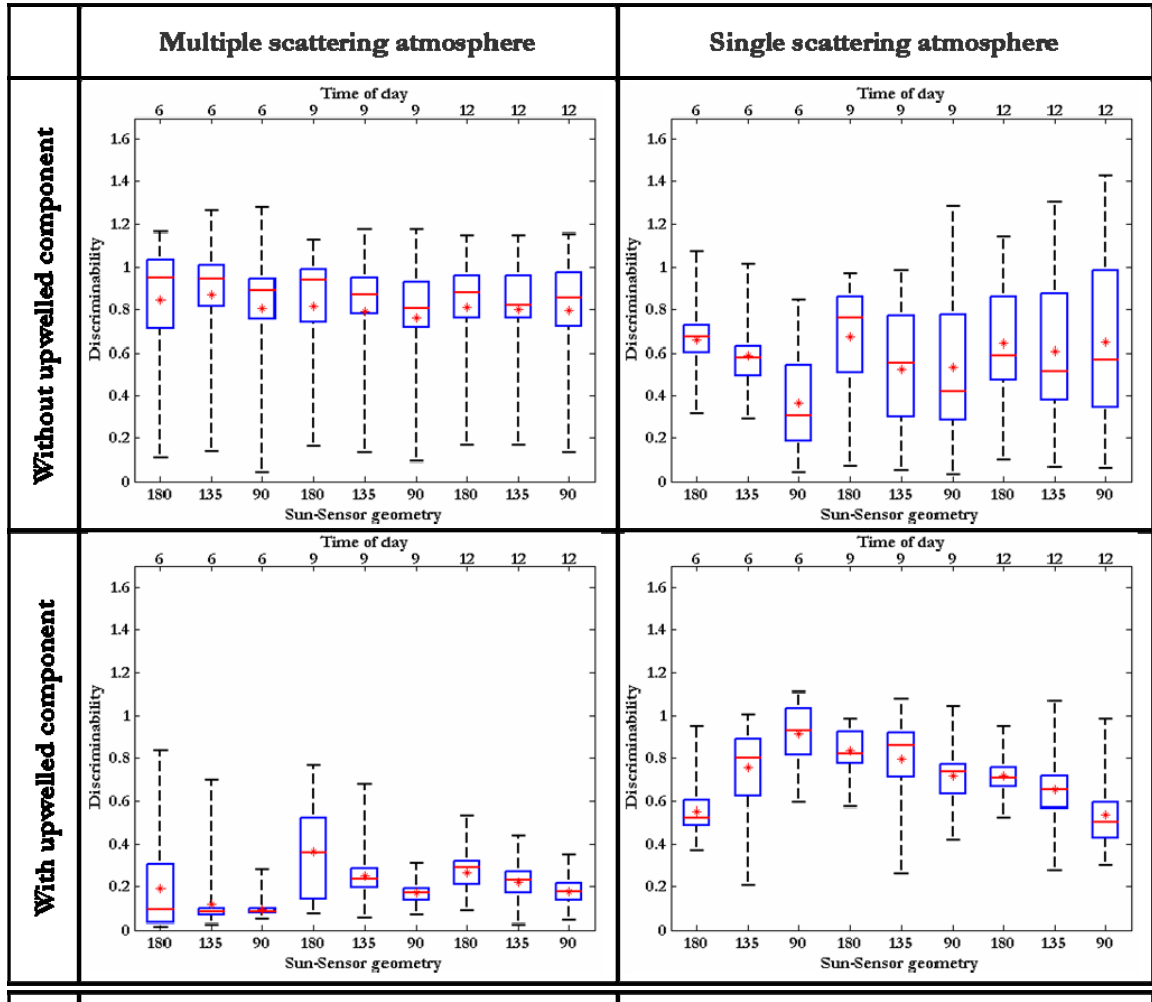
Figure 4.12: Material discriminability of glossy black target on asphalt.

Table 4.2: Correlation with unpolarized sky dome.

Sun-Sensor	180°			135°			90°		
TOD	6	9	12	6	9	12	6	9	12
MS Atmosphere	0.96	0.96	0.95	0.95	0.96	0.95	0.96	0.94	0.95
SS Atmosphere	0.88	0.81	0.79	0.76	0.78	0.78	0.50	0.76	0.82

Therefore the multiple scattering atmosphere extracts target surface polarization information with least effect of the observation geometry. This can be further verified

92

from Figure 4.13, Figure 4.14 and Figure 4.15, which shows the target surface discriminability for different sun-sensor relative azimuth angle using multi view images (MV) and single view image at different sensor observation zenith angles (SV). By comparing with Figure 4.4, it can be seen that the observed target contrast in single view images increases with incident angle experiencing a maximum near the Brewster angle of 56°, as expected, and then decreases beyond the Brewster angle.

Figure 4.13: Material discriminability of glossy black target on asphalt with sensor at 180° in multiple scattering atmosphere.

Figure 4.14: Material discriminability of glossy black target on asphalt with sensor at 135° in multiple scattering atmosphere.

Furthermore, Figure 4.13, Figure 4.14 and Figure 4.15 illustrate the improvement in material discriminability at all target scattering angles using multi view (MV) polarimetric images over the target contrast observed in single view (SV) polarimetric images.

Figure 4.15: Material discriminability of glossy black target on asphalt with sensor at 90° in multiple scattering atmosphere.

It can be seen from Figure 4.12 that in a single scattering atmosphere when the upwelled component is not included, the observed material discriminability of glossy black target on asphalt is dependent on both time of day and sun-sensor azimuth. This can be attributed to the strongly polarizing single scattering atmosphere, which varies for observation geometry and solar location. This can be further verified from Table 4.2,

which presents the correlation of the measured material discriminability for a single scattering atmosphere with the material discriminability observed with a theoretical uniform unpolarized sky dome (laboratory illumination condition). The low correlation values indicate the dissimilarity of the single scattering atmosphere to unpolarized sky dome. As expected there is a significant drop in the correlation value especially for sun-sensor relative azimuth of 90° at 6 am, due to the strongly polarized sky dome.

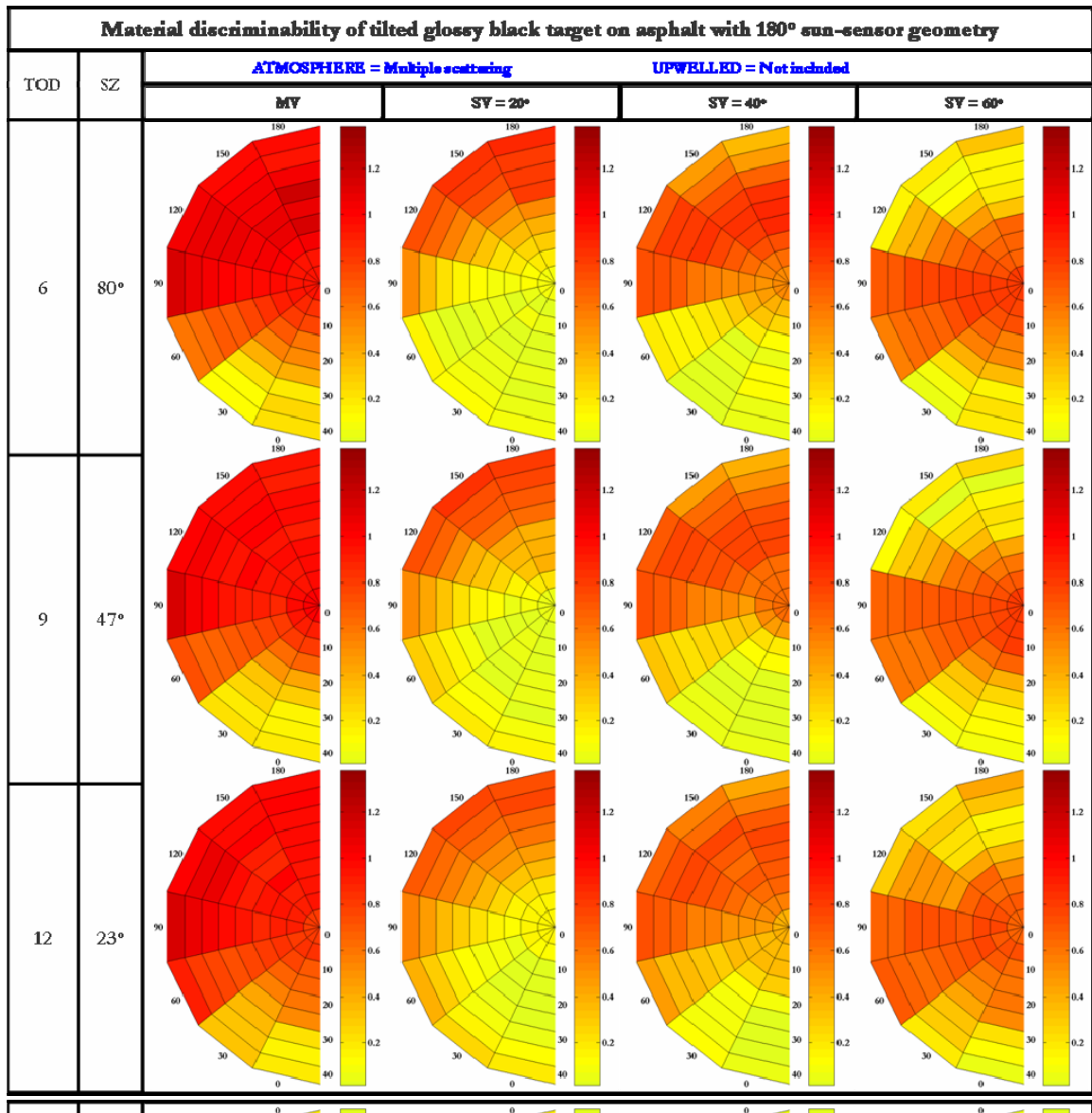

Figure 4.16: Material discriminability of glossy black target on asphalt with sensor at 180° in single scattering atmosphere.

Figure 4.17: Material discriminability of glossy black target on asphalt with sensor at 135° in single scattering atmosphere.

Moreover, as shown in Figure 4.12 the median of observed material discriminability for multiple scattering atmosphere is always higher than the single scattering atmosphere for all observation geometry at any time of day. But for the 6 am case, the lower whisker of material discriminability for single scattering atmosphere is slightly higher than that of the multiple scattering atmosphere when the sensor is located

97

at 180° or 135° with respect to Sun. Also, Figure 4.16, Figure 4.17 and Figure 4.18 illustrate the usefulness of multi view (MV) polarimetric images in maximizing the discriminability when compared to the single view (SV) polarimetric images that are significantly influenced by the polarizing sky dome.
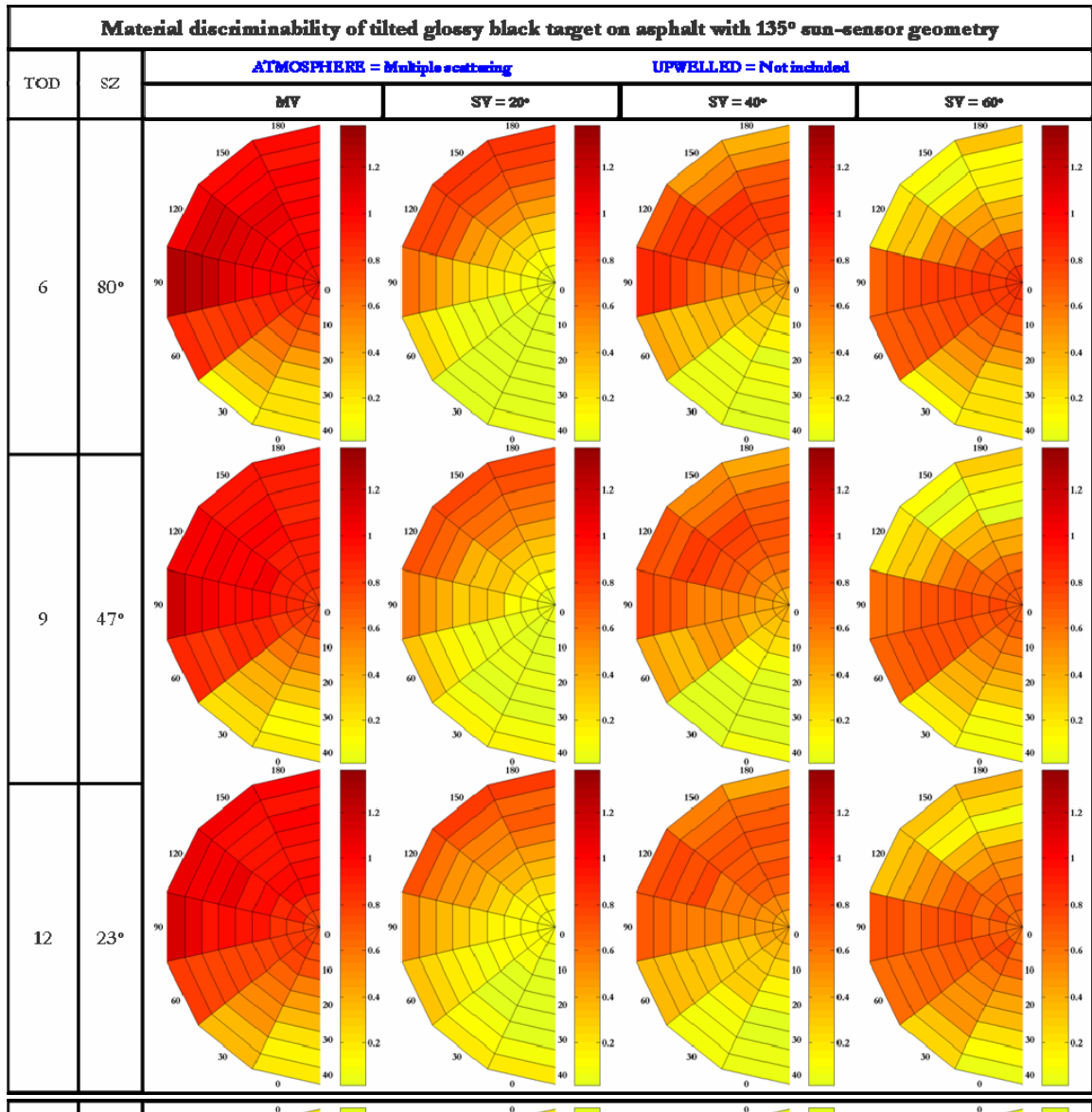

Figure 4.18: Material discriminability of glossy black target on asphalt with sensor at 90° in single scattering atmosphere.

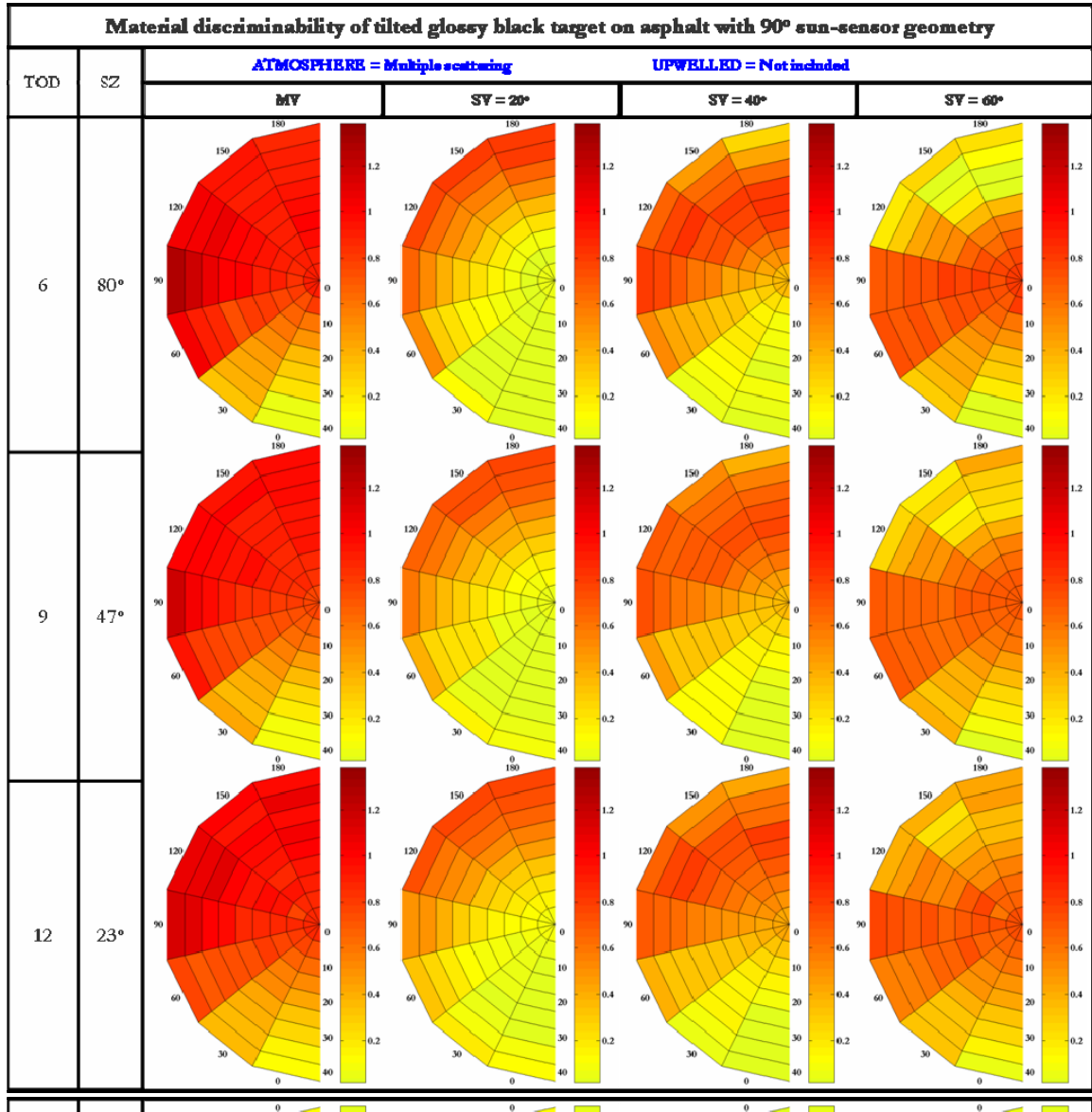**Figure 4.19: Material discriminability of glossy black target on asphalt with sensor at 180° in multiple scattering atmosphere when upwelled is included.**

The impact of including the upwelled component on the discriminability of glossy black target on asphalt when the scene is directly illuminated by sunlight and skylight can be seen in Figure 4.12. In the case of multiple scattering atmosphere, the target discriminability is severely affected as the upwelled component has a depolarizing effect on the target polarization. This can be further confirmed from Figure 4.19, Figure 4.20

99

and Figure 4.21, where the target discriminability is below 0.2 for most of the target orientations. Therefore polarimetric images that include the upwelled component in a multiple scattering atmosphere will contain more information about the atmosphere than the target polarization information.
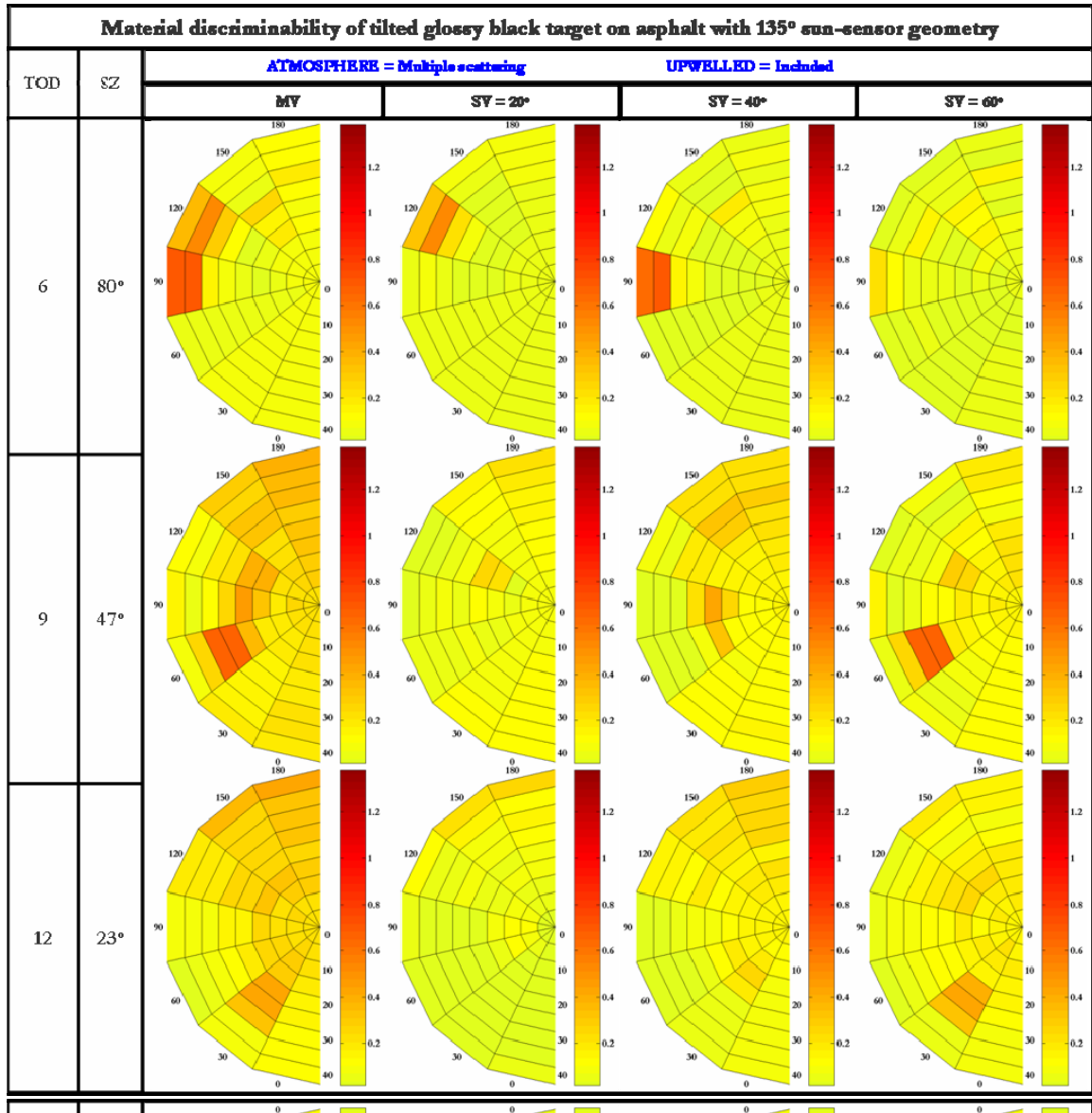
Figure 4.20: Material discriminability of glossy black target on asphalt with sensor at 135° in multiple scattering atmosphere when upwelled is included.
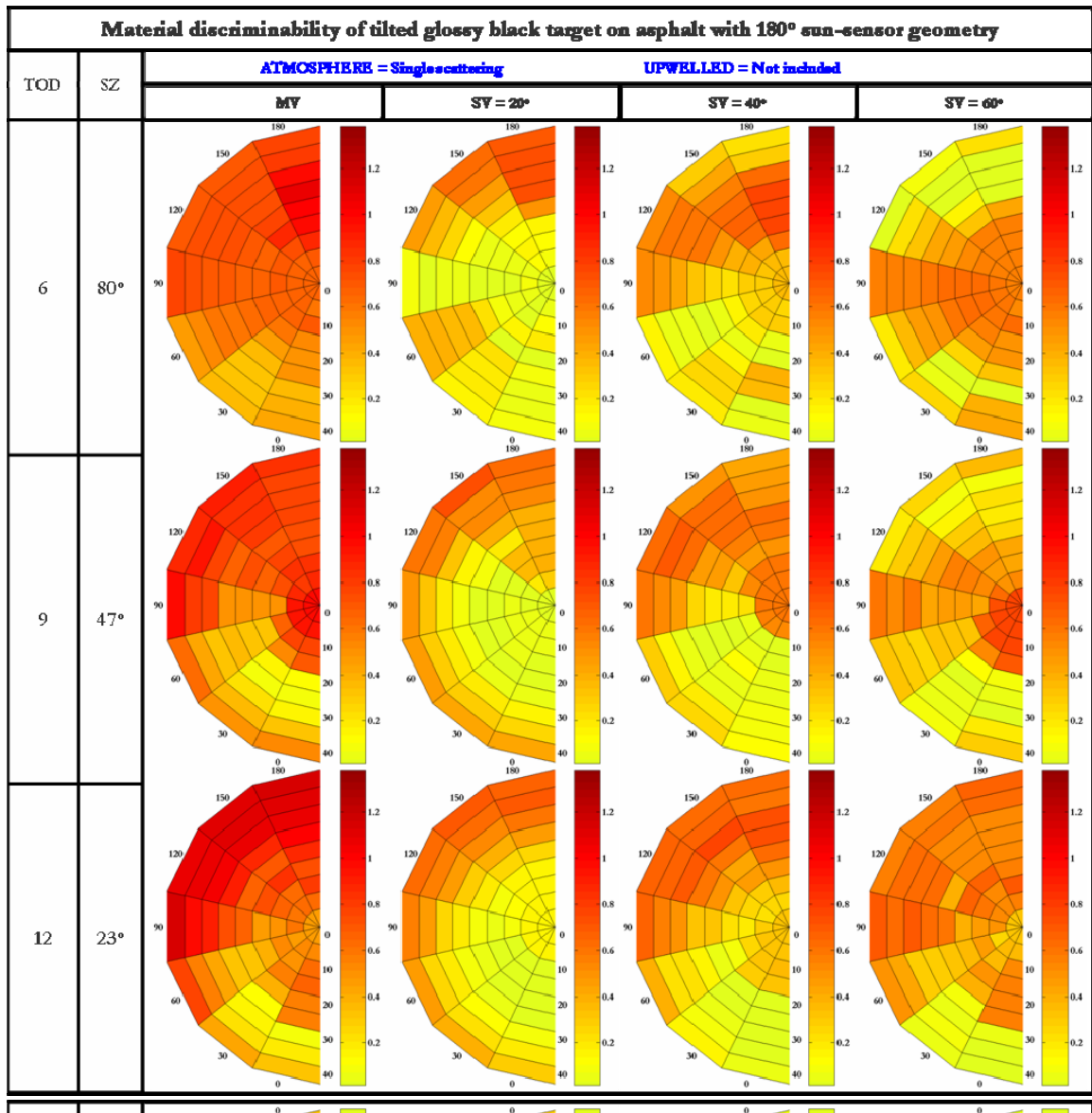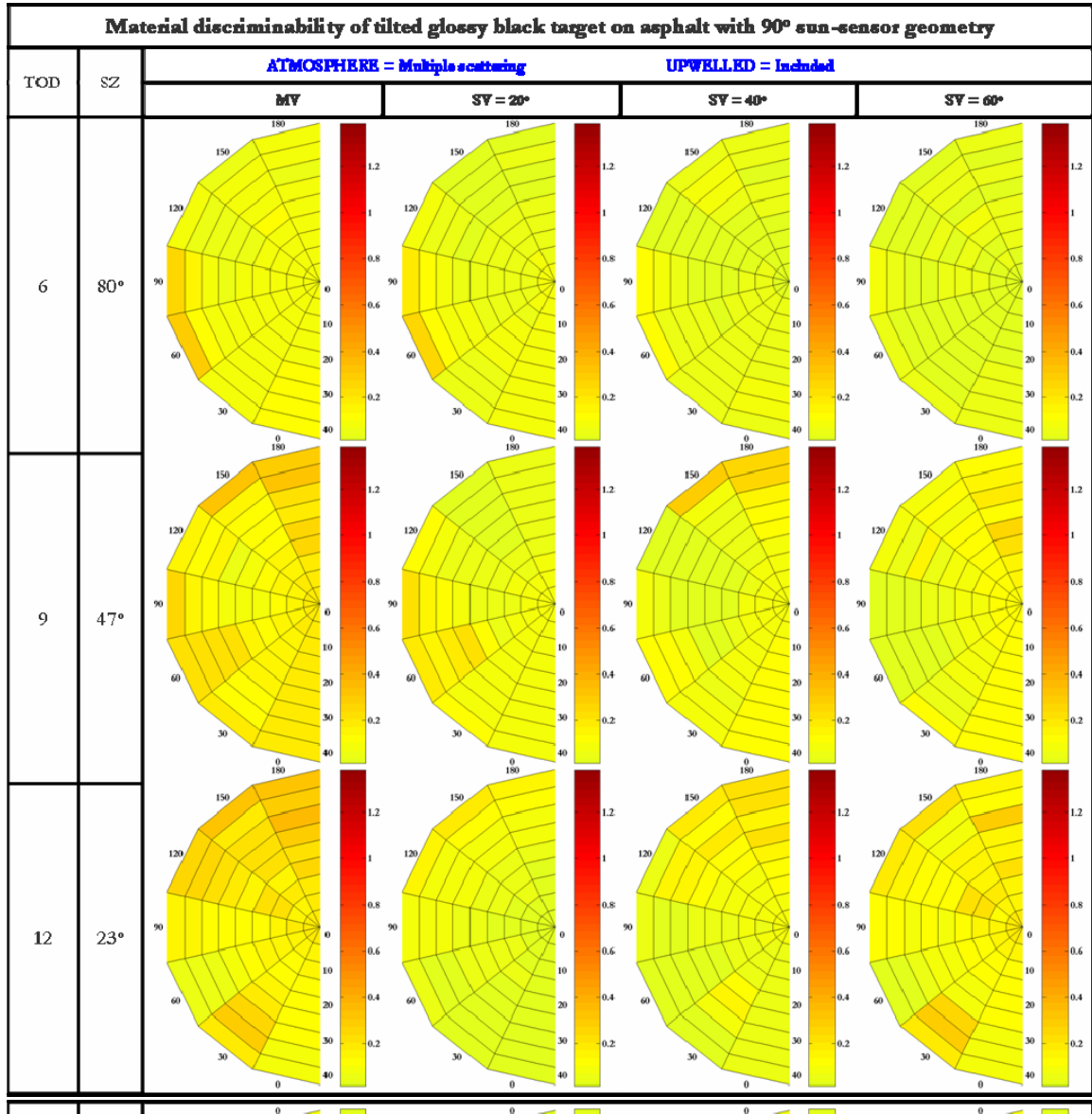
Figure 4.21: Material discriminability of glossy black target on asphalt with sensor at 90° in multiple scattering atmosphere when upwelled is included.

In case of a single scattering atmosphere, the discriminability of glossy black target on asphalt is improved when the upwelled component is included as shown in Figure 4.12. This impact of including the polarizing upwelled component can also be seen in Figure 4.22, Figure 4.23, and Figure 4.24. It is important to recognize that the target contrast in single view images is not a function of target scattering angles.
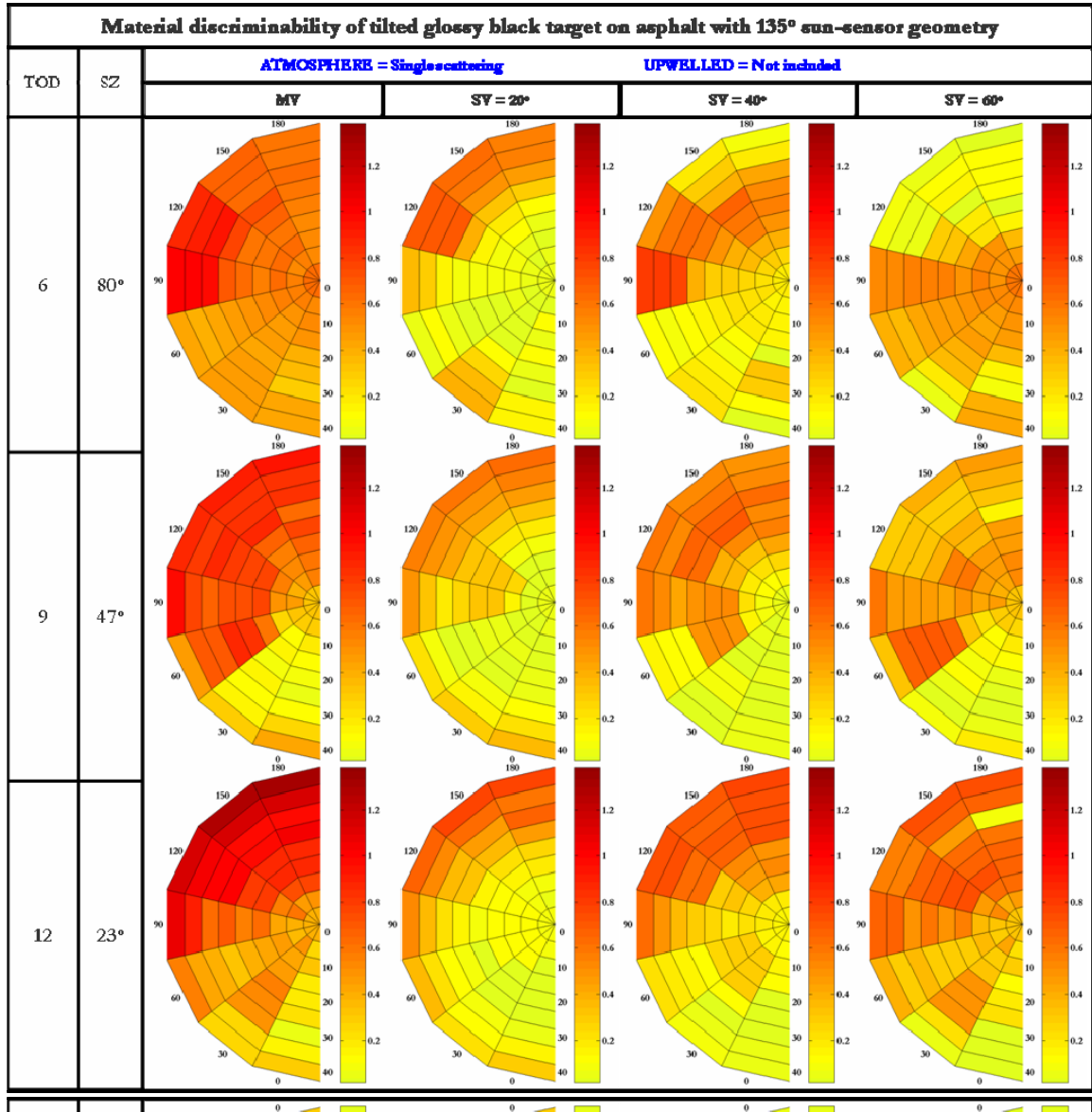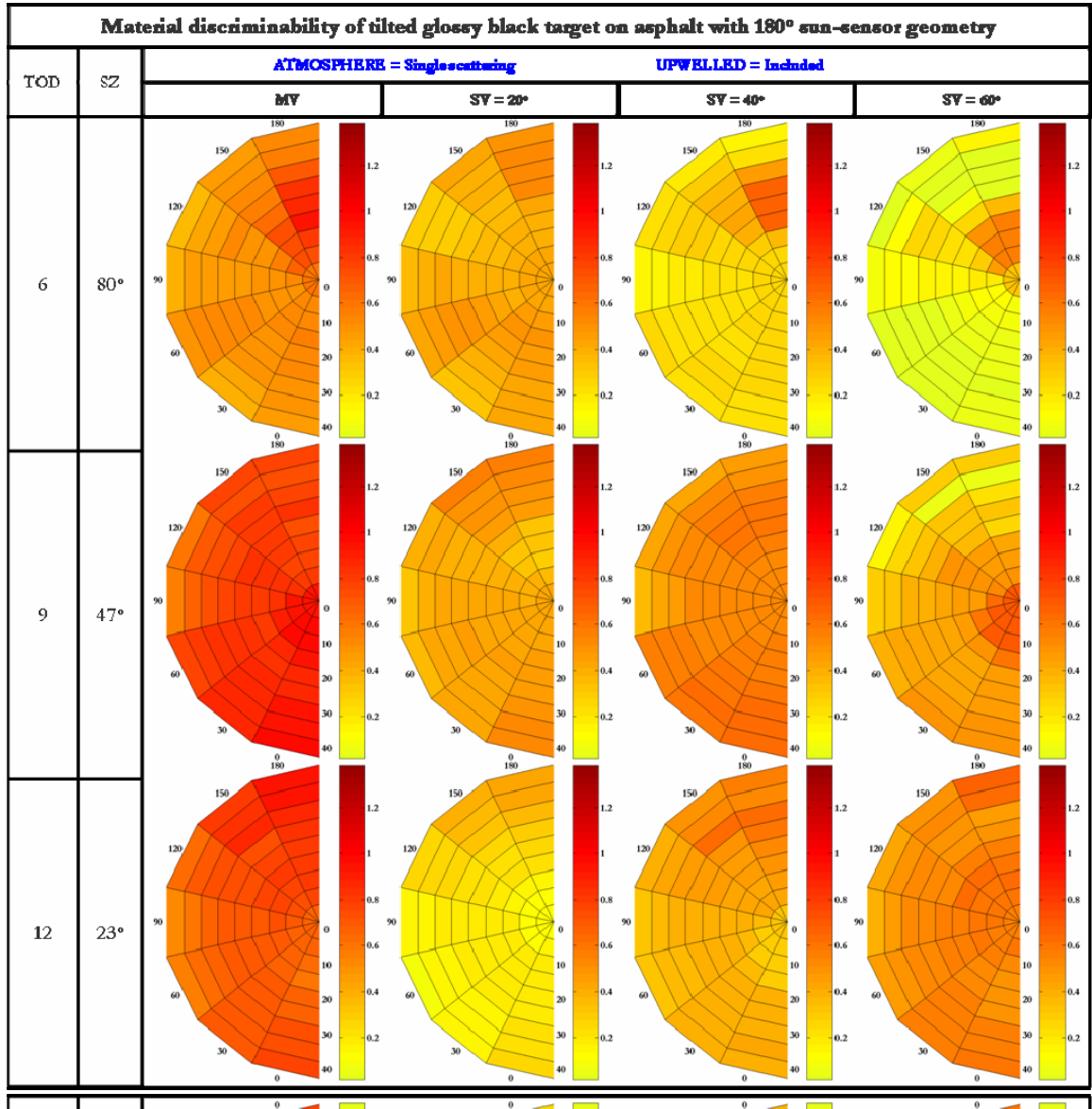
Figure 4.22: Material discriminability of glossy black target on asphalt with sensor at 180° in single scattering atmosphere when upwelled is included.

The total sensor reaching radiance may be approximated as a sum of radiance sources: solar radiation (L_r), skylight component (L_d) and upwelled atmosphere (L_u)

$$L_s = L_r + L_d + L_u .$$ (4.4)

Therefore the Stokes vector representation of the sensor reaching polarized radiance is

102

$$L_{S_0} = L_{S_{0rd}} + L_{S_{0u}}$$
$$L_{S_1} = L_{S_{1rd}} + L_{S_{1u}} \quad (4.5)$$
$$L_{S_2} = L_{S_{2rd}} + L_{S_{2u}}$$

where $L_{S_{xrd}}$ is the Stokes vector of the reflected component that is illuminated by sunlight

and skylight in natural environment.

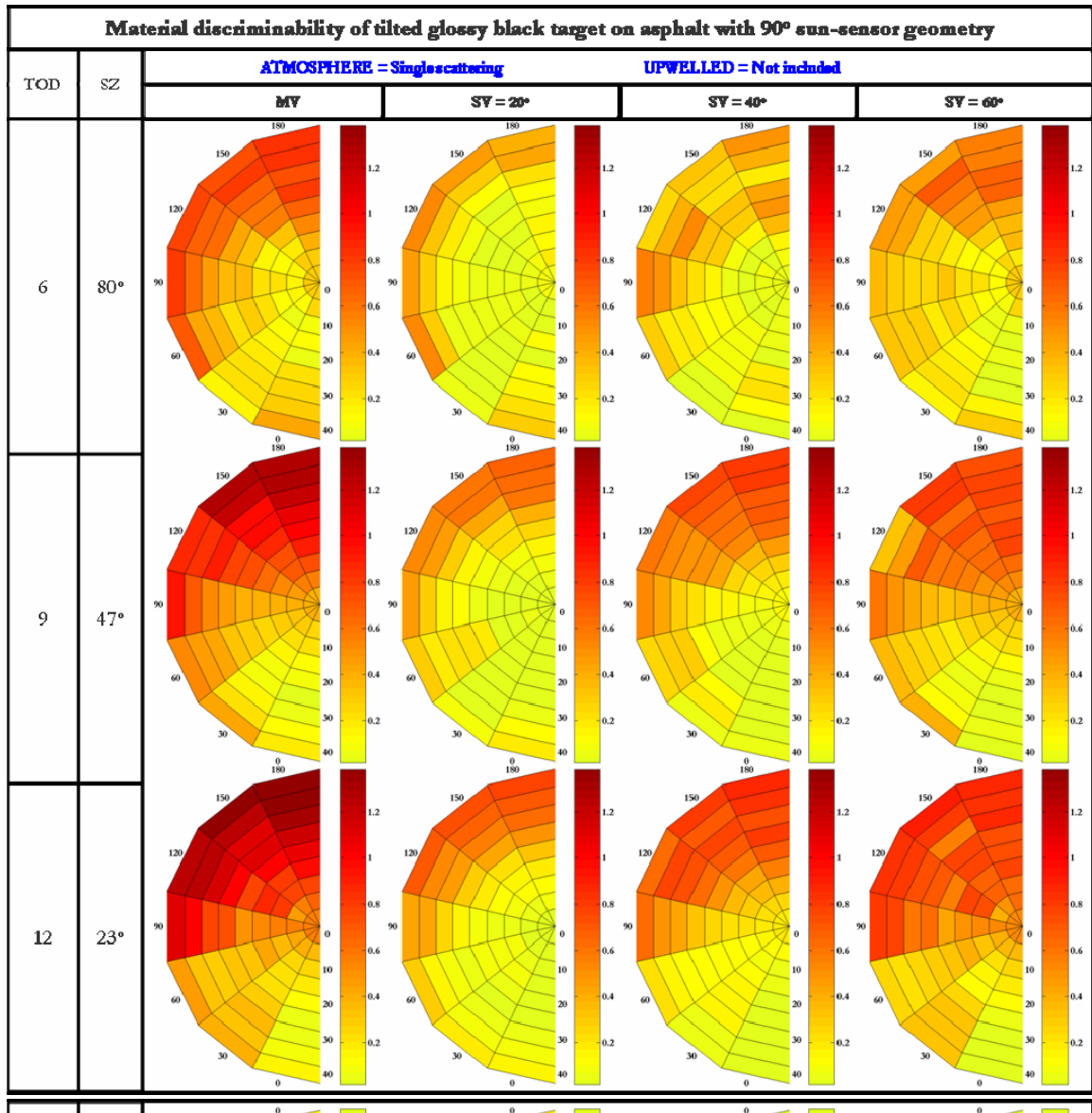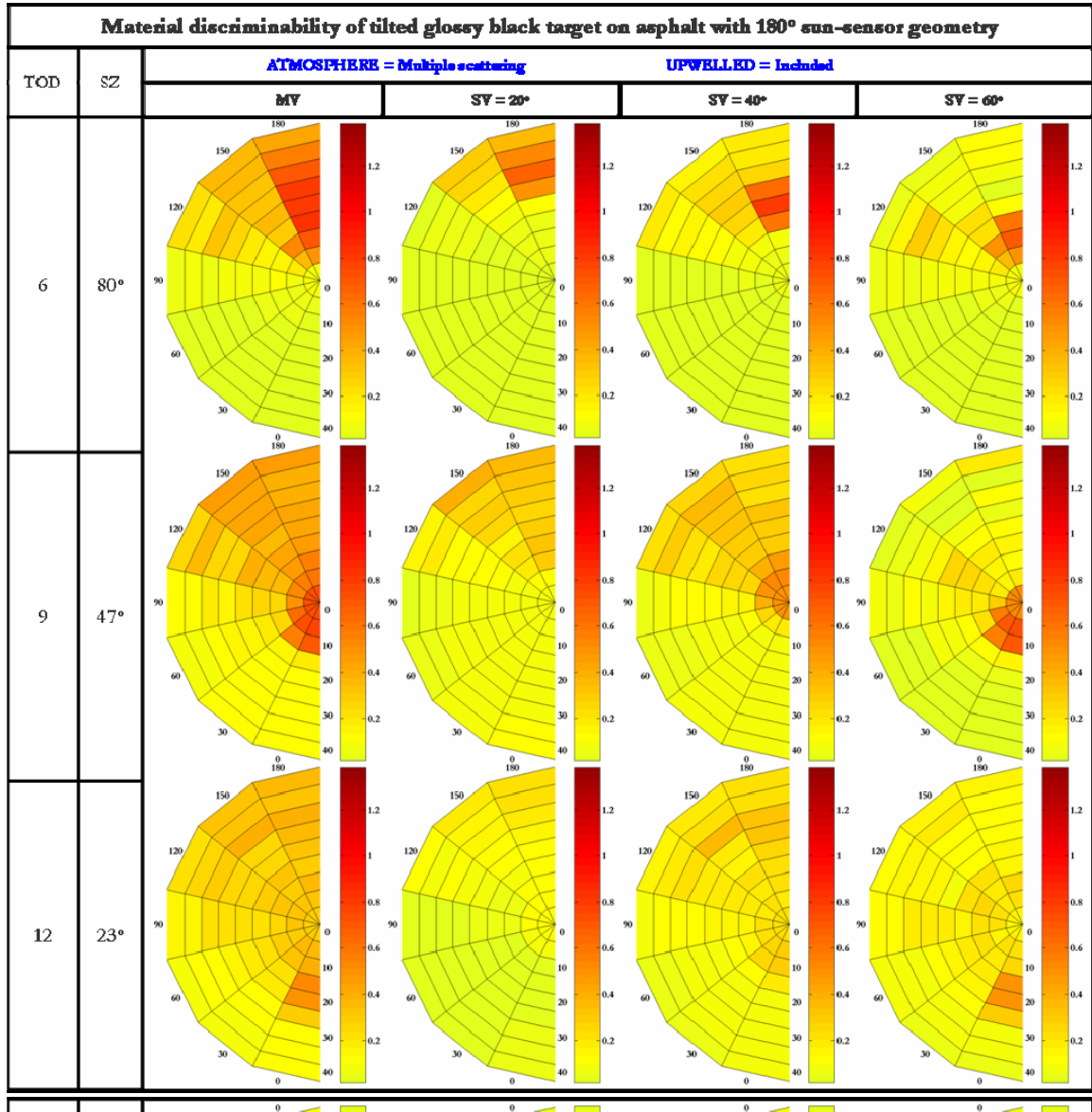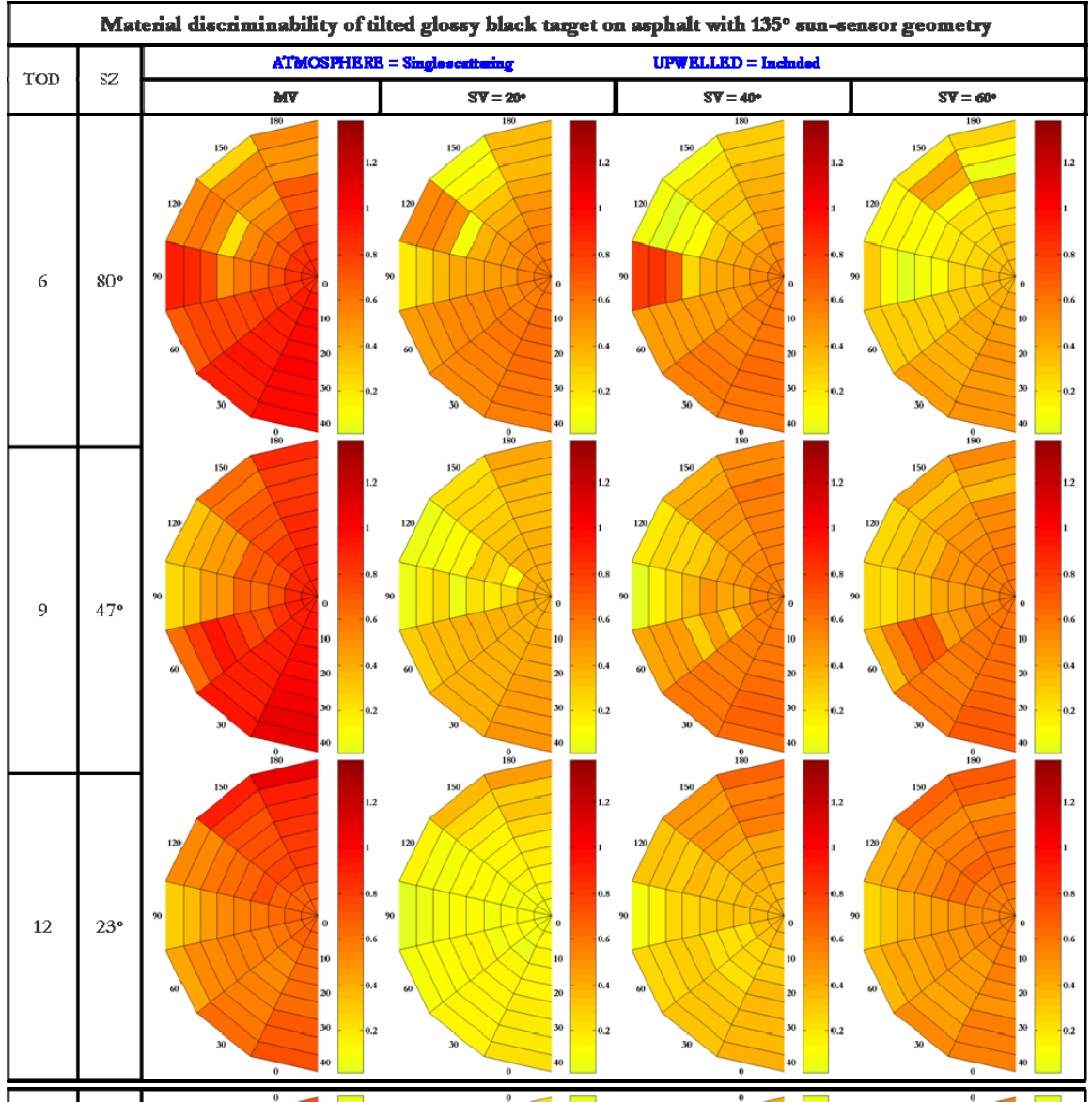**Figure 4.23: Material discriminability of glossy black target on asphalt with sensor at 135° in single scattering atmosphere when upwelled is included.**
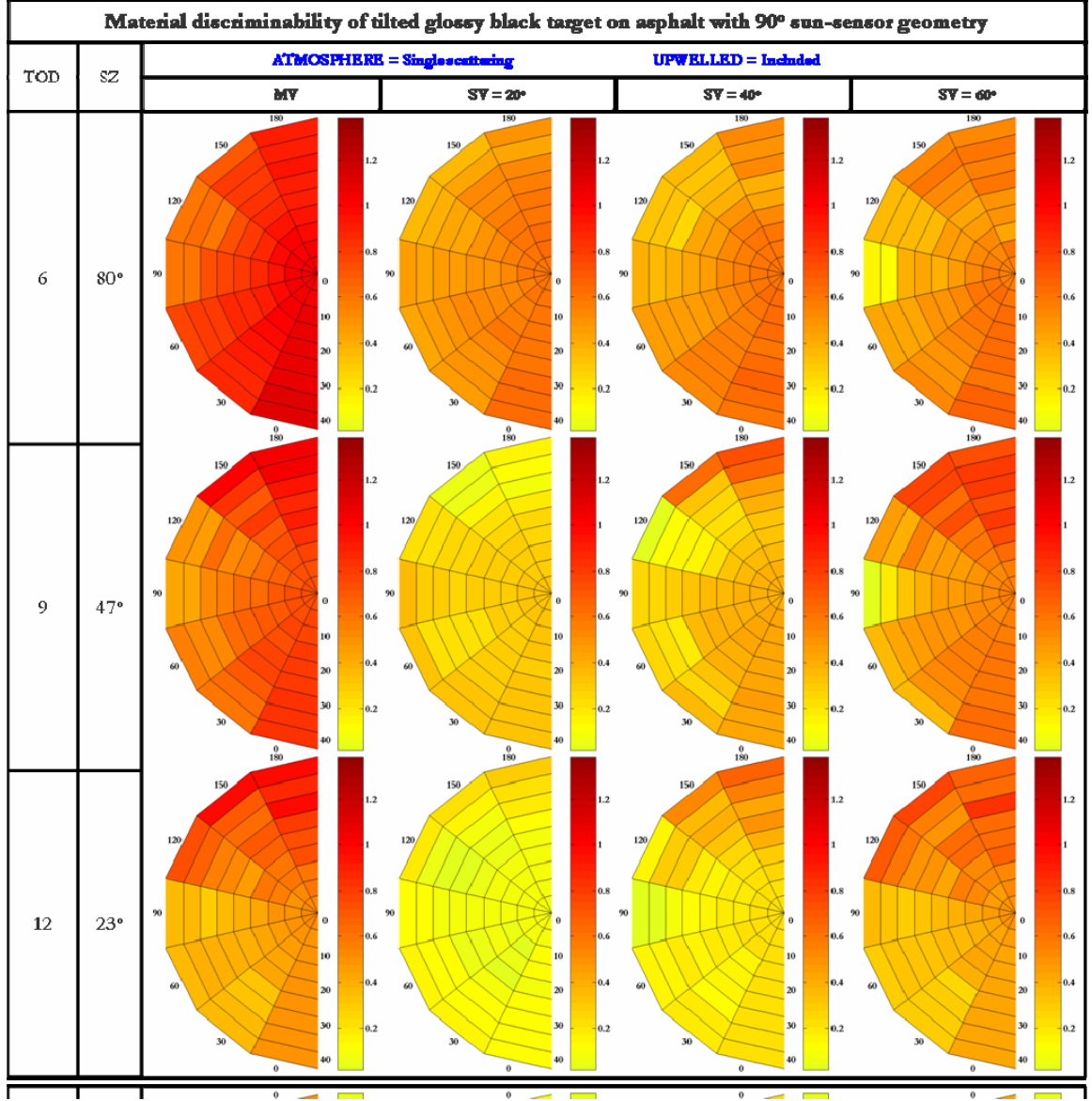
Figure 4.24: Material discriminability of glossy black target on asphalt with sensor at 90° in single scattering atmosphere when upwelled is included.

When the upwelled component is not included, the DOP of target and background can be

written as

$$DOP^{tgt} = \sqrt{\frac{\left(L_{S_{1rd}}^{tgt}\right)^2 + \left(L_{S_{2rd}}^{tgt}\right)^2}{\left(L_{S_{0rd}}^{tgt}\right)^2}} \qquad DOP^{bgd} = \sqrt{\frac{\left(L_{S_{1rd}}^{bgd}\right)^2 + \left(L_{S_{2rd}}^{bgd}\right)^2}{\left(L_{S_{0rd}}^{bgd}\right)^2}} \quad . \qquad (4.6)$$

104

As natural background materials are usually unpolarizing, the target contrast can be approximated as

$$Contrast^{no-upwelled} = \left| DOP^{tgt} - DOP^{bgd} \right| \approx \sqrt{\frac{\left(L_{S_{1rd}}^{tgt}\right)^2 + \left(L_{S_{2rd}}^{tgt}\right)^2}{\left(L_{S_{0rd}}^{tgt}\right)^2}} \, . \qquad (4.7)$$

Due to the polarized upwelled component in the image, background materials in the scene look falsely polarizing and the DOP of background is given by

$$DOP^{bgd} = \sqrt{\frac{\left(L_{S_{1rd}}^{bgd} + L_{S_{1u}}\right)^2 + \left(L_{S_{2rd}}^{bgd} + L_{S_{2u}}\right)^2}{\left(L_{S_{0rd}}^{bgd} + L_{S_{0u}}\right)^2}} \approx \sqrt{\frac{\left(\left(L_{S_{1u}}\right)^2 + \left(L_{S_{2u}}\right)^2\right)}{\left(L_{S_{0rd}}^{bgd} + L_{S_{0u}}\right)^2}} \, . \qquad (4.8)$$

However, the target polarization very much depends on the target geometry and the degree and direction of polarization of the upwelled component. Therefore, the target DOP can increase if the multiplicative term in the numerator in equation (4.9) becomes positive.

$$DOP^{tgt} = \sqrt{\frac{\left(\left(L_{S_{1rd}}^{tgt}\right)^2 + \left(L_{S_{2rd}}^{tgt}\right)^2\right) + \left(\left(L_{S_{1u}}\right)^2 + \left(L_{S_{2u}}\right)^2\right) + 2\left(L_{S_{1rd}}^{tgt} L_{S_{1u}} + L_{S_{2rd}}^{tgt} L_{S_{2u}}\right)}{\left(L_{S_{0rd}}^{tgt} + L_{S_{0u}}\right)^2}} \, . \qquad (4.9)$$

This phenomenon can be easily identified in the single view (SV) target contrast images shown in Figure 4.22, Figure 4.23, and Figure 4.24.

Figure 4.25 illustrates the observed material discriminability of glossy black target on asphalt when the scene is in shadow and hence illuminated only by the skylight component. Comparing Figure 4.12 and Figure 4.25 it can be seen that in the multiple scattering atmosphere when the upwelled component is not included, the material discriminability is independent of the illumination source type. When the upwelled

component is included the target discriminability is lowered in shadowed scene for both the atmospheric conditions.
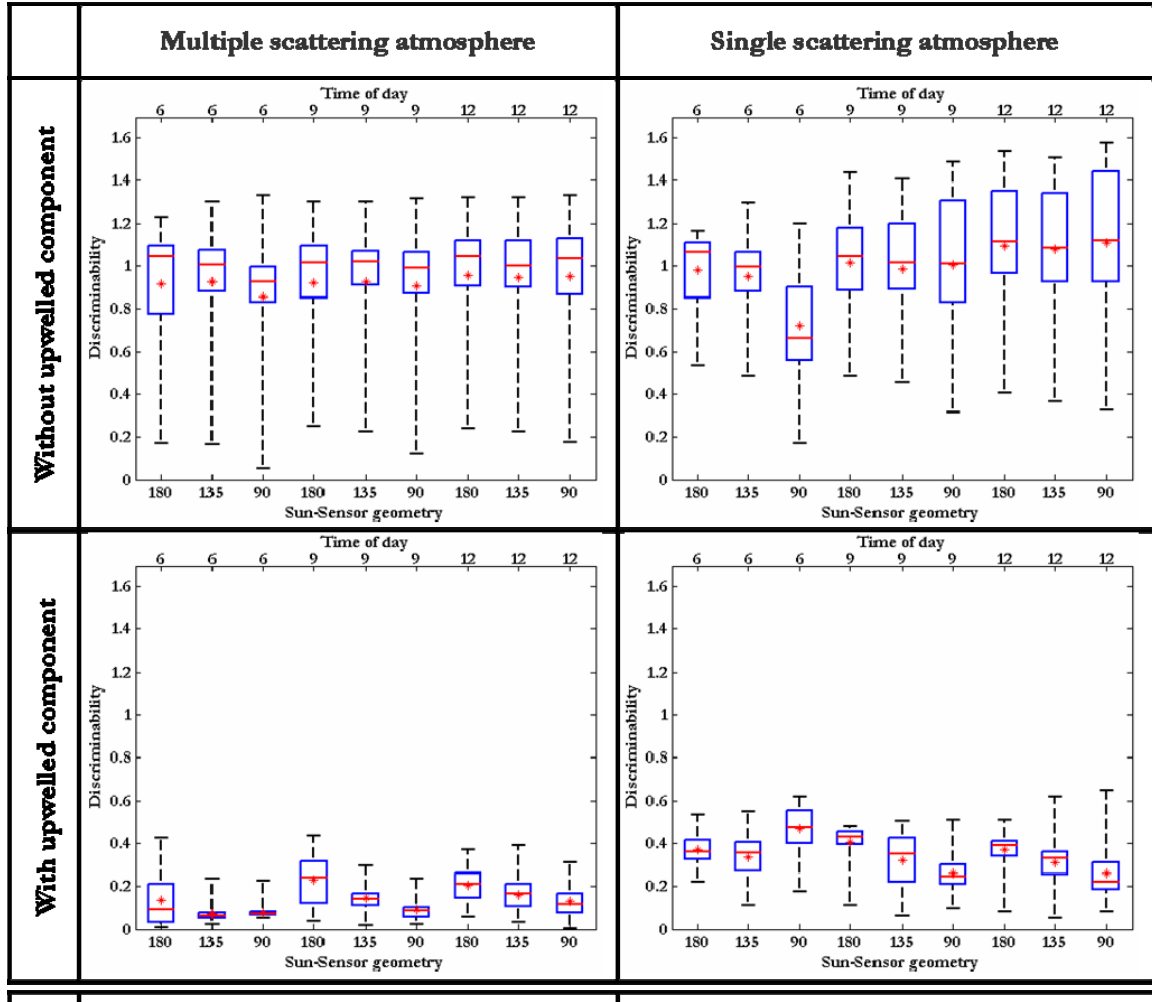
Figure 4.25: Material discriminability of shadowed glossy black target on asphalt.

In the absence the upwelled component equation (4.4) is simplified to $L_s = L_r + L_d$. The Stokes vector representation of the sensor reaching radiance is derived by substituting for the solar and downwelled surface reflection component as

106

$$L_{S_0} = \vec{f}_0 \cdot E_{sun} \cdot \vec{S}_{sun} + \vec{f}_0 \cdot E_{sky} \cdot \vec{S}_{sky}$$
$$L_{S_1} = \vec{f}_1 \cdot E_{sun} \cdot \vec{S}_{sun} + \vec{f}_1 \cdot E_{sky} \cdot \vec{S}_{sky} \; , \qquad (4.10)$$
$$L_{S_2} = \vec{f}_2 \cdot E_{sun} \cdot \vec{S}_{sun} + \vec{f}_2 \cdot E_{sky} \cdot \vec{S}_{sky}$$

where E_{sun} and E_{sky} are the solar and sky dome irradiance incident on the surface respectively and $\vec{f}_x$ corresponds to the row vector of the Mueller matrix.
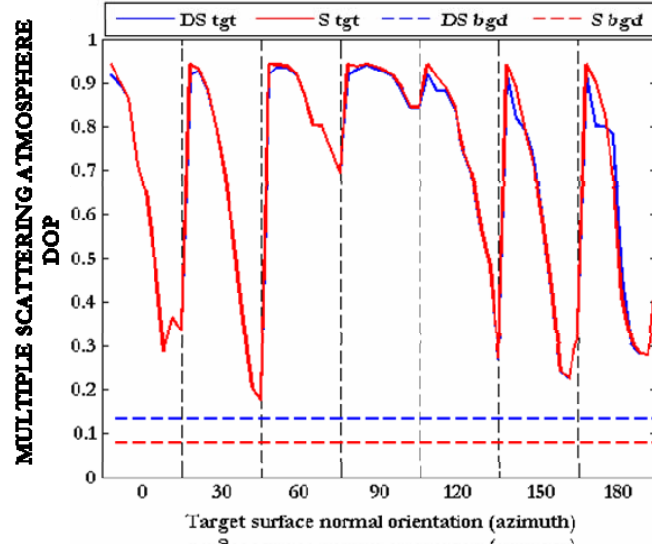
(a)
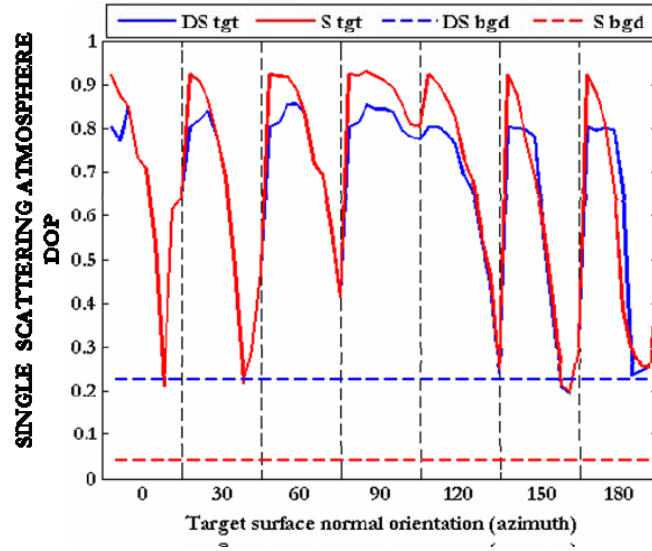
(b)

Figure 4.26: DOP of glossy black target and background in direct sunlight (DS) and in shadow (S) at 9 am (a) multiple scattering atmosphere and (b) single scattering atmosphere.

107

Using equation (4.10) and recalculating the DOP of target in sunlight and in shadow for multiple scattering atmosphere, we can recognize from equation (4.11) that it is independent of illumination and is purely a function of surface polarization properties. This makes the material discriminability independent of illumination type and time of day.

$$DOP^{tgt} = \sqrt{\frac{\left(f_{10} \cdot E_{sun} \cdot S_{sun_0} + f_{10} \cdot E_{sky} \cdot S_{sky_0}\right)^2 + \left(f_{20} \cdot E_{sun} \cdot S_{sun_0} + f_{20} \cdot E_{sky} \cdot S_{sky_0}\right)^2}{\left(f_{00} \cdot E_{sun} \cdot S_{sun_0} + f_{00} \cdot E_{sky} \cdot S_{sky_0}\right)^2}}$$

$$DOP^{tgt} = \sqrt{\frac{\left(f_{10}\right)^2 + \left(f_{20}\right)^2}{\left(f_{00}\right)^2}} = DOP^{tgt\_shad}$$

(4.11)

Figure 4.26 presents the DOP of target with varying surface normal orientations and background, in direct sunlight (DS tgt/bgd) and in shadow (S tgt/bgd) observed at 9 am for different atmospheric conditions. It can be seen from Figure 4.26(a) that the target DOP does not change under varying illumination conditions for a multiple scattering atmosphere, but the background DOP value is slightly lowered in shadow which leads to the slight increase in the material discriminability (median) that is shown in Figure 4.25. However, in the single scattering atmosphere case presented in Figure 4.26(b), the polarized sky dome reduces the DOP of background in shadow resulting in a significant increase in the target discriminability as shown in Figure 4.25.

4.5.3-ii Glossy green target on grass

The reflected radiation from a glossy green painted surface is contributed by both single surface reflection and volumetric scattering component. Unlike the single reflection component, the volumetric scattering component partially depolarizes the

incident polarized radiation due to multiple random reflections. Figure 4.27 illustrates the observed material discriminability of glossy green target on grass when the scene is directly illuminated by sunlight and skylight. Due to the depolarizing volumetric scattering component, glossy green target (Figure 4.27) has lower discriminability compared to glossy black target (Figure 4.12) for all imaging configurations.
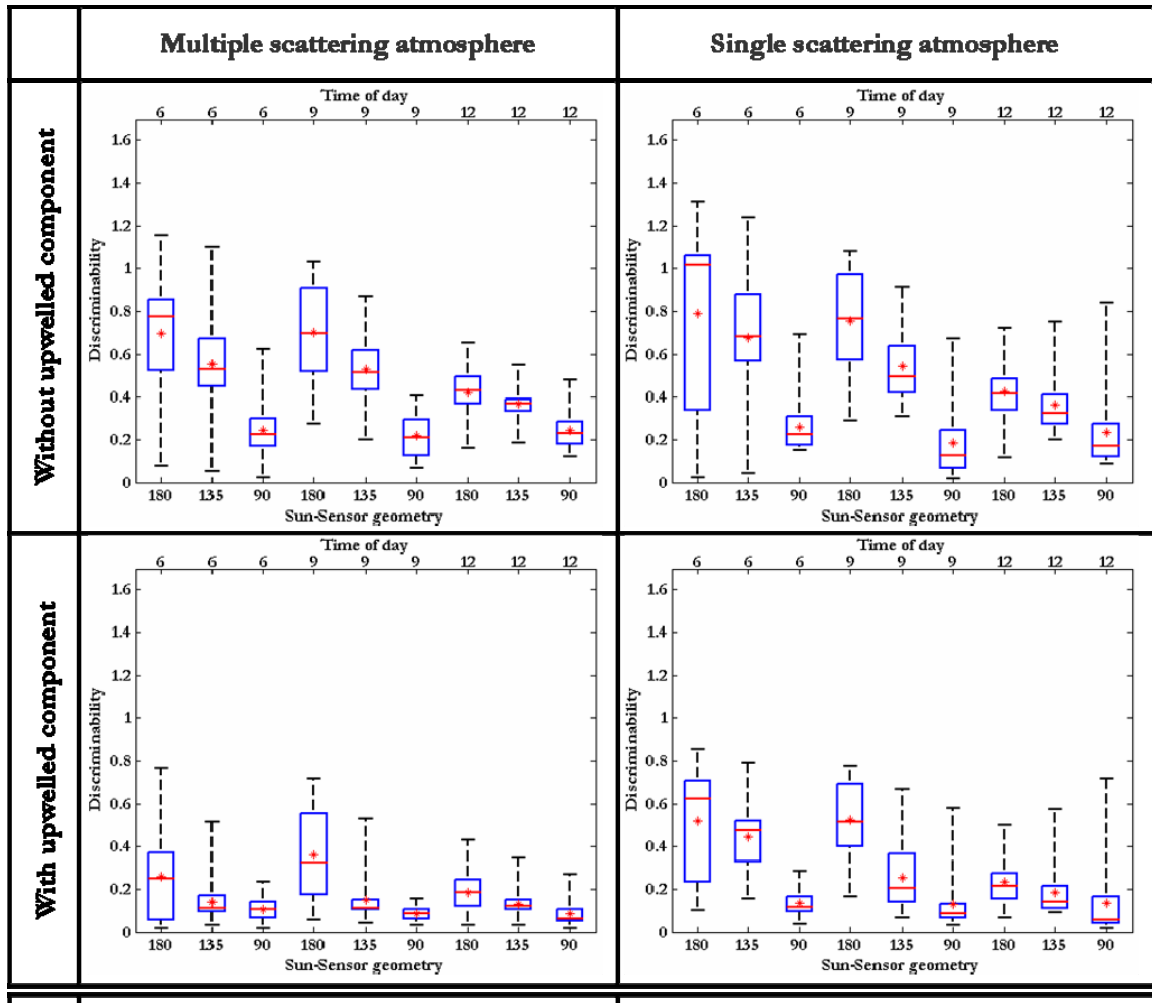
Figure 4.27: Material discriminability of glossy green target on grass.

It can be seen that when the upwelled component is not included, the glossy green target discriminability is independent of atmospheric type but dependent on time of day and sun-sensor azimuth. The material discriminability is worse when the relative sun-

sensor geometry is 90° at all times of day. Furthermore, when the upwelled component is included the target discriminability is lowered for both the atmospheric conditions. Figure 4.28 illustrates the observed material discriminability of glossy green target on grass in shadow. Target discriminability is improved in shadow for the single scattering atmosphere. However, the target discriminability in shadow is further reduced when the upwelled component is included in a multiple scattering atmosphere. It can be recognized that when the upwelled component is not included, the target discriminability in shadow is independent of the observation geometry and solar location.
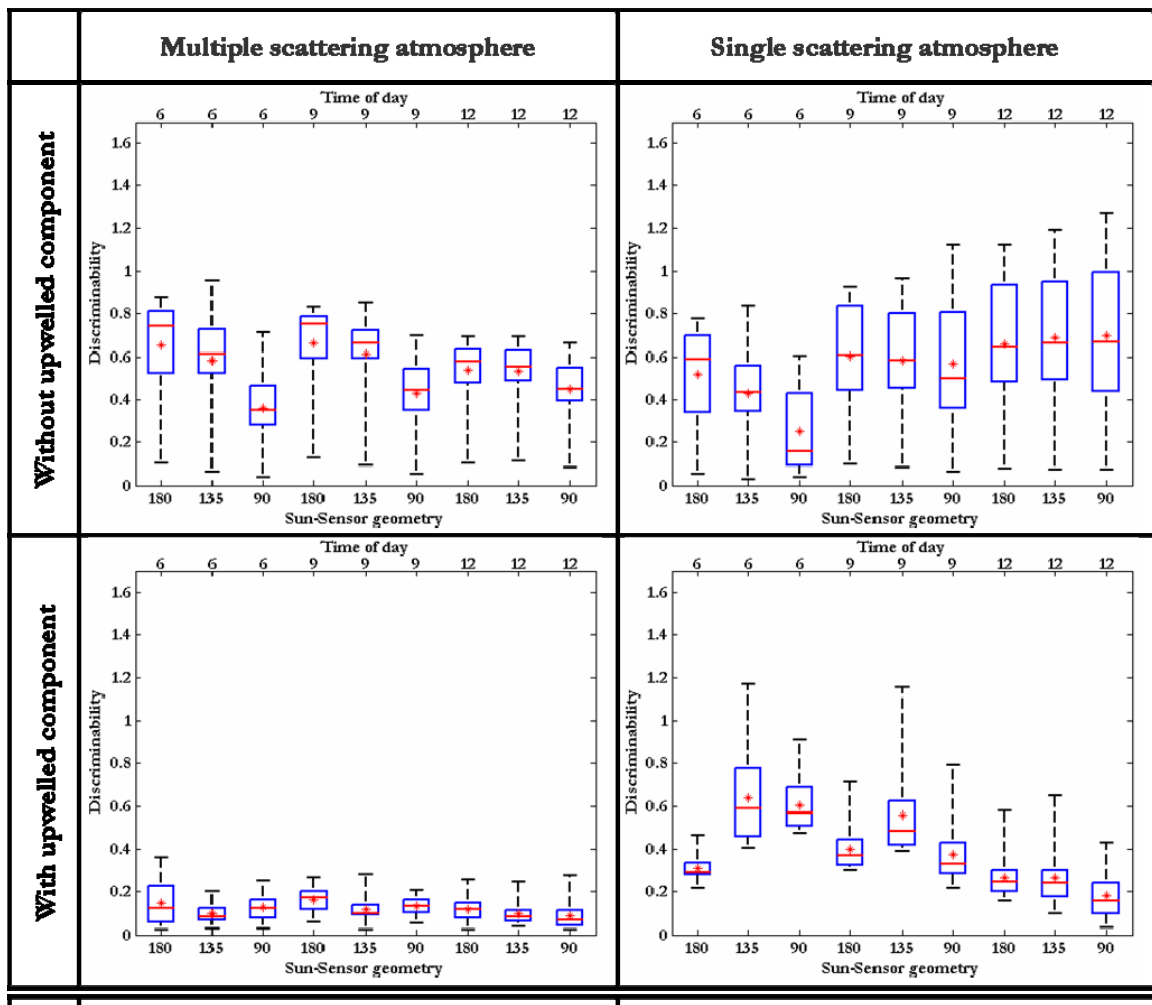
Figure 4.28: Material discriminability of shadowed glossy green target on grass.

110

4.5.3-iii Matte black target on asphalt

Matte surfaces are depolarizing due to the fact that the reflected radiation is dominated by volumetric scattering component. Figure 4.29 presents the observed material discriminability for matte black target on asphalt when the scene is illuminated by sunlight and skylight. The depolarizing volumetric scattering component lowers the target discriminability for all imaging configurations. This can be observed when Figure 4.29 is compared with glossy black target discriminability in Figure 4.12 and glossy green target discriminability Figure 4.27.
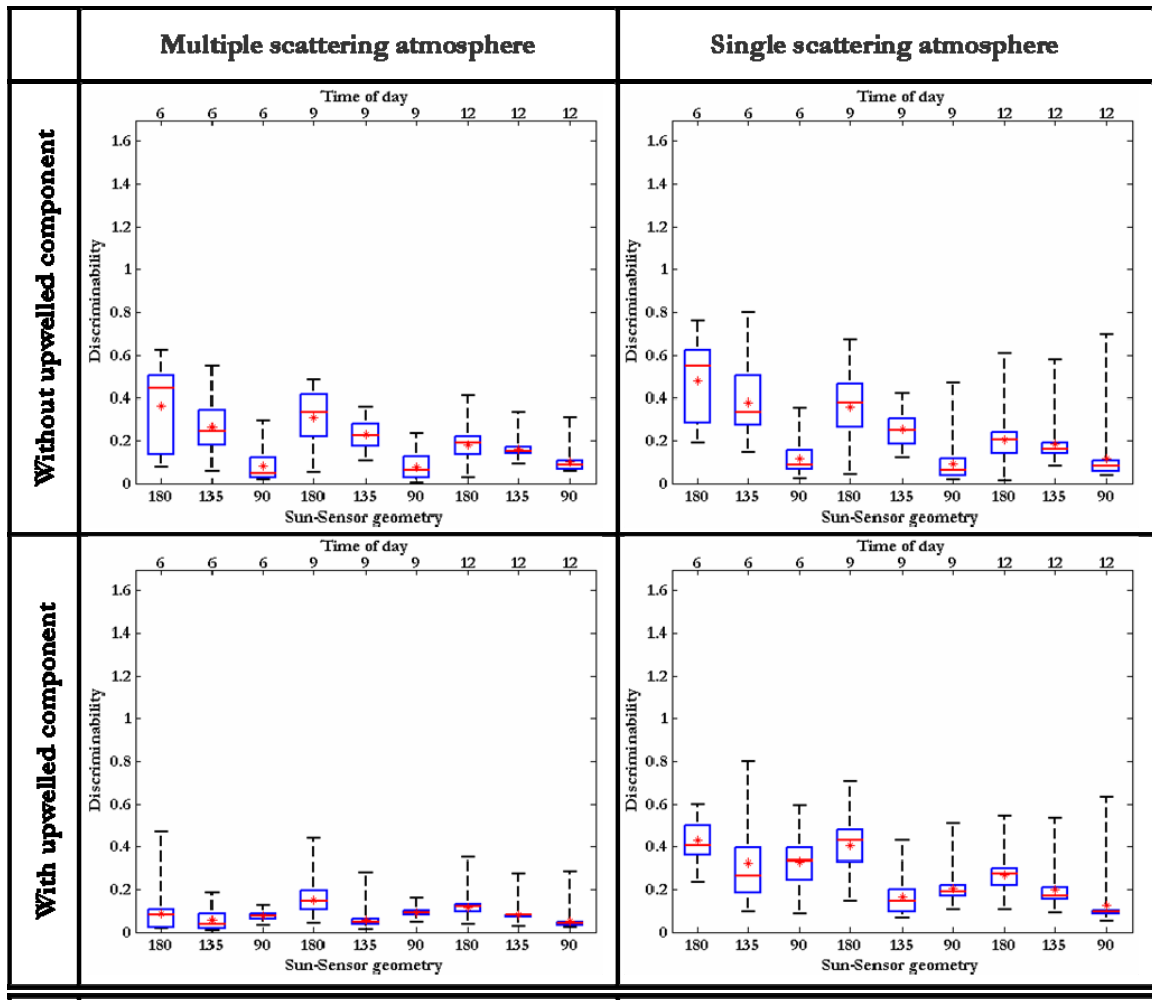
Figure 4.29: Material discriminability of matte black target on asphalt.

111
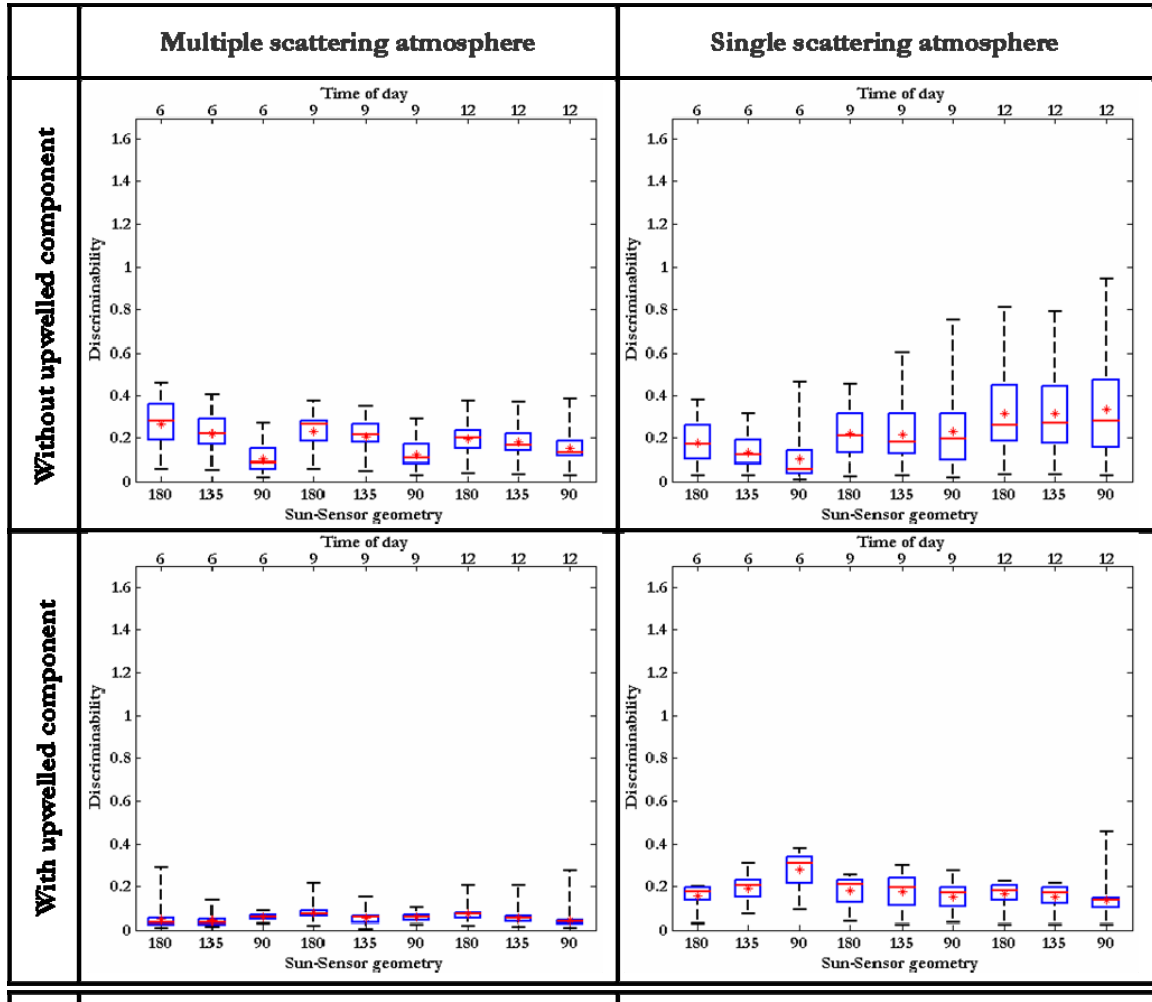
Figure 4.30: Material discriminability of shadowed matte black target on asphalt.

Figure 4.30 illustrates the observed material discriminability for matte black target on asphalt in shadow. It can be identified that the material discriminability is reduced for all the imaging configurations when compared to the sunlit case shown in Figure 4.29. When the upwelled component is not included, the target discriminability in shadow is independent of the observation geometry and solar location. Also, from Figure 4.25 it can be seen that glossy black target has higher discriminability in shadow when compared to matte black target on asphalt shown in Figure 4.30.

112

4.5.3-iv Matte green target on grass

The observed material discriminability for matte green target on grass when illuminated by sunlight and skylight is presented in Figure 4.31. As expected, the depolarizing volumetric scattering component lowers the target discriminability for all imaging configurations.
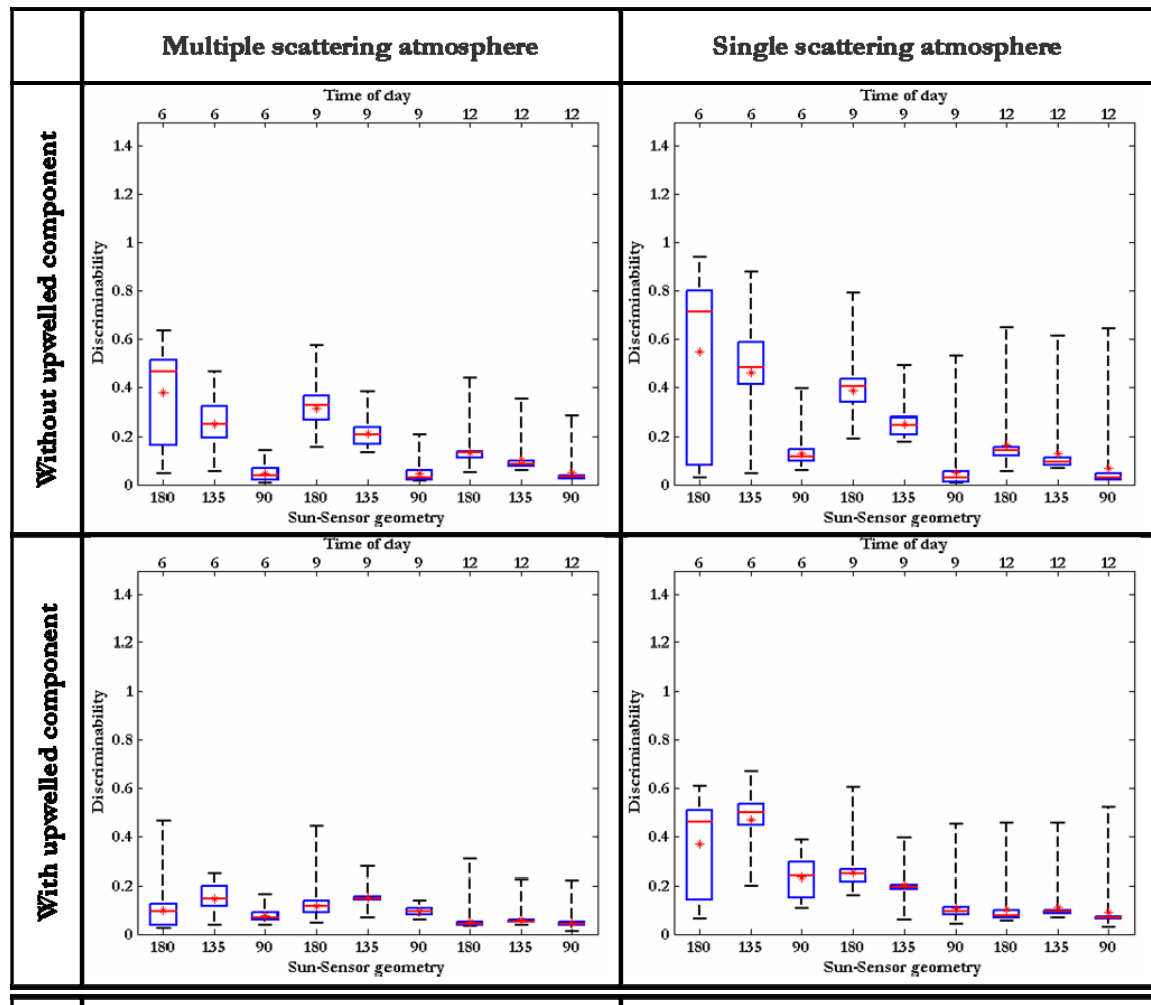
Figure 4.31: Material discriminability of matte green target on grass.

This can be confirmed from Figure 4.31 when compared with glossy black target discriminability in Figure 4.12 and glossy green target discriminability in Figure 4.27.

Figure 4.32 demonstrates that the observed material discriminability for matte green target is further reduced in shadow. Moreover, matte green target discriminability observed under different illumination conditions is comparable to matte black target discriminability shown in Figure 4.29 and Figure 4.30. This can be attributed to the fact that both the matte painted surfaces are spectrally different but have similar degree of polarization values.
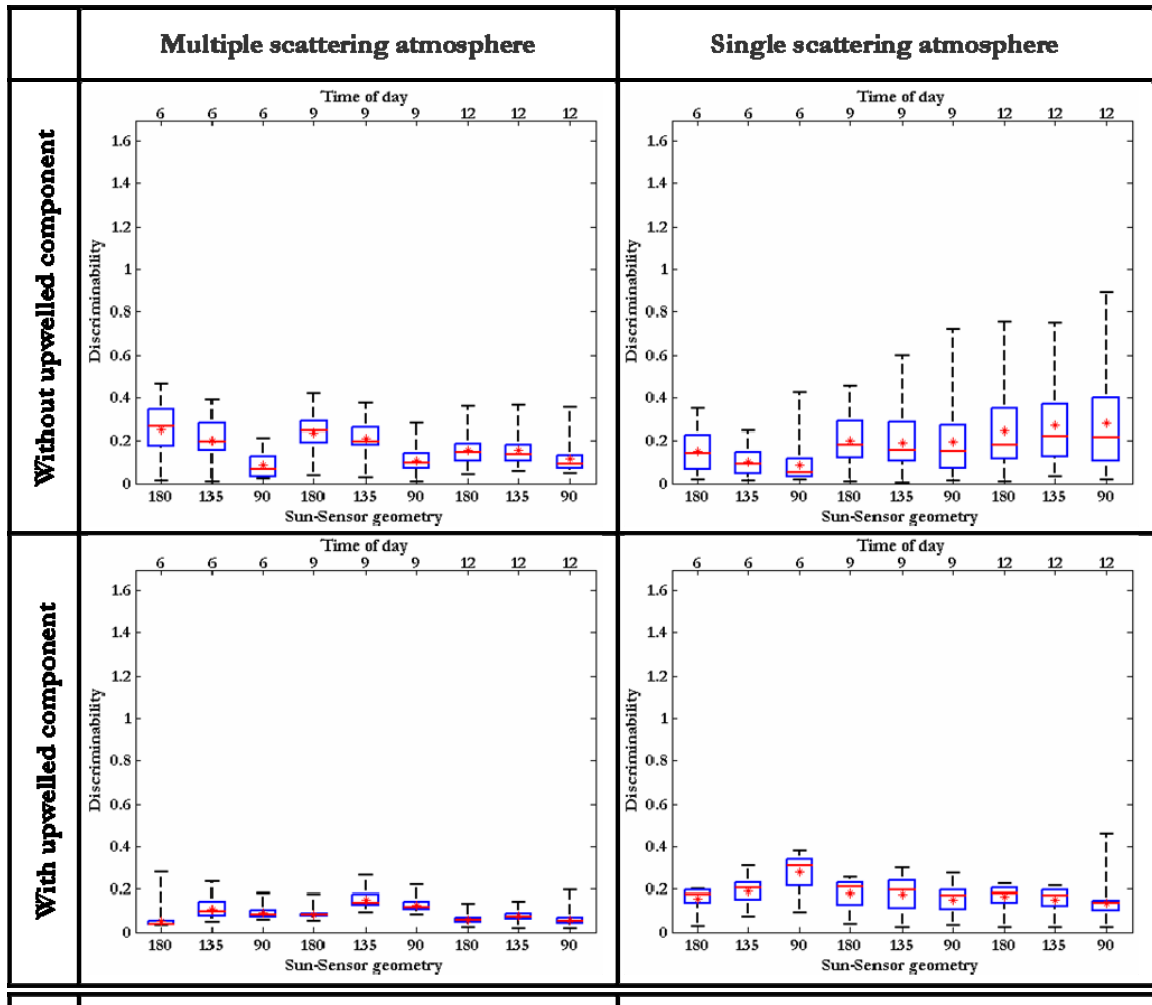
Figure 4.32: Material discriminability of shadowed matte green target on grass.

4.6 Material discriminability using complex scene analysis

Target discriminability analysis using a simple scene at varying imaging configurations facilitates understanding the influence of scene related parameters on the separability of each target material. However, the ultimate goal is to extend this polarimetric material discriminability study to a realistic remote sensing scene that contains multiple target-background materials. Results from this complex scene analysis can be integrated with the previous observations to interpret if there are any effects due to scene induced complexities on material discriminability. The main components of this study include data generation, quantification, and analysis of material discriminability in polarimetric images. This section presents the details of the complex scene analysis by addressing each of these components.

4.6.1 DIRSIG polarimetric data generation

The complex scene that was used for this study represents a remote sensing scene comprising both spatial and material type variability as shown in Figure 4.33. This cluttered scene includes different background materials such as grassland, tree canopy, soil, asphalt and man made objects like green, red, black and white glossy painted hemispherical targets. Figure 4.34 presents the sketch of some of the target models used in this analysis. In Figure 4.33, the color of the circle around the target indicates the color of the target, except blue circles correspond to glossy black targets. In addition to the target geometry the scene by itself will induce additional complexities as these targets are arranged such that they are in shadow or directly illuminated by sun or concealed in tree

canopy. The solid circle corresponds to targets under direct solar illumination while the dashed circle corresponds to targets in shadow.
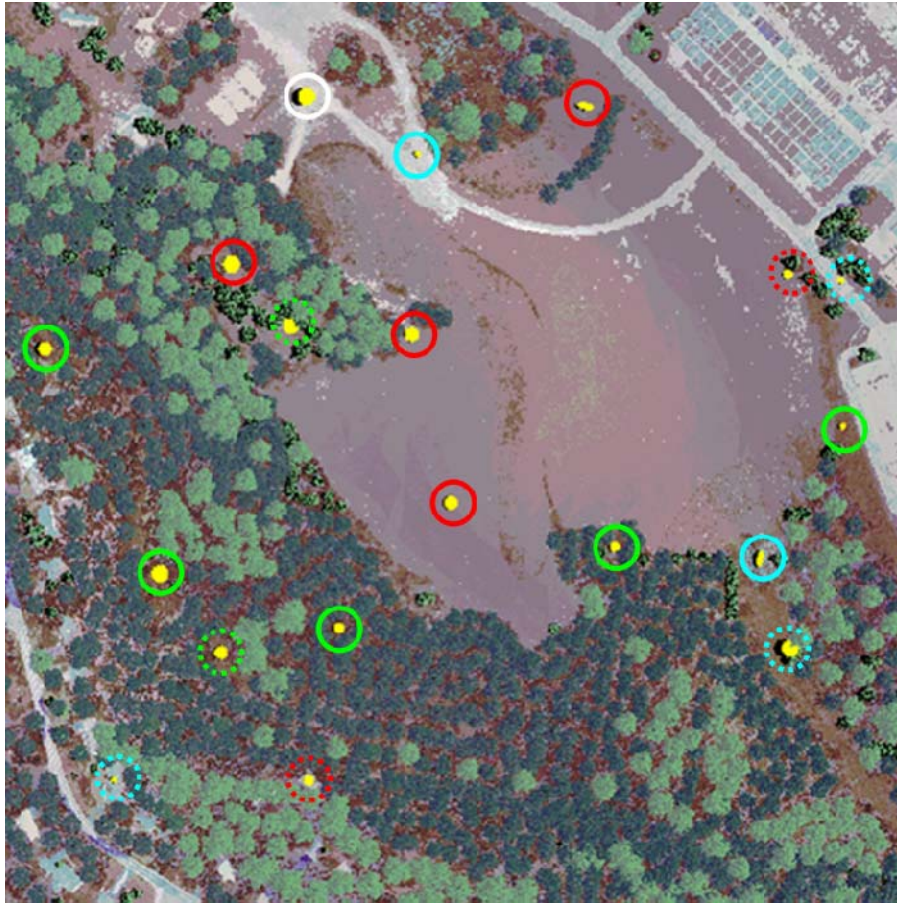
Figure 4.33: DIRSIG Megascene target layout.
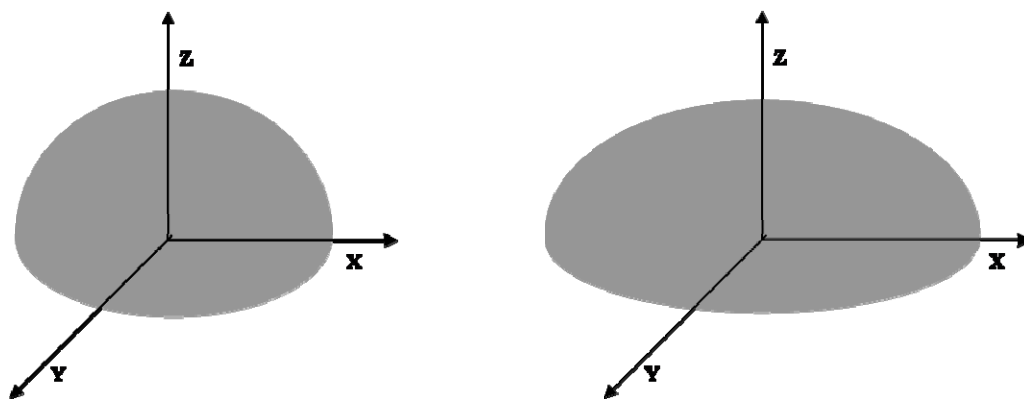
Figure 4.34: Sample target shapes used in complex scene analysis.

This analysis utilizes images acquired at three different sensor zenith angles (θ) and Figure 4.35 illustrates the platform locations for viewing the scene at nadir and off nadir when observing at a constant altitude (H). Therefore for a given detector size and observation height, the focal length (Schott 2007) for the off nadir viewing geometry is given by

$$f_\theta = \frac{f_{nadir}}{\cos(\theta)} \qquad (4.12)$$

where f_{nadir} and f_θ correspond to focal length for nadir view geometry and for a given sensor view angle respectively.
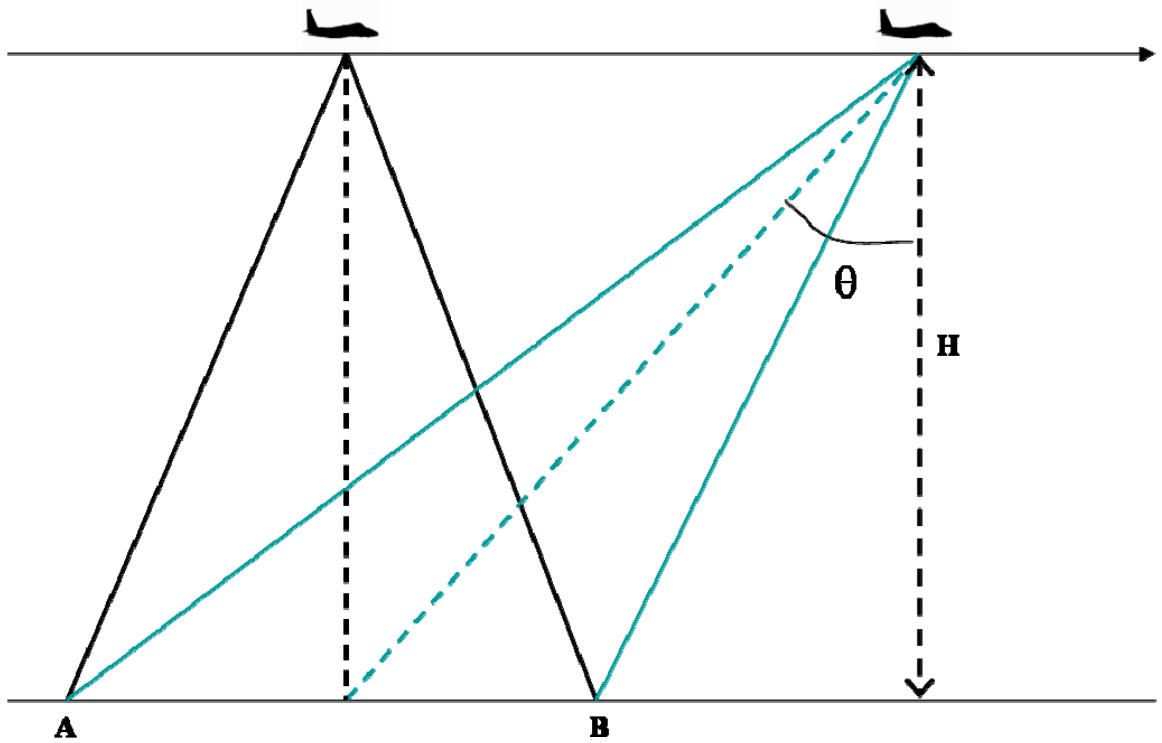
Figure 4.35: Concept of acquiring multiple view angles at constant flying altitude.

So the multi-view polarimetric imaging system can be modeled as a platform carrying three framing array systems, each pointing in the forward direction (with respect to the flying direction) in the order of increasing off nadir angle. Also the ground sample distance will be preserved by varying the focal length with the view angles using equation (4.12). However, at any given platform location the images acquired will correspond to different parts of the scene. Therefore the off nadir view angle images corresponding to the given study site (shown in Figure 4.33) were collected by calculating the location of the platform from the nadir view platform location. These images were then orthorectified by projecting them onto the ground coordinates corresponding to nadir view geometry as described in Section 4.6.2-ii.

Table 4.3: List of parameters in complex scene analysis.

PARAMETER NAME	VALUES
Observation time	6, 9, 12
Sun-Sensor geometry	180°, 135°, 90°
Atmosphere	Multiple and Single scattering
Upwelled component	Include, Remove
Target illumination	Targets in Sun and shadow
Observation altitude	5000m
Sensor zenith	20°, 40°, 60°

This analysis was performed to understand the impact of solar location on target discriminability. For each case, observations were made at different sensor azimuth locations to identify the variability in target discriminability due to changes in the view

118

geometry. The effect of different types of atmosphere was also investigated to identify the variability caused by single and multiple scattering in the atmosphere. The upwelled polarization effect on target discriminability was studied by including and removing the sensor path radiance in the simulations. In each of these simulations, the observation altitude used was 5000 m, $f_{nadir} = 200$ mm and the spatial resolution was 1 m. It can be seen in Figure 4.33 that the scene contains targets of different sizes and shapes. Such an arrangement of targets results in a variety of target surface orientations in each image simulation as there are multiple sample points on each target object. This analysis of target discriminability was performed using a well demonstrated DIRSIG simulation with an "ideal" sensor. Simulations were done without using the over-sampling option in DIRSIG. Table 4.3 provides the summary of parameters used in the complex scene analysis to identify the impact of these scene related variables on the observed target discriminability.

4.6.2 Quantification of target discriminability

4.6.2-i Visual analysis

Target discriminability analysis was performed by visual inspection of DIRSIG simulated data to identify the improvement in the image contrast using polarization information. Figure 4.36 presents the true color composite of the intensity image and Figure 4.37 presents the color composite image formed using orthorectified DOP images observed at different sensor zenith angles (20°, 40° and 60°). The orthorectification methodology will be described in Section 4.6.2-ii. In both cases the images were acquired

at 6 am in the forward scattering direction, which can be further verified from the shadows in Figure 4.36.
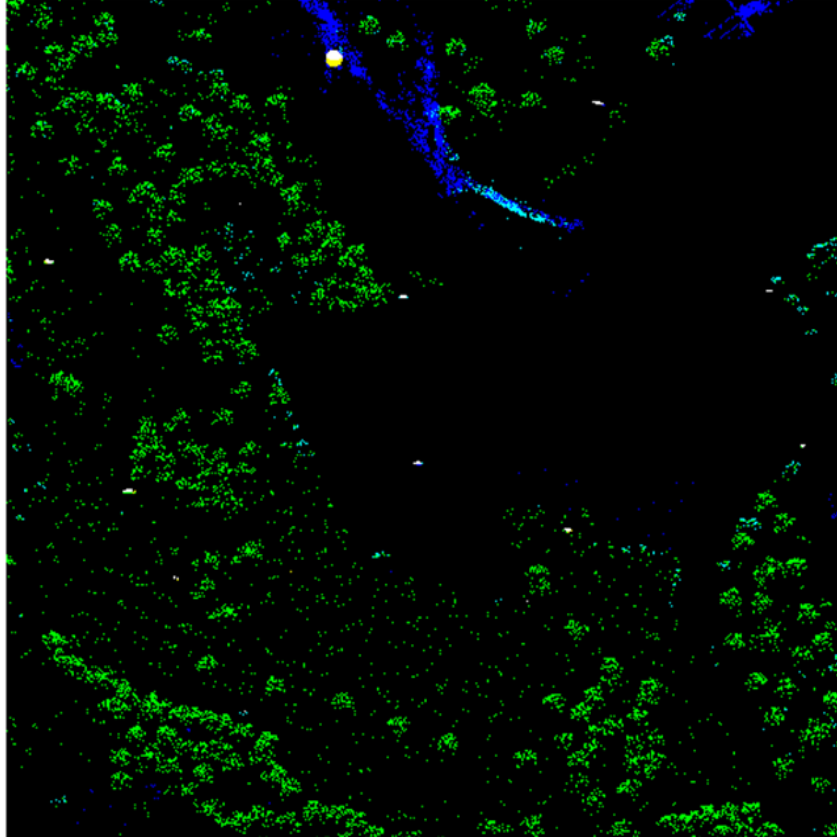
Figure 4.36: True color composite image formed using red, green and blue bands acquired at 6 am with solar zenith of 80° in the forward scattering direction.

Due to poor illumination conditions, only the white target can be visually detected in Figure 4.36 and since the sun was behind the white target part of the hemisphere is in self shadow. Also, the inverse relationship between the intensity and DOP images can be confirmed by comparing the white and black targets in Figure 4.36 and Figure 4.37. Different colors observed on the target illustrate that the observed polarization is a function of the scattering angle and therefore varies for different target surface orientation and sensor viewing angle. This demonstrates the usefulness of multi view polarimetric

images in improving the target contrast when multiple targets with different surface orientations are present in the scene. In addition, the DOP images are independent of illumination type which makes them very valuable in cases of poorly illuminated scenes where the spectral sensors show poor target discriminability.

Figure 4.37: Color composite image formed using DOP at different view angles (with 20°, 40° and 60° corresponding to red, green and blue respectively) acquired at 6 am in the forward scattering direction.

4.6.2-ii Quantitative analysis

The main objective of the material discriminability analysis in this complex remote sensing scene is achieved by identifying a suitable approach for quantification of target discriminability. Firstly, it is important to recognize that a polarimetric spectrum for a material has infinite variations due to diverse surface and observation geometries in

addition to atmospheric polarization variations. Therefore, algorithms that do not require *a priori* knowledge about the target materials are more appropriate for quantification of material discriminability in polarimetric images. So, the RX anomaly detection algorithm (Reed and Yu 1990) that detects the target by measuring its distinctness from the surrounding with no *a priori* knowledge was used.
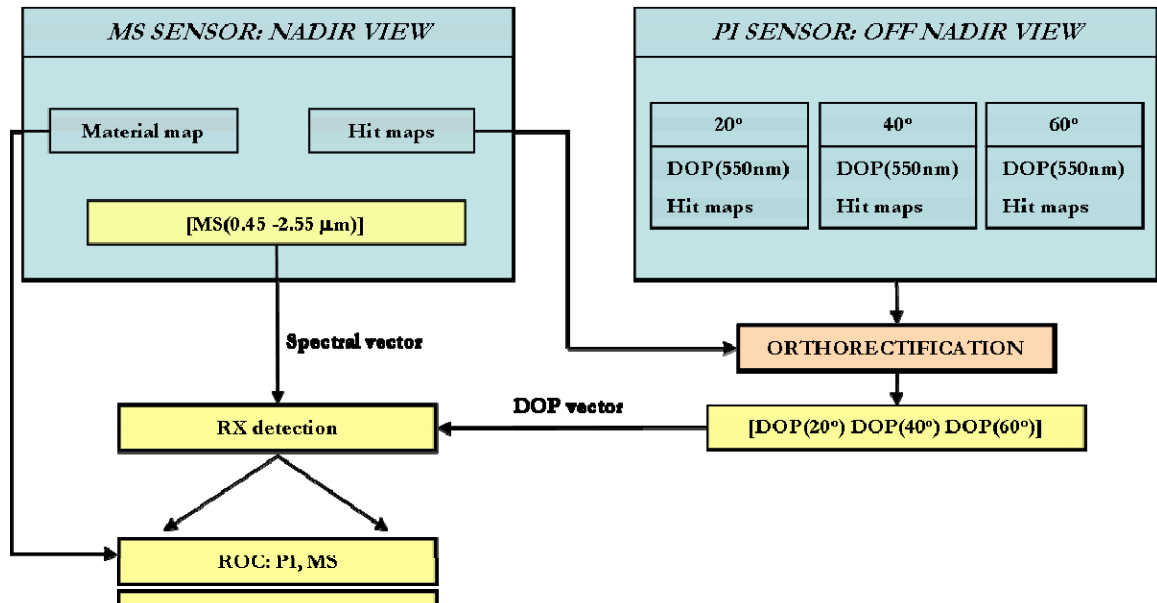
Figure 4.38: Steps in complex scene analysis.

Figure 4.38 presents the methodology used in analyzing the sensitivity of target discriminability to various scene related parameters in a polarimetric system. Target detectability of the multi view polarimetric system is compared with that of the multispectral system for each imaging configuration listed in Table 4.3. Multispectral data consists of 22 bands between $0.45 - 2.55$ μm and was acquired using a nadir viewing sensor geometry with the spatial resolution of 1 m. DOP images observed at different sensor zenith angles (20°, 40° and 60°) were orthorectified by projecting them onto the

122

ground coordinates corresponding to nadir view geometry. This can be done using the linear collinearity model (Lillesand 2008) that relates the image space to ground coordinate space for a given sensor location and focal length. However, the estimation of ground coordinates can be avoided by taking advantage of DIRSIG hit maps and directly projecting the off-nadir polarimetric images onto the nadir ground coordinates. Then the RX detection algorithm was applied on orthorectified DOP images observed at different sensor zenith angles (20°, 40° and 60°) and multispectral data. Using the material maps corresponding to nadir view geometry the detection statistics in the form of receiver operating characteristic (ROC) was calculated for these two datasets to compare their detection performance.

4.6.3 Analysis of anomaly detection performance

4.6.3-i Without upwelled component

Firstly, the effectiveness of multi-view polarimetric imaging in improving target discriminability was investigated by comparing the detection performance with that achieved using a single-view polarimetric image. The RX detection algorithm was applied on 4 different datasets namely (i) multi-view DOP (MVDOP) with S0, (ii) single-view DOP at 20° with S0, (iii) single-view DOP at 40° with S0 and (iv) single-view DOP at 60° with S0. In these datasets S0 corresponds to the panchromatic intensity image observed with nadir viewing geometry. ROC curves in Figure 4.39, Figure 4.40 and Figure 4.41 present the performance of the RX detection algorithm for different sensor azimuth angles. In all cases (a) and (d) correspond to 6 am, (b) and (e) correspond to 9 am and (c) and (f) correspond to 12 pm. Results indicate that multi-view DOP (MVDOP)

with S0 outperforms the single-view DOP with S0 in target detection performance for all sun-sensor geometries and atmospheric conditions. This confirms the usefulness of multi-view polarimetric imagery in improving target discriminability.

Next, the influence of different scene related parameters in a polarimetric system on the detection performance was quantitatively evaluated. In this analysis, the RX detection algorithm was applied on 2 different datasets namely (i) multi-view DOP (MVDOP) images, (ii) multispectral (MS) bands. This quantitative analysis will reveal scenarios where polarization imaging can be very useful in improving the target contrast. Comparison of RX detection performance of multi-view polarimetric system vs. multispectral system without upwelled component for different solar locations for sun-sensor geometry of 180°, 135° and 90° is presented in Figure 4.42, Figure 4.43 and Figure 4.44 respectively. It can be seen from Figure 4.42 that when the sensor is in the forward scattering direction, MVDOP detection performance is better than MS especially at 6 am and 9 am and the performance is comparable at 12 pm. This can be attributed to the fact that the DOP images are independent of illumination type which makes them valuable when the scene is poorly illuminated where the spectral sensors show poor target discriminability. Also Figure 4.42 (d) indicates the impact of polarized sky dome that slightly lowered the performance when compared to multiple scattering atmosphere in Figure 4.42 (a). Since multiple scattering atmosphere generates slightly more photons to illuminate the scene than the single scattering atmosphere, MS shows slightly poor performance for single scattering atmosphere especially at 6 am. Figure 4.43 is very much comparable to Figure 4.42 except at 12 pm, which indicates the influence of changing the sun-sensor geometry to 135°. MVDOP detection performance is still better

for lower solar locations. Figure 4.44 indicates the sensitivity of polarimetric imaging to sun-sensor geometry. When the sensor is located at 90° with respect to sun, MVDOP performs better than MS only at 6 am for both the atmospheric conditions. However, at 9 am and 12 pm for single scattering atmospheric condition, MVDOP detection performance is significantly reduced. In the case of single scattering atmosphere, detection performance of MVDOP is still comparable to MS at 9 am and 12 pm. Therefore by comparing Figure 4.42, Figure 4.43 and Figure 4.44 it can be concluded that the optimal sensor geometry is 180°. It can also be observed that the detection performance of MVDOP is lower than MS at lower Pfa values. This can be attributed to the fact that the MS images show higher contrast for the white target which does not have any polarization characteristic. Also multiple scattering atmosphere always enhanced target discriminability because target polarization response could be lowered if there is any mismatch between the surface orientation and direction of polarization of the skylight in the case of single scattering atmosphere.
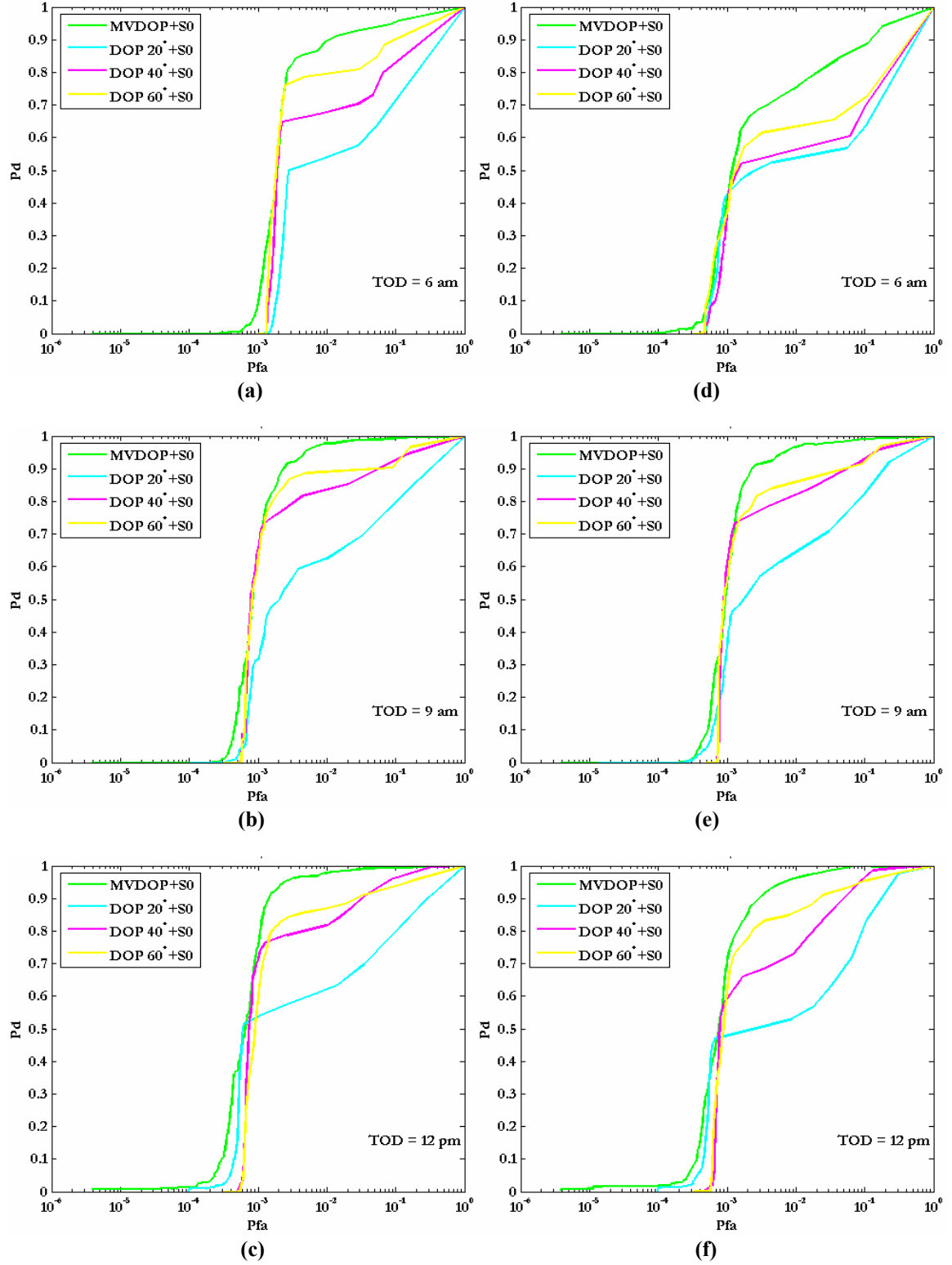
Figure 4.39: Comparison of RX detection performance of multi-view vs. single-view polarimetric imagery without upwelled atmospheric component for different solar locations with sun-sensor geometry of 180⁰ (a)-(c) multiple scattering atmosphere and (d)-(e) single scattering atmosphere.
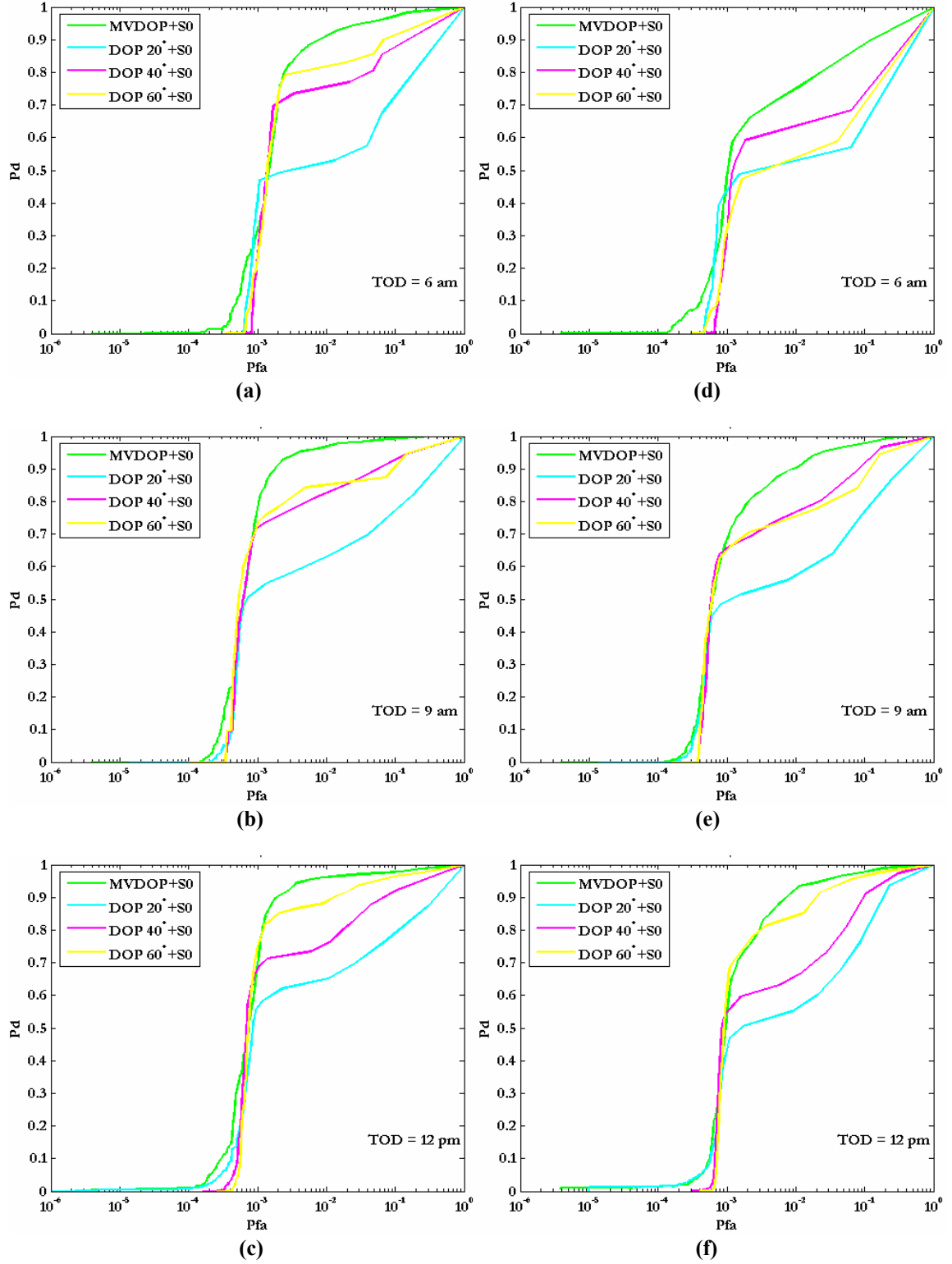
Figure 4.40: Comparison of RX detection performance of multi-view vs. single-view polarimetric imagery without upwelled atmospheric component for different solar locations with sun-sensor geometry of 135° (a)-(c) multiple scattering atmosphere and (d)-(e) single scattering atmosphere.
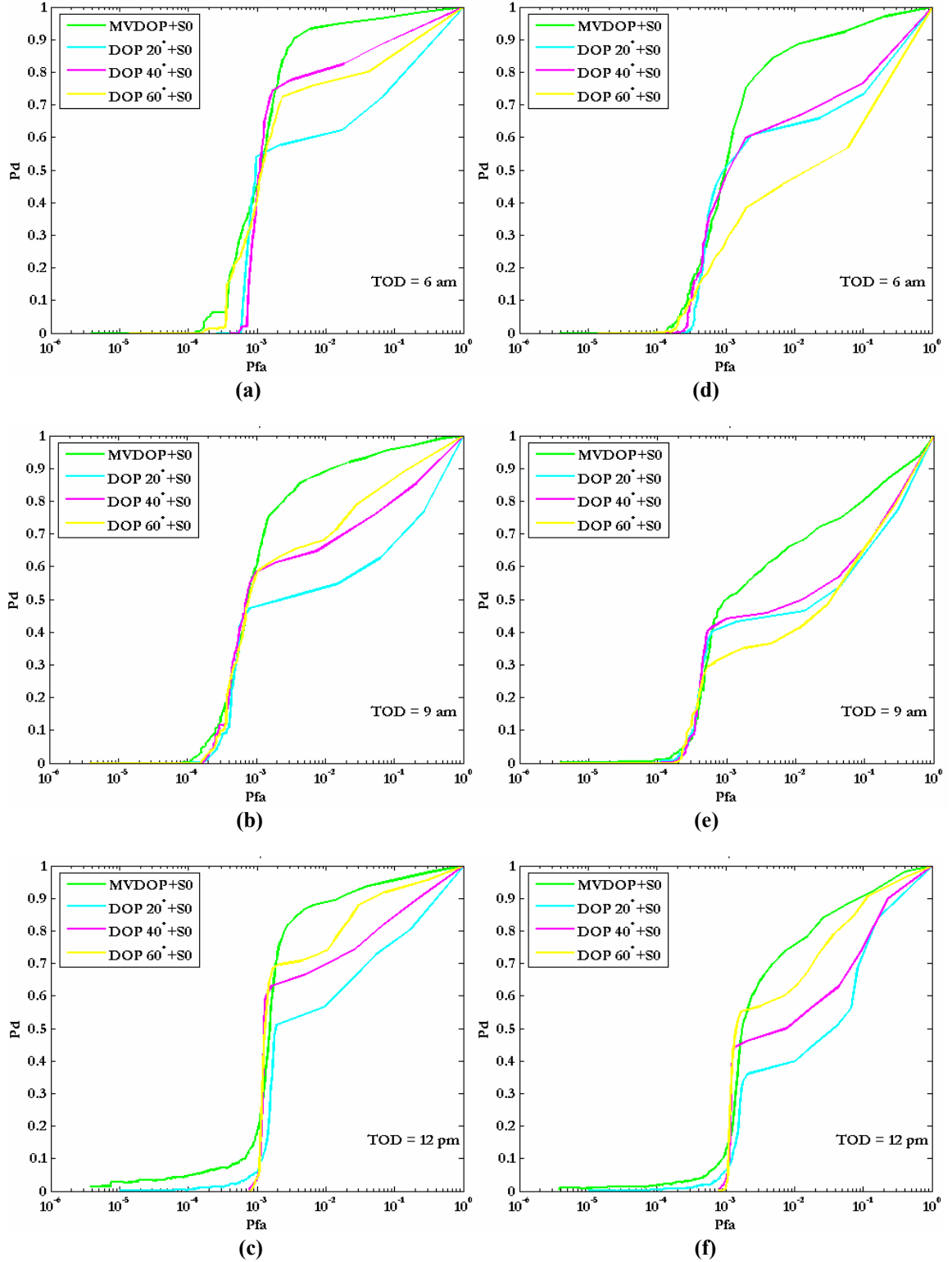
Figure 4.41: Comparison of RX detection performance of multi-view vs. single-view polarimetric imagery without upwelled atmospheric component for different solar locations with sun-sensor geometry of 90° (a)-(c) multiple scattering atmosphere and (d)-(e) single scattering atmosphere.

Figure 4.42: Comparison of RX detection performance of multi-view polarimetric system vs. multispectral system without upwelled component for different solar locations with sun-sensor geometry of 180° (a)-(c) multiple scattering atmosphere and (d)-(e) single scattering atmosphere.

Figure 4.43: Comparison of RX detection performance of multi-view polarimetric system vs. multispectral system without upwelled component for different solar locations with sun-sensor geometry of 135° (a)-(c) multiple scattering atmosphere and (d)-(e) single scattering atmosphere.

Figure 4.44: Comparison of RX detection performance of multi-view polarimetric system vs. multispectral system without upwelled component for different solar locations with sun-sensor geometry of 90° (a)-(c) multiple scattering atmosphere and (d)-(e) single scattering atmosphere.

131

4.6.3-ii With upwelled component

The intent of this analysis was to identify the influence of the upwelled polarization component on the detection performance. Comparison of RX detection performance of multi-view polarimetric system vs. multispectral system with upwelled component for different solar locations for sun-sensor geometry of 180°, 135° and 90° is presented in Figure 4.45, Figure 4.46 and Figure 4.47 respectively. Compared to Figure 4.42, Figure 4.43 and Figure 4.44, the detection performance of multi-view polarimetric system is severely affected as the upwelled component has a depolarizing effect on the target polarization. In addition, the background materials in the scene look falsely polarizing due to the polarized upwelled component in the image as described in equation (4.8) resulting in higher false alarms. This effect of upwelled component can be further verified in Figure 4.48 which presents the color composite images formed using the orthorectified multi-view DOP images acquired at 6 am in the forward scattering direction for single and multiple scattering atmospheres.

The sensitivity of upwelled component in polarimetric imaging to sun-sensor geometry can be easily identified as the detection performance degrades when the sensor is located at 90° with respect to sun and this effect is more prominent at 6 am. Also, results from the simple scene analysis in Section 4.5 indicated that the optimal time of day that maximizes target discriminability is 9 am (with the sensor in forward scattering direction) when the upwelled polarization component was included and this can be observed again in Figure 4.45. In summary, polarimetric images that include the upwelled component contain more information about the atmosphere than the target polarization information and therefore reduce the detection performance.
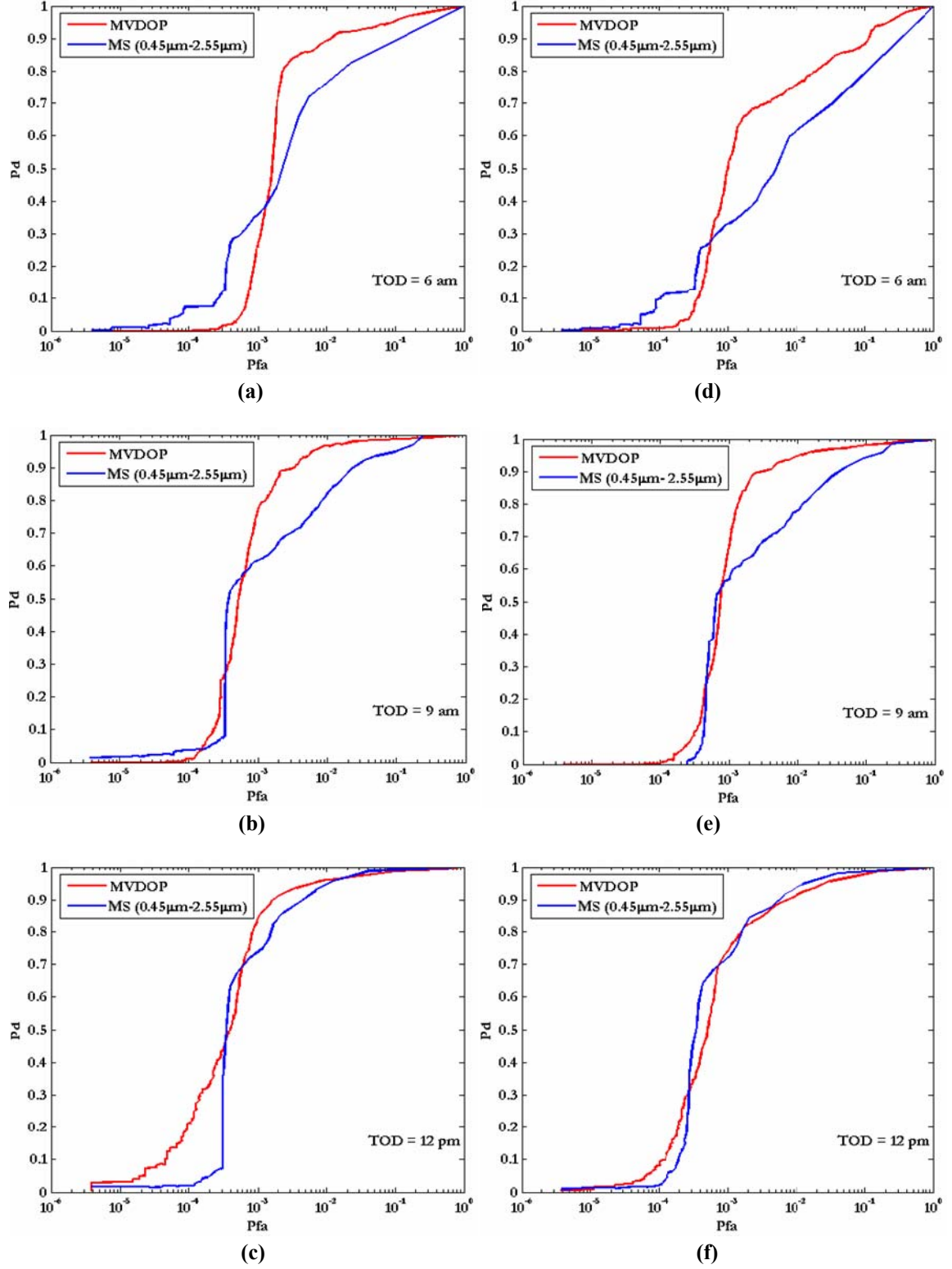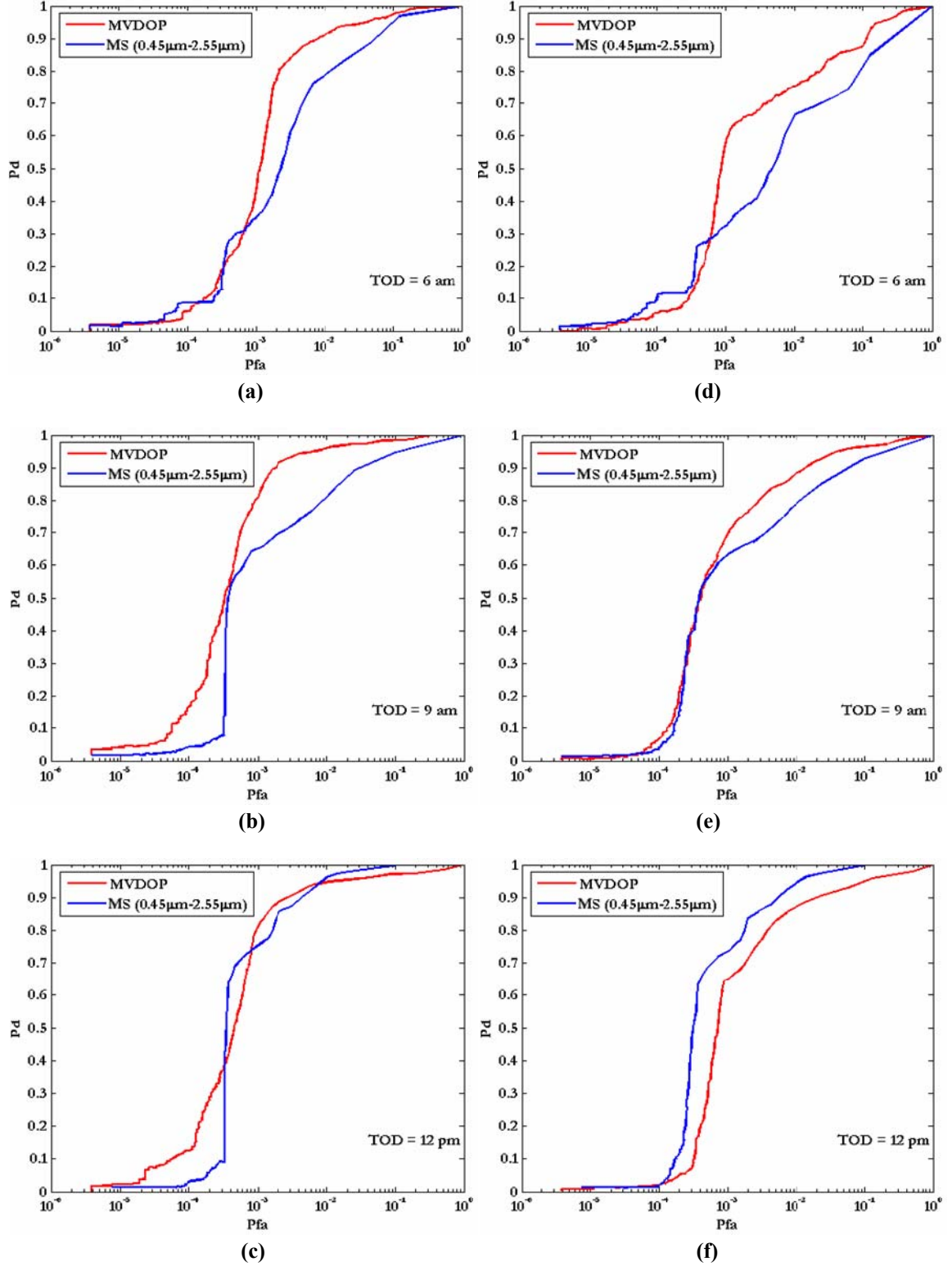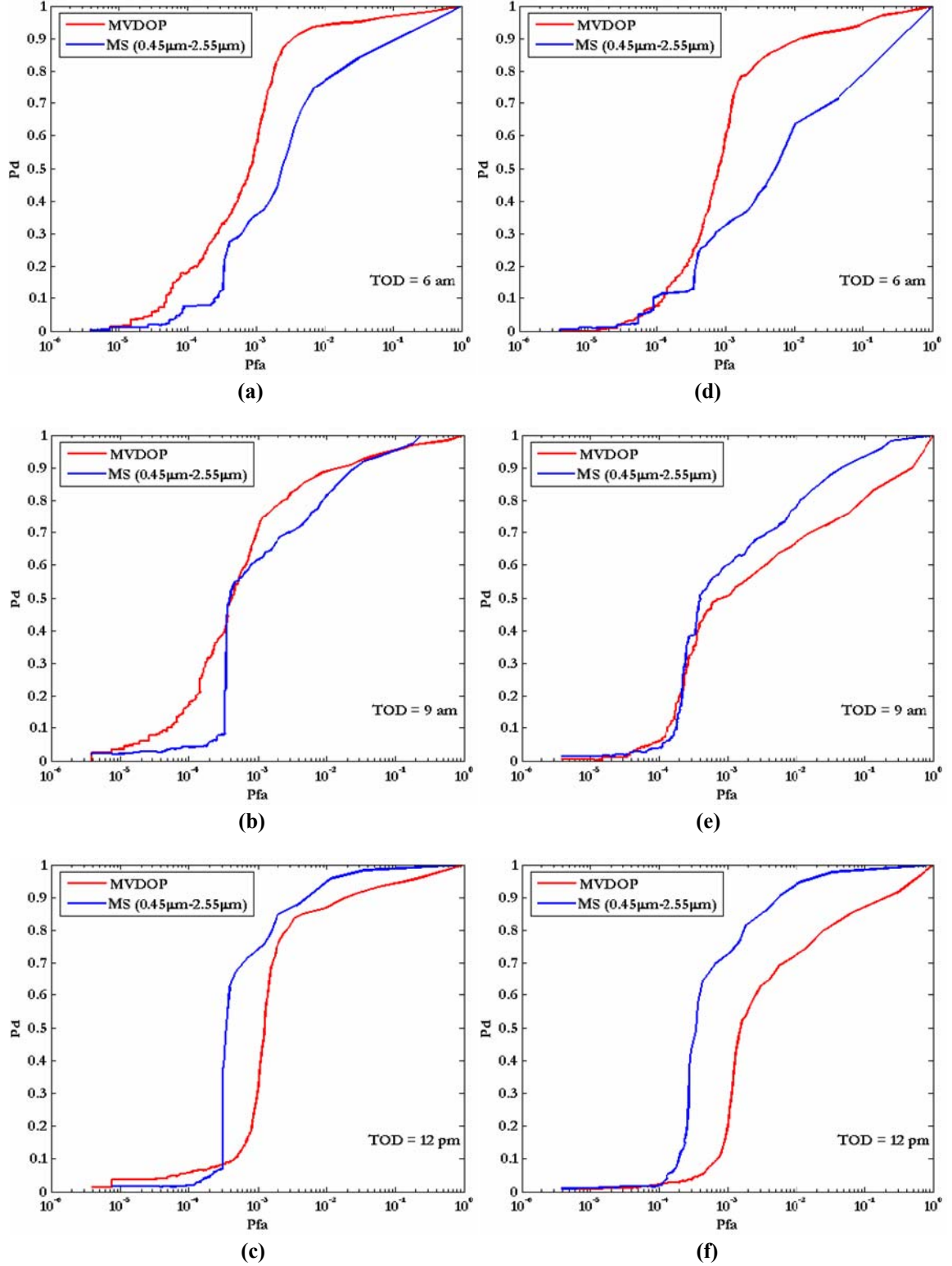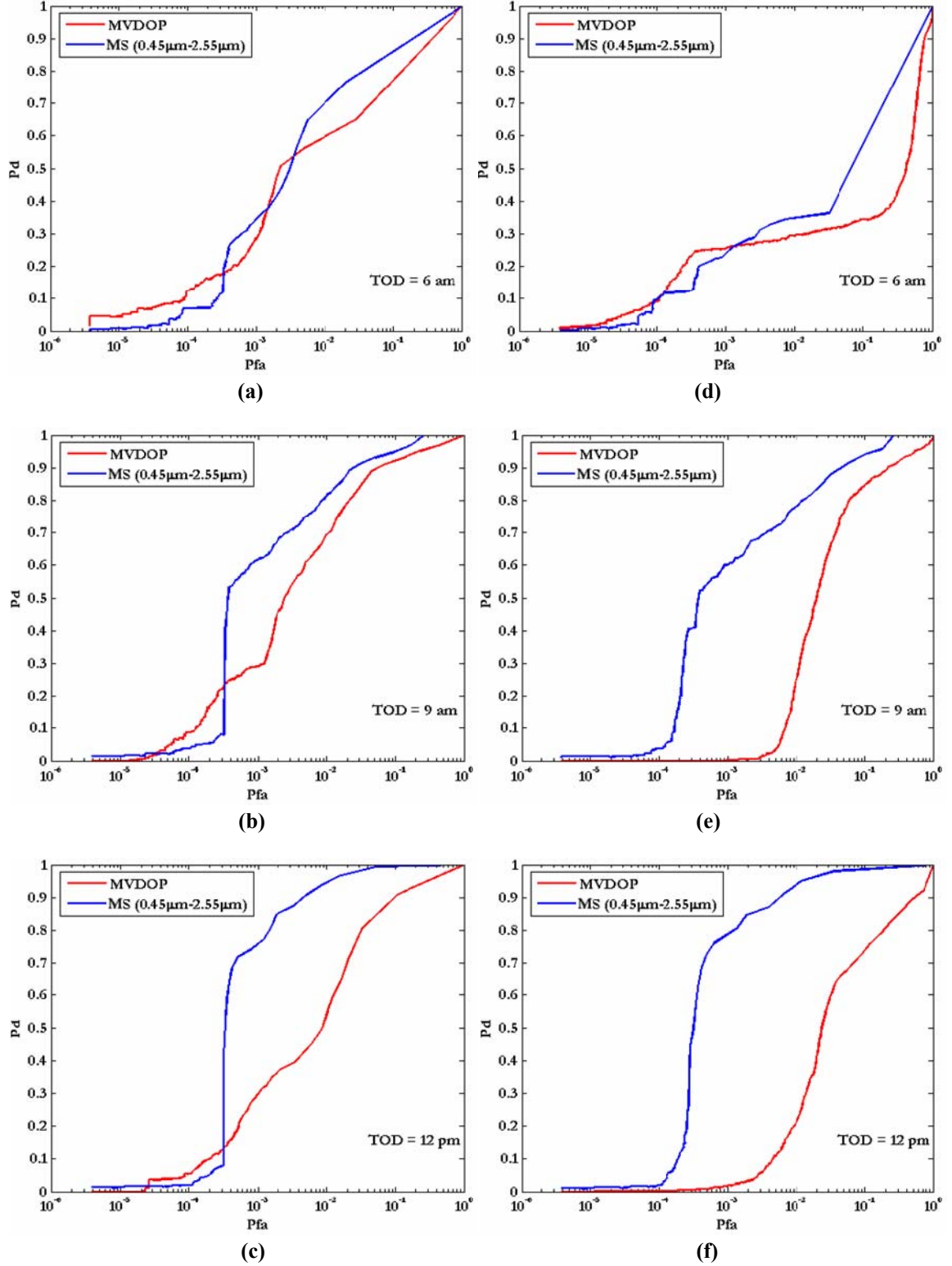
Figure 4.45: Comparison of RX detection performance of multi-view polarimetric system vs. multispectral system with upwelled component for different solar locations with sun-sensor geometry of 180° (a)-(c) multiple scattering atmosphere and (d)-(e) single scattering atmosphere.

133

Figure 4.46: Comparison of RX detection performance of multi-view polarimetric system vs. multispectral system with upwelled component for different solar locations with sun-sensor geometry of 135° (a)-(c) multiple scattering atmosphere and (d)-(e) single scattering atmosphere.

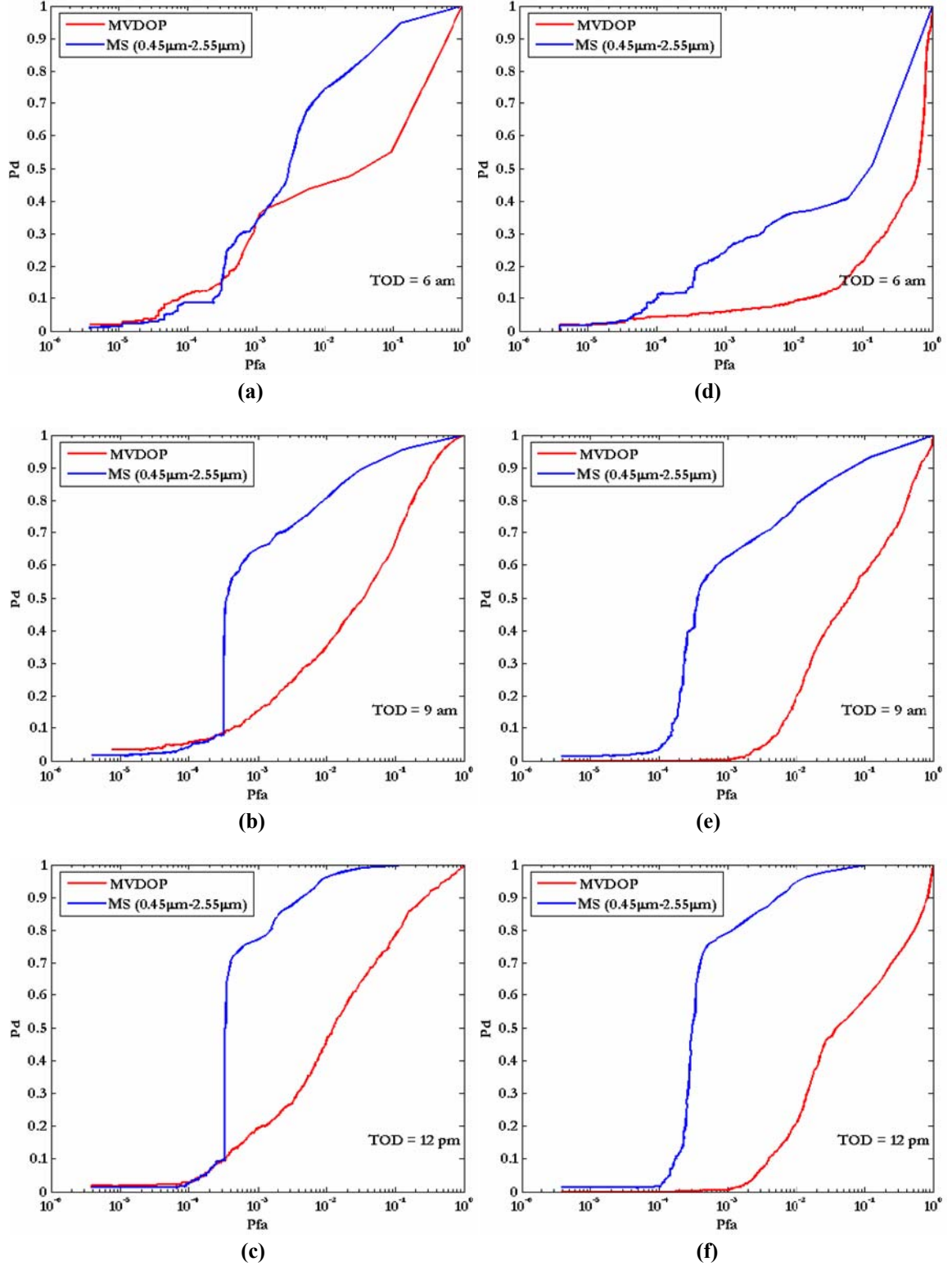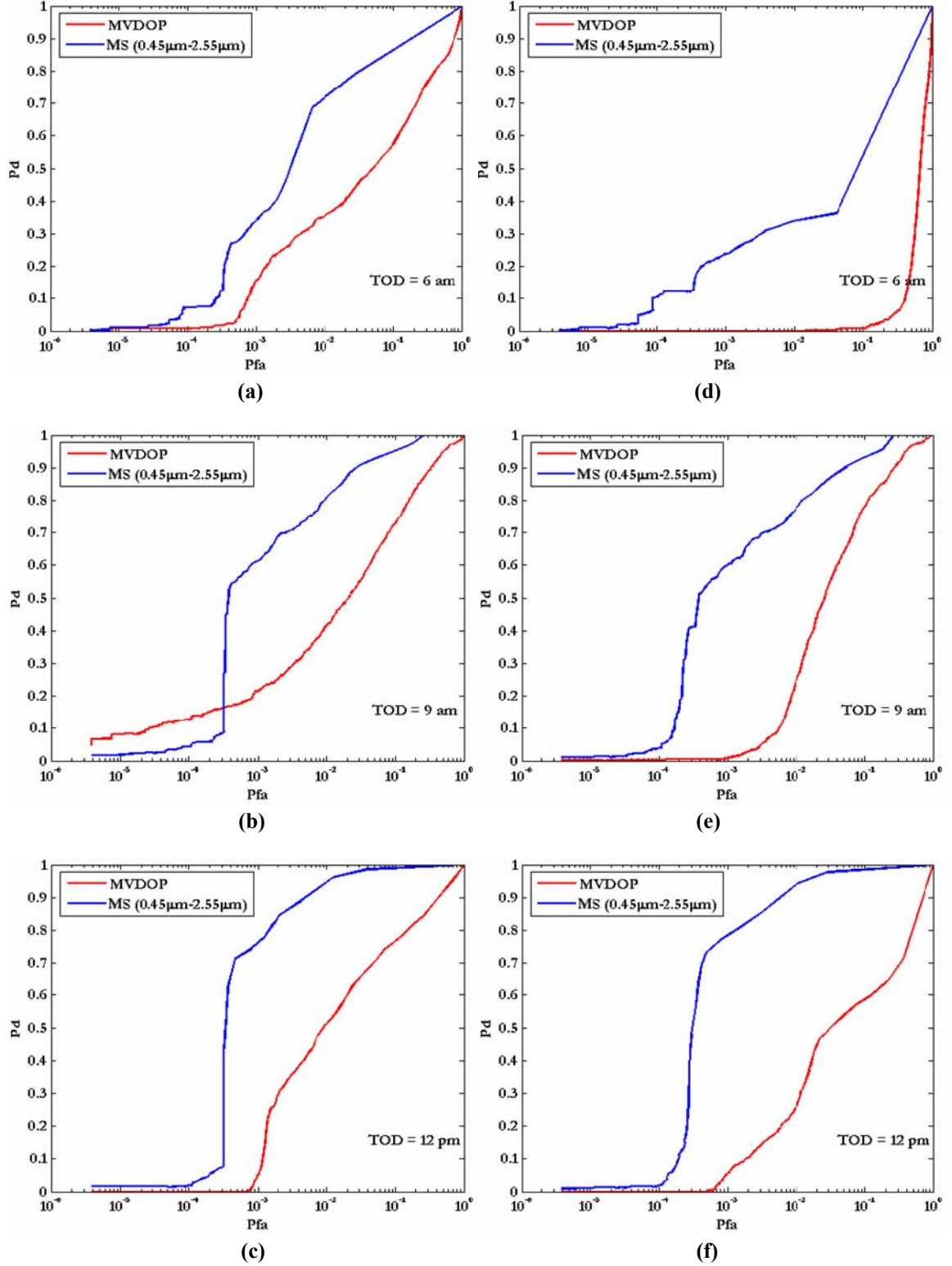**Figure 4.47: Comparison of RX detection performance of multi-view polarimetric system vs. multispectral system with upwelled component for different solar locations with sun-sensor geometry of 90° (a)-(c) multiple scattering atmosphere and (d)-(e) single scattering atmosphere.**

135
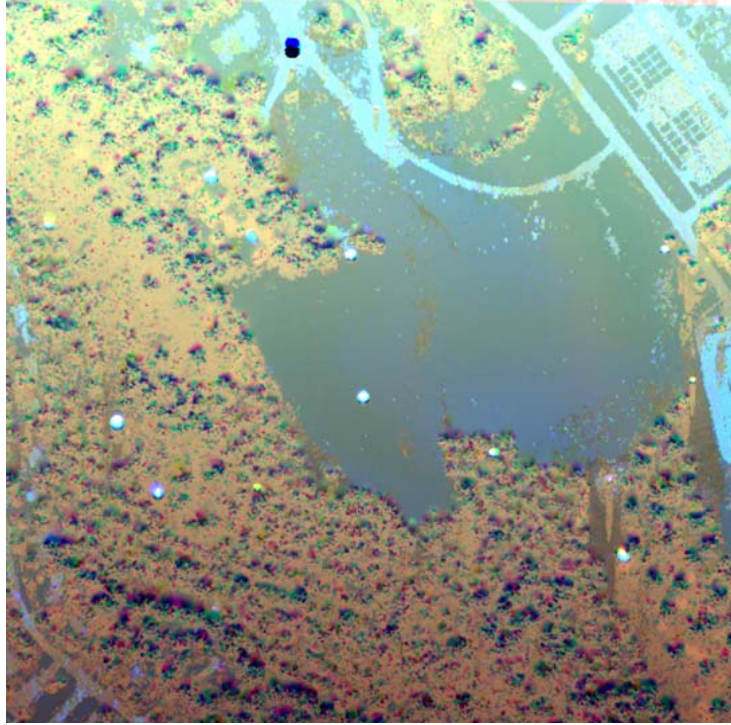
(a)
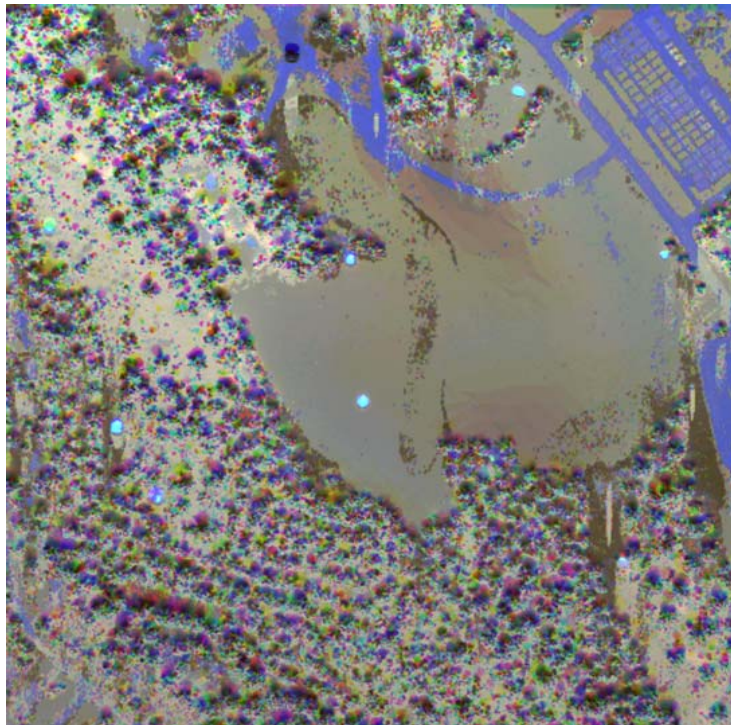
(b)

Figure 4.48: Color composite image formed using DOP at different view angles (with 20°, 40° and 60° corresponding to red, green and blue respectively) acquired at 6 am in the forward scattering direction with upwelled component for (a) multiple and (b) single scattering atmospheric condition.

4.7 Summary

This chapter explored the functional relationship between the fundamental system parameters and the polarimetric properties of a material by examining the target discriminability at different imaging configurations. This chapter also included DIRSIG data generation, quantification, and analysis of material discriminability in polarimetric images. It described a polarization physics-based approach for improving the target-background discriminability and demonstrated the usefulness of this approach in improving detection performance in the absence of *a priori* knowledge about the target geometry. This chapter also provided the results of sensitivity analysis of material discriminability in a simple scene for different target background combinations. In addition, the chapter presented the results of target detection performance of the proposed multi-view polarimetric system and multispectral system for a complex remote sensing environment to identify scenarios where polarization imaging can be useful in improving the target discriminability.

CHAPTER 5

Conclusions

5.1 Research summary

The research presented in this dissertation was conducted to advance our knowledge in polarimetric remote sensing. Through this polarization phenomenology study, we wanted to answer a broader scientific question - "*How will different scene related parameters in polarimetric remote sensing system influence material discriminability?*" Hence the main objective of this research was to understand the physics of polarimetric remote sensing and integrate this knowledge in developing techniques to effectively extract the scene information. The research findings will be of significance to the remote sensing community as it reveals scenarios where polarization information can be very useful in improving the target contrast. The two major components of this research include:

(3)   Validating the capability of DIRSIG in polarimetric image modeling and simulation.

(4)   Investigating the impact of system parameters on material discriminability in polarimetric images.

5.2 Research contributions

5.2.1 DIRSIG polarimetric system validation

The Digital Imaging and Remote Sensing Image Generation (DIRSIG) model is a high fidelity synthetic image generation tool developed at the Rochester Institute of Technology (RIT) to simulate broadband, multispectral and hyperspectral imagery. Recently, DIRSIG was extended to support rendering scenes polarimetrically in the visible through thermal infrared regions of the spectrum. The DIRSIG validation component of this research verified the correctness of implementation and integration of each link in the polarimetric imaging chain within the simulation model. A theoretical framework was developed for validating the capability of DIRSIG in predicting the polarized signatures within a natural scene. The accuracy of integration of the polarized version of MODTRAN code within the DIRSIG model was validated by performing skylight polarization analysis. The correctness of integration of skylight polarization component with the surface reflection polarization inside DIRSIG was confirmed using water surface reflected skylight analysis. The accuracy of DIRSIG in modeling the surface reflection polarization phenomenology was verified by examining the relationship between surface reflection polarization parameters and object geometry for objects with different optical properties. The accuracy of DIRSIG in calculating the polarized upwelled term and its integration with the surface reflection polarization component was verified using a traditional remote sensing calibration technique. The results provide improved confidence in the synthetic polarized images generated using the DIRSIG model.

5.2.2 Polarization phenomenology and target discriminability

In this research component, the main objective was to identify the imaging conditions under which we can maximize target discriminability using polarization information. Various factors include time of day, sun-sensor geometry, atmospheric conditions and object geometry. Moreover, in polarimetric imaging the observed polarization response is a function of the target scattering angles which depends on the relative orientation of the target surface with respect to the sensor. Hence a polarization physics-based approach, which utilizes the polarimetric information observed at multiple sensor view angles, for improved target-background discriminability was proposed and the usefulness of the approach in improving detection performance in the absence of *a priori* knowledge about the target geometry was demonstrated. Target discriminability analysis highlighted the fact that the DOP images are independent of illumination type which makes them valuable in cases of poorly illuminated scenes where the spectral sensors showed poor target discriminability. The detection performance in single scattering atmosphere was significantly decreased when the sensor was located at 90° with respect to sun. It also indicated that the polarized sky dome slightly lowered the performance compared to multiple scattering atmosphere. Furthermore, the target discriminability was decreased when the polarimetric images included the upwelled component since it contained significant information about the atmosphere relative to the target polarization information.

Since skylight polarization is sensitive to the molecular composition of the atmosphere, target discriminability will also depend on weather conditions and geographic location of the scene. For example, the imaging in clear sky conditions in

Arizona will present a single scattering atmosphere when compared to turbid sky conditions in Rochester that results in multiple scattering atmosphere. Therefore, in this research we demonstrated the impact of different atmospheric conditions on target discriminability for different sun-sensor geometry. In addition, the importance of atmospheric correction for improved detection performance using polarimetric images was demonstrated.

Sensor characteristics play a vital role in determining the usefulness of the acquired polarimetric data, as the measurement precision influences the accuracy of the extracted polarization information. As a result, these measurement inconsistencies will influence the physical and geometrical properties of the targets in the observed images. Therefore, it is essential to recognize the magnitude of variation in the observed polarimetric material discriminability due to various sensor related parameters. In this research, a comprehensive analysis of material discriminability was performed using a well demonstrated DIRSIG simulation with an "ideal" sensor. Future study will focus on identifying different sources of measurement errors such as spatial misregistration, polarization analyzer orientations, and sensor noise that will affect the target discriminability in a polarimetric system.

References

Atkinson, G.A., & Hancock, E.R. (2006). Recovery of surface orientation from diffuse polarization. *IEEE Transactions on Image Processing, 15*, 1653-1664.

Berk, A., Berstein, L.S., & Robertson, D.C. (1989). MODTRAN: a moderate resolution model for LOWTRAN 7. In, *GL-TR-89-0122, Spectral Sciences*: Burlington, MA.

Brines, M. (1978). Skylight polarization patterns as cues for honey bee orientation: physical measurements and behavioural experiments. In: Rockefeller University,1978.

Clarke, D., & Grainger, J.F. (1971). *Polarized light and optical measurement*. Oxford, New York: Pergamon Press.

Coulson, K., Jitendra, D., & Sekera, Z. (1960). Tables Related to Radiation Emerging from a Planetary Atmosphere with Rayleigh Scattering. *University of California Press.*

Coulson, K.L. (1966). Effects of reflection properties of natural surfaces in aerial reconnaissance. *Applied Optics, 5*, 905-917.

Coulson, K.L. (1988). *Polarization and intensity of light in the atmosphere*. Hampton, Va., USA: A. Deepak Pub.

Curran, P. (1981). The relationship between polarized visible light and vegetation amount. *Remote Sensing of Environment, 11*, 87-92.

Curran, P. (1982). Polarized visible light as an aid to vegetation classification. *Remote Sensing of Environment, 12*, 491-499.

Curran, P.J. (1978). A photographic method for the recording of polarised visible light for soil surface moisture indications. *Remote Sensing of Environment, 7*, 305-322.

Curran, P.J. (1979). The use of polarized panchromatic and false-color infrared film in the monitoring of soil surface moisture. *Remote Sensing of Environment, 8*, 249-266.

DIRSIG (2004). Digital Imaging and Remote Sensing Lab, The DIRSIG User's Manual, 3.5.3 edition. In: Rochester Institute of Technology.

Egan, W.G. (1970). Optical stokes parameters for farm crop identification. *Remote Sensing of Environment, 1*, 165-180.

Egan, W.G. (1985). *Photometry and polarization in remote sensing*. New York: Elsevier.

Egan, W.G. (1999). Inverse relationship between surface brightness and polarization. In, *Rough Surface Scattering and Contamination* (pp. 232-239). Denver, CO, USA: SPIE.

Egan, W.G. (2000). Detection of vehicles and personnel using polarization. In, *Polarization Analysis, Measurement, and Remote Sensing III* (pp. 233-237). San Diego, CA, USA: SPIE.

Egan, W.G. (2004). *Optical Remote Sensing Science and Technology*. NY: Marcel Dekker Inc.

Egan, W.G., & Duggin, M.J. (2000). Optical enhancement of aircraft detection using polarization. In, *Polarization Analysis, Measurement, and Remote Sensing III* (pp. 172-178). San Diego, CA, USA: SPIE.

Egan, W.G., & Duggin, M.J. (2002). Synthesis of optical polarization signatures of military aircraft. In, *Polarization Analysis and Measurement IV* (pp. 188-194). San Diego, CA, USA: SPIE.

Egan, W.G., Israel, S., Johnson, W.R., & Whitehead, V.S. (1992). High resolution space shuttle polarimetry for farm crop classification. *Applied Optics, 31*, 1542-1548.

Fetrow, M. (2003). MODTRAN4-P: Developing a polarized version of MODTRAN In: AFRL,Limited distributions.

Gál, J., Horváth, G., & Meyer-Rochow, W.B. (2001). Measurement of the reflection-polarization pattern of the flat water surface under a clear sky at sunset. *Remote Sensing of Environment, 76,* , 103–111.

Gartley, M.G. (2007). Polarimetric modeling of remotely sensed scenes in the thermal infrared. In: Rochester Institute of Technology.

Genda, H., & Okayama, H. (1978). Simulator for remote sensing and its application to soil moisture measurements. *Applied Optics, 17*, 807-813.

Goldstein, D.H. (2003). *Polarized light*. New York: Marcel Dekker.

Gonzalez, R.C., & Woods, R.E. (2002). *Digital Image Processing*: Prentice Hall.

Hecht, E. (1990). *Optics*. MA: Addison-Wesley.

Horváth, G. (1995). Reflection-polarization patterns at flat water surfaces and their relevance for insect polarization vision. *Journal of Theoretical Biology, 175*, 27–37.

Horváth, G., & Varjú, D. (2004). *Polarized light in animal vision: polarization patterns in nature*. Berlin: Springer.

Jones, D.G., Goldstein, D.H., & Spaulding, J.C. (2006). Reflective and polarimetric characteristics of urban materials. In, *Polarization Analysis, Measurement, and Remote Sensing VII* (p. 62400A). San Diego, CA, USA: SPIE.

Jong, W.d., Cremer, F., K. Schutte, & Storm, J. (2000). Usage of polarisation features of landmines for improved automatic detection. In, *Polarization Analysis, Measurement, and Remote Sensing VII* (pp. 241–252). San Diego, CA, USA: SPIE.

Können, G.P. (1985). *Polarized light in nature*: Cambridge University Press.

Lee, R.L. (1998). Digital imaging of clear-sky polarization. *Applied Optics, 37*, 1467-1476.

Lillesand, T.M., Kiefer, R.W., & Chipman, J. (2008). *Remote Sensing and Image Interpretation*: John Wiley & Sons.

Matchko, R.M., & Gerhart, G.R. (2005). Polarization azimuth angle in daylight scenes. *Optical Engineering, 44*, 028001-028009.

Maxwell, J.R., Beard, J., Weiner, S., Ladd, D.a., & Ladd, S. (1973). Bidirectional reflectance model validation and utilization. In, *Technical Report AFAL-TR-73-303*: Environmental Research Institute of Michigan (ERIM).

Meriaudeau, F., Ferraton, M., Stolz, C., Morel, O., & Bigue, L. (2008). Polarization imaging for industrial inspection. In S.N. Kurt & F. David (Eds.) (p. 681308): SPIE.

Meyers, J.P. (2002). Modeling polarimetric imaging using DIRSIG. In: Rochester Institute of Technology.

Miyazaki, D., Kagesawa, M., & Ikeuchi, K. (2004). Transparent surface modeling from a pair of polarization images. *IEEE Transactions on Pattern Analysis and Machine Intelligence, 26*, 73-82.

Morel, O., Stolz, C., Meriaudeau, F., & Gorria, P. (2006). Active lighting applied to three-dimensional reconstruction of specular metallic surfaces by polarization imaging. *Applied Optics, 45*, 4062-4068.

Priest, R.G., & Germer, T.A. (2002). Polarimetric BRDF in the Microfacet Model: Theory and Measurements. In, *Proceedings of the 2000 Meeting of the Military Sensing Symposia Specialty Group on Passive Sensors* (pp. 169–181).

Prosch, T., Hennings, D., & Raschke, E. (1983). Video polarimetry: a new imaging technique in atmospheric science. *Applied Optics, 22*, 1360.

Pust, N., & Shaw, J. (2008). Digital all-sky polarization imaging of partly cloudy skies. *Applied Optics, 47*, H190-H198.

Raven, P.N., Jordan, D.L., & Smith, C.E. (2002). Polarized directional reflectance from laurel and mullein leaves. *Optical Engineering, 41*, 1002-1012.

Reed, I.S., & Yu, X. (1990). Adaptive multiple-band CFAR detection of an optical pattern with unknown spectral distribution. *IEEE Transactions on Acoustics, Speech and Signal Processing, 38*, 1760-1770.

Rossel, S., & Wehner, R. (1982). The bee's map of e vector pattern in the sky. *Proc. National Academy of Sciences USA, 79*, 4451-4455.

Schott, J.R. (2007). *Remote Sensing: The Image Chain Approach*: Oxford University Press.

Schott, J.R. (2009). *Fundamentals of Polarimetric Remote Sensing*. Bellingham, USA: Society of Photo-Optical Instrumentation Engineers.

Schwind, R. (1991). Polarization vision in water insects and insects living on a moist substrate. *Journal of Comparative Physiology A, 169*, 531–540.

Shell, J.R. (2005). Polarimetric remote sensing in the visible to near infrared. In: Rochester Institute of Technology.

Smith, H.J.P., Dube, D.J., Gardner, M.E., Clough, S.A., Kneizys, F.X., & Rothman, L.S. (1978). FASCODE- Fast Atmospheric Signature Code (Spectral Transmittance and Radiance). In, *Air Force Geophysics Laboratory Technical Report AFGL-TR-78-0081*: Hanscom AFB, MA.

Solomon, J.E. (1981). Polarization imaging. *Applied Optics, 20*, 1537.

Stokes, G.G. (1852). On the composition and resolution of streams of polarized light from different sources. *Transactions of the Cambridge Philosophical Society, 9*, 399-416.

Tyo, J.S., Goldstein, D.L., Chenault, D.B., & Shaw, J.A. (2006). Review of passive imaging polarimetry for remote sensing applications. *Applied Optics, 45*, 5453-5469.

Umov, N. (1905). Chromatische depolarisation durch Lichtzerstreuung. *Phys. Z., 6*, 674–676.

Vanderbilt, V.C., Grant, L., Biehl, L.L., & Robinson, B.F. (1985a). Specular, diffuse, and polarized light scattered by two wheat canopies. *Applied Optics, 24*, 2408-2418.

Vanderbilt, V.C., Vanderbilt, V.C., & de Venecia, K.J. (1988). Specular, diffuse, and polarized imagery of an oat canopy. *IEEE Transactions on Geoscience and Remote Sensing, 26*, 451-462.

Vanderbilt, V.C., Vanderbilt, V.C., Grant, L., & Daughtry, C.S.T. (1985b). Polarization of light scattered by vegetation. *Proceedings of the IEEE, 73*, 1012-1024.

Walraven, R. (1981). Polarization imagery. *Optical Engineering, 20*, 14-18.

Wolff, L.B. (1990). Polarization-Based Material Classification from Specular Reflection. *IEEE Transactions on Pattern Analysis and Machine Intelligence, 12*, 1059-1071.

Wolff, L.B., & Boult, T.E. (1991). Constraining object features using a polarization reflectance model. *IEEE Transactions on Pattern Analysis and Machine Intelligence, 13*, 635-657.